AN ABSTRACT OF THE DISSERTATION OF

Trenton James Carpenter for the degree of Doctor of Philosophy in
Mechanical Engineering presented on June 4, 2015.

Title: Predicting Aerodynamic Loads on Highly Flexible Membrane Wings

Abstract approved: _____

Roberto Albertani

Through passive adaptation to incidental flow, flexible aerodynamic surfaces exploit effects of increased lift, delayed stall and disturbance rejection. Wings of birds, bats, and insects exhibit these passive effects, and at the same time through the use of structural state feedback sensed from the loads on the wing, active control is applied to achieve stable and highly dynamic maneuvers. The goal of this research is to predict aerodynamic loads on flexible wings, by sensing their structural responses to static and dynamic airflow conditions. Three approaches are presented to estimate aerodynamic loads on highly flexible membrane wings, under static and dynamic conditions, at low Reynolds number. The first applies a linear membrane formulation to correlate the wing's structural strain to lift, through wing-tip vorticity. In the second, the Poisson equation for a 2D linear-elastic membrane with out-of-plane deformation was used to calculate normal pressure distribution from virtual strain sensors using proper orthogonal decomposition basis functions and a recursive least squares minimization. Finally, potential flow theory and a first order state space representation is applied to the transient flow effects around a pitching membrane airfoil to model the time varying loads due to dynamic pitching.

Predicting Aerodynamic Loads on Highly Flexible Membrane Wings

by

Trenton James Carpenter

A DISSERTATION

submitted to

Oregon State University

in partial fulfillment of
the requirements for the
degree of

Doctor of Philosophy

Presented June 4, 2015
Commencement June 2016

<u>Doctor of Philosophy</u> dissertation of <u>Trenton James Carpenter</u> presented on <u>June 4, 2015</u>

APPROVED:

_____

Major Professor, representing Mechanical Engineering

_____

Head of the School of Mechanical, Industrial, and Manufacturing Engineering

_____

Dean of the Graduate School

I understand that my dissertation will become part of the permanent collection of Oregon State University libraries. My signature below authorizes release of my dissertation to any reader upon request.

_____

Trenton James Carpenter, Author

ACKNOWLEDGMENTS

CONTRIBUTION OF AUTHORS

TABLE OF CONTENTS

TABLE OF CONTENTS (Continued)

TABLE OF CONTENTS (Continued)

Page

LIST OF FIGURES

LIST OF FIGURES (Continued)

LIST OF FIGURES (Continued)

PREDICTING AERODYNAMIC LOADS ON HIGHLY FLEXIBLE MEMBRANE WINGS

1. INTRODUCTION

Flexible aerodynamic surfaces demonstrate improved stability and lift characteristics over their rigid counterparts in low Reynolds number flow regimes ($Re < 10^5$) [1]. Through passive adaptation to incidental flow, flexible aerodynamic surfaces exploit effects of increased lift, delayed stall and disturbance rejection [2–4]. This passive behavior, coupled with proprioceptive sensing, is utilized throughout the natural world by biological fliers such as birds, bats and insects [5, 6]. To date, fundamental research is still being conducted in this area, expanding our knowledge of the complexities of the coupled fluid-structure interactions inherent to flexible lifting surfaces.

Micro Air Vehicles (MAV), as defined by [7], are in general lacking in their ability to match the agility, control and overall aerodynamic performance of birds, bats and insects [8]. One potential leap in this technology could come from the use of structural state feedback measured from the lifting surfaces of the vehicle for use in flight control strategies. For example, it is believed that bats use thin muscles in their wings and the flex felt in their bones for sensory feedback utilized in flight [8,9]. It is also believed that birds can feel the lifting of their feathers from the surface of their wing due to air flow separation, helping them detect the onset of stall [10]. The main focus of this author's research aspires from nature through use of measurable structural state knowledge from lifting surfaces such as displacements and strain for the prediction or correlation of aerodynamic behaviors due to fluid structure interaction.

1.1.   A Brief History of MAV's and Flexible Wings

Coined by the Defense Advanced Research Projects Agency (DARPA) in 1997 [7], MAV refers to a class of unmanned aerial vehicle, defined by a wing span of 15cm or less and typical operation in flow regimes with a Reynolds number of 10^3 to 10^5. Observing the Great Flight diagram in Fig. 1.1, the full spectrum of natural and man-made flying objects can be seen. In general, MAVs occupy a region on the diagram between 7-20 m/s flight speed and 0.1-10N wing load [11]. These low operational speeds result in unfavorable aerodynamic conditions which reduce authority of flight controls and cause flight instability [1]. Wind gusts can cause a change to the vehicle's angle of attack, resulting in massive flow separation, loss of lift and reduction in lift-to-drag ratio [12]. It has been shown that flexible lifting surfaces, such as membrane wings, can significantly reduce these adverse effects compared to rigid lifting surfaces [2, 3, 13]. Numerous fixed, rotary and flapping wing designs have been proposed in the last decade aimed at producing a stable, agile MAV or furthering our understanding of their behavior [14–27]. To date, the majority of MAVs are rather conventional in design and have yet to fulfill DARPA's original vision of agility, robustness, autonomy and stealth [28]. Yet, a company from California, Aerovironment Inc., has successfully engineered a flapping artificial craft with the size and similar flight mechanics as a hummingbird. The craft can hover, fly forwards and backwards and is rather lightweight [29]. With an aircraft realized to such a degree, the technical challenge for creating effective wings for such a design has received more research attention in recent years [30].

Noteworthy research on flight utilizing flexible wings within the MAV scale dates back to the 19th and 20th century. In 1868, equipped with newly invented slow-motion film, Marey filmed tethered insects and traced their wing tip movements with a glass filament [31]. Studies continued on flying insects in the early 1900s, yet it was not until 1956 when Jensen filmed tethered Desert Locusts, that the kinematics of the wing beat

cycle were accurate enough for aerodynamic analysis [32]. Figure 1.2(a) shows some of the kinematic results found by Jensen. Observing the composite wing paths from Fig. 1.2(a), the flapping wing motion is clearly three dimensional and has a unique geometric behavior. Several other studies on the kinematics of various tethered and free-flying insects were performed in the second half of the 20th century as reviewed by Willmott [33].
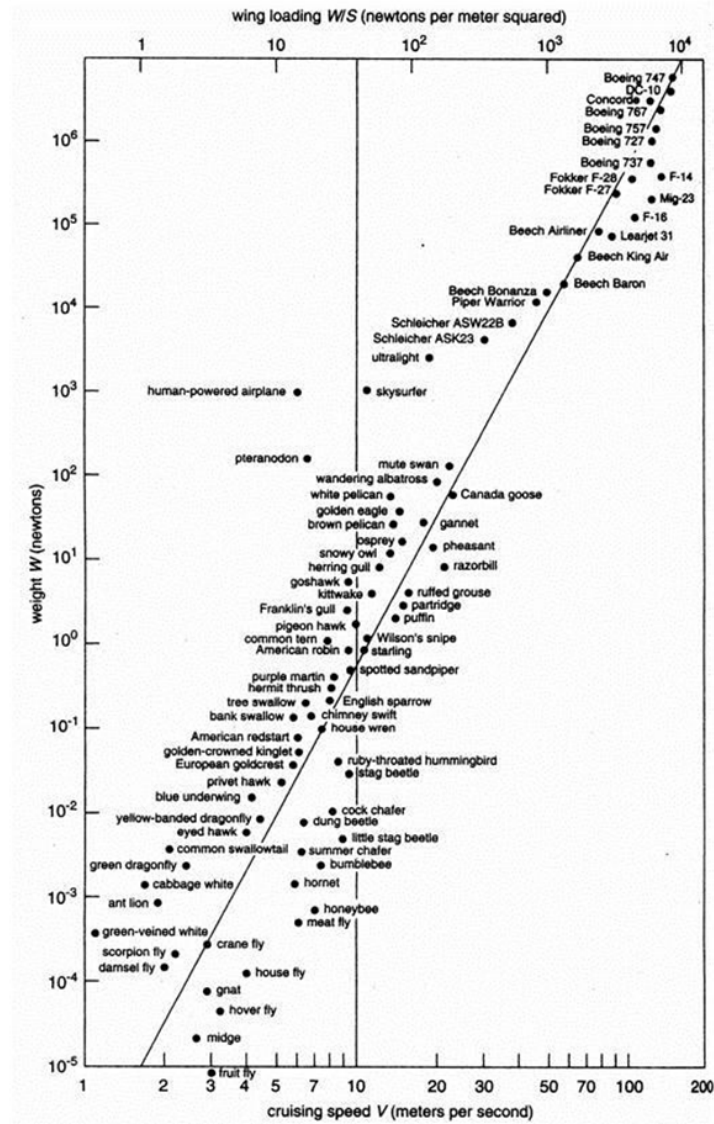
FIGURE 1.1: The Great Flight diagram [10] illustrating the relationship between flight speed, wing load and vehicle weight. Region of MAV, between 7-20 m/s and 0.1-10N.

Comprehensive studies of insect flight has been reported in Ellington's series from 1984, "The Aerodynamics of Hovering Insect Flight" [34–39]. In this work he discusses a quasi-steady lifting theory for flapping flight based on the blade element theory, insect morphological effects on power consumption, kinematic comparisons of different species of insects, and aerodynamic mechanisms as vortices which generate lift and thrust. Following this work over a decade later, with flow visualizations of a hawkmoth flight in a wind tunnel, Willmott et al. progresses understanding of the unsteady lift producing flow mechanisms present during the wing beat cycle [33, 40]. The unsteady vortices developed along the leading edge of the wing, their progression to tip vortices and their ultimate shedding, are illustrated in Fig. 1.2(b). Studies were also conducted to measure the lift and thrust produced by insects during flight. By tethering the insect directly to a strain gauge sting balance, in 1990 Wilkin was able to measure the instantaneous forces generated by a Locust while flapping [41]. Since the force measured was a total "body" force, comprised of both aerodynamic loads and inertial loads, additional steps were taken to decouple the two effects. Wilkin attempted to derive aerodynamic loads by subtracting calculated inertial forces. In his calculation, inertial forces were found by assuming a constant mass distribution over a rigid wing and by calculating the wing accelerations from kinematics derived from film video. This study was found to not produce accurate results, and was assumed to be due to the method of calculating inertial loads.

In 1993 Wilkin and Williams [42] compare the previous approach with a virtual air added-mass approach, originally purposed by Sedov in 1965 [43]. In this method, a cylindrical volume of virtual air mass, which would theoretically be moved by a wing, was added to the overall inertia of the system. The virtual added-mass approach produced better results, but was inconclusive as to the absolute accuracy of the method. In 2000, Sunada and Ellington extend the added-mass method to include effects from the vortices generated along the leading edge of the wing [44]. This method was used to estimate induced power requirements as opposed to aerodynamic forces, nevertheless this method

(a)   (b)
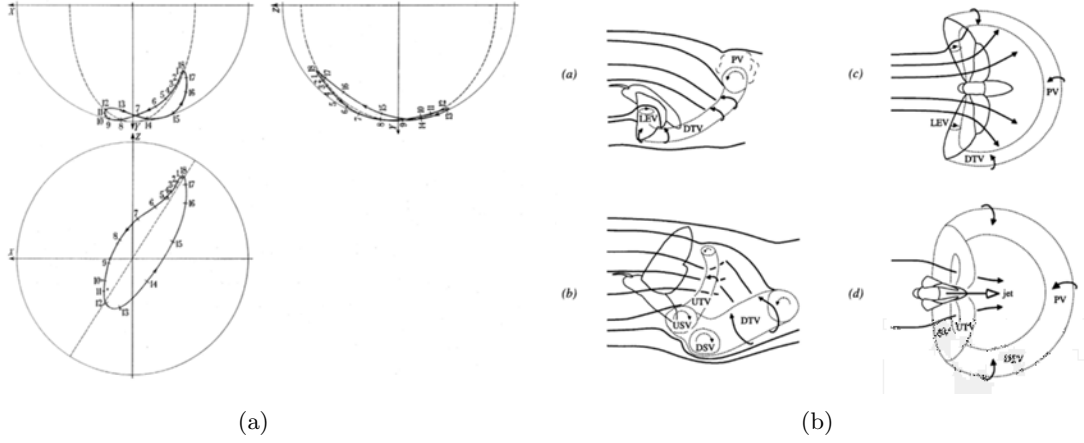
FIGURE 1.2: Movement of wing tip, Fig. 1.2(a), in relation to the Locust body during tethered flight in a wind tunnel. "A generalized model for the wake structure of a Hawk-moth Fig. 1.2(b). (a) & (b), Schematic representation of the visualized wake features during late down-stroke and late upstroke respectively. (c) & (d), Dorsal views of the same features and the accompanying air movements; leading edge vortex (LEV), down-stroke tip vortex (DTV), upstroke tip vortex (UTV), pronation vortex (PV), supination vortex (SV) [33].

was a more sophisticated approach than others of the time. Ellington's work would later be the foundation for other researchers investigating power requirements and kinematic motion for design of artificial flapping systems such as those produced by Agrawal et. al. [45, 46]. In addition to the preceding studies on insects, studies on the kinematics of dragonflies [31] and hummingbirds [47] can also be found.

Due to the advent of more powerful, readily available computers, computational fluid dynamic (CFD) simulations and structural finite element models (FEM), have become far more prevalent in this field over the last ten to fifteen years. Due to the coupled behavior of a non-rigid wing and the fluid flow around it, various numeric fluid-structure interaction simulations were developed for both fixed and flapping wings [12, 18, 23, 26, 48–52]. While coupled CFD and FEM models have proven to be accurate for solving fluid structure interaction problems for both wing-wake structures and aerodynamic loads, they are very computationally expensive and are not suitable for solving problems in real-time with today's computer technology.

In addition to simulation, researchers have also sought to characterize the unsteady

flow around flapping wings experimentally, on various forms of rigid and flexible wings [25, 26, 48, 53–56]. The typical method of flow visualization in these studies was particle image velocimetry (PIV). This technique provides two-dimensional section planes of velocity vector fields of the three-dimensional fluid flow being measured.

While both CFD and PIV methods are not used directly for real-time solutions, they are a primary means of system identification for fluid flows, [25, 26, 48, 51, 53–55, 57] . In addition to flow state identification, significant research has gone into structural state identification for wings, including, visual based measurements (digital image correlation or laser doppler vibrometery) of the wing operating in air and vacuum [20, 58]. Load identification utilizing inverse matrix methods, coupled with a finite element solver, have also seen significant research [21, 59].

In general, estimation problems start with developing a model of the system of interest. For high dimensional systems such as turbulent near-wake flows, a reduced order model will likely be required for solving real-time problems. Methods for model reduction include modal truncation, balanced realization/truncation, and proper orthogonal decomposition (POD). Prevalent estimation methods in literature relating to this field include, linear stochastic estimators (LSE) such as the Kalman filter, Monte Carlo Estimation (particle filters), deterministic approaches such as weighted least squares, and artificial neural networks estimators (ANNE). Biases vary among researchers, but in general the majority of studies utilize POD in conjunction with LSE or ANNE for flow state estimation.

Research being conducted on estimation of wake flow behavior include, water distributions systems [60, 61], traffic flow control [62, 63], process tomography (used in medical imaging) [64, 65], wind turbine blade control [66], flow control over aerodynamic optics [67], large aircraft gust tolerance [68], and aerodynamics of damaged large aircraft [69]. In addition to these real-world problems, there are also relevant studies focusing on estimation of flow around simplified geometry of bluff bodies and walls such as, separated flow over a plate with a bluff leading edge [70], wake flow for a plate with an abrupt trailing edge [71],

separated flow over a wall with a backwards facing step [72, 73], separated flow over a backwards facing ramp at varying angles [74], and flow over a circular cylinder generating a Von Karman vortex sheet [75, 76]. A study directly relating to MAV's, was the wake-flow estimation of a flexible membrane wing by Schmit and Glauser utilizing POD [77,78]. Continuing this work with the same POD approach, Glauser et. al. implemented a practical means to control turbulent flow separation over a NACA-4412 air foil utilizing a trailing edge control surface [79–81].

Proper orthogonal decomposition is utilized in this work as a form of system identification. POD, was proposed by Lumley [82,83] as a tool for identifying the most energetic coherent structures, or eddies, contained within a turbulent flow field [77]. For a more comprehensive review of work utilizing POD see [77, 84]. This approach is an optimal approach from an energy conservation standpoint, where the largest amount of energy is stored in the first modes of decomposition [85]. While POD is a powerful method of data analysis for multivariate and non-linear phenomena [86], it has its limitations, namely due to the fact that POD must be seeded by data spanning the range of conditions one wishes to model. The basic POD approach has been shown to not be well suited for flows with certain characteristics, such as different scaled flow structures, highly non-steady flow or non-periodic flow [84]. Yet, a great amount of research effort has been put into variations of this method over the last 50 years and remains an area of state-of-the-art development in flow state estimation.

The phenomena of natural vibrations occuring on highly flexible membrane wings is a common area of fluid-structure interaction research. Gursul et. al. [87–91] have been investigating the unsteady fluid structure interactions of perimeter reinforced membrane wings. Studies have been conducted under both steady and dynamic flow conditions in a low speed wind tunnel. Wings studied were typically rectangular, perimeter reinforced, covered with a thin rubber membrane with no pre-tension and had an aspect ratio of two.

1.2. Preface

Herein, three works are presented on the subject of novel predictive approaches to aerodynamic loads generated by highly flexible lifting surfaces. Strong vortical wake structures are common characteristics of natural fliers [34], and are utilized in the first work to correlate a membrane's wings induced circulation to the structural deformations experienced in the wing. Pressure distributions acting over the surface area are the primary means for a fluid to apply loads to a body. The second work utilizes a formulation of the Poisson equation to predict aerodynamic pressure distributions from virtual strain sensors over the surface of a deformed membrane wing. The final work presents an analytic potential flow approach to predicting the dynamic load and stall phenomena experienced by a pitching membrane wing. All works utilize experimental data from both wind tunnel and laboratory tests, to validate the accuracy of the predictive models presented. Individually each work represents a novel approach to predicting aerodynamic loads on a membrane wing. Together, each of these novel works increase the knowledge of aerodynamic phenomena surrounding membrane wing response and ways of predicting useful aerodynamic parameters.

Correlation of Structural Strain to Tip Vorticity and Lift for a MAV Pliant Membrane Wing

Trenton Carpenter, Cody Ray, Roberto Albertani

2. CORRELATION OF STRUCTURAL STRAIN TO TIP VORTICITY AND LIFT FOR A MAV PLIANT MEMBRANE WING

2.1. Abstract

The last decade has witnessed a surge of scientific interest in flight at the micro air vehicle (MAV) scale. To date, a MAV utilizing an adaptable, flexible smart wing design has yet to come to fruition. While highly flexible aerodynamic surfaces have repeatedly demonstrated improved performance through passive adaptation, limited structural and flow state knowledge prevents the inclusion of active control strategies which could improve performance of such designs. In this work, a flexible membrane wing constructed of latex was considered. The goal of estimating lift was approached through experimental and theoretical correlation of wing strain state due to flow-induced pressure. Using visual image correlation, elastic deformations, strains and membrane pretensions of the wing were measured in the Oregon State University wind tunnel. In addition, a six-degree-of-freedom sting balance was used to determine aerodynamic loads. A linear membrane wing formulation was utilized to correlate the wing's structural strain to lift and wing-tip vorticity. Results of the forces measured by a sting balance were then compared to those predicted by flow simulation. This work describes experimental results that illustrate the effectiveness of low fidelity models in predicting and estimating useful information for flexible wing designs.

2.2. Introduction

Scientific and engineering interest in small unmanned aerial vehicles (UAVs) and micro aerial vehicles (MAVs) has increased substantially in the last decade. Such craft are expected to benefit military, law, and search and rescue operations in a variety of ways.

However, to date, a MAV utilizing an adaptable, robust, flexible smart wing design has yet to come to fruition. While structural knowledge of such designs is well known and described in literature, the problems of control and estimation of relevant states on board such small craft (with limited computational power) is, as of yet, restricting the actual implementation of such craft in the field. Flexible aerodynamic surfaces have repeatedly demonstrated improved performance through passive adaptation to incident flow and disturbances. This passive behavior and proprioceptive sensing is utilized throughout the natural world by biological fliers such as birds, bats and insects. However, from a control design perspective, such wings present a challenge in traditional actuation approaches. Furthermore, limited structural and flow state knowledge prevent the inclusion of active control strategies which could improve performance of such designs. In response to these difficulties, a study of a flexible membrane wing constructed of latex was considered. Through experimental and theoretical correlation of wing strain state due to flow-induced pressure resultants, the goal of estimating lift was approached. Using visual image correlation (VIC), elastic deformations, strains and membrane pretensions of the wing were measured in the Oregon State University (OSU) wind tunnel along with true values for lift and drag obtained via a six degree-of-freedom sting balance. A linear partial differential equation relating pressure distribution to membrane deflection was used to relate and correlate wing structural strain to lift and wing-tip vorticity via approximating lift resultant and applying basic linear aerodynamic principles. Results from the aerodynamic forces measured by the sting balance can be compared to those predicted by flow simulation. Preliminary results indicate that such approaches to lift/circulation estimation do indeed correlate well to the true values. These approaches and results are discussed along with possible future research directions.

2.3.   Experimental Setup

During testing our objective was to determine the out-of-plane deformation of the membrane wing under steady aerodynamic loads, in different steady conditions of angle of attack (AOA) and free stream velocity. The low-speed wind tunnel at OSU was used to conduct this phase of testing which can be seen in Fig. 2.1(a). The close loop, close test section wind tunnel is capable of speeds from 1 18 meter per second (m/s) and has a 1.3 x 1.5 meter test section. The installation of the test wing can also be seen mounted to a one degree of freedom motion rig inside the test section in Fig. 2.1(a). The apparatus was used for AOA sweeps in steady state flow conditions. The angle of the apparatus was measured by an inclinometer sensor with an accuracy of 0.1 degrees. Loads were measured using a six degree-of-freedom strain gauge load cell. The load cell was capable of measuring loads up to 100 N normal force and 200 N axial force with a resolution of 0.05 N and 0.10 N respectively. The wind tunnel flow velocity was monitored by a pitot tube probe installed in the test section ahead of the model connected to a pressure transducer with a resolution of 0.05 mmH$_2$0. Air temperature was monitored by a J-type thermocouple sensor mounted inside the test section. All channels were monitored simultaneously and recorded during testing.

For this test, the three main testing variables considered were membrane pre-strain (PS), wing AOA and flow velocity (V). To design the experiment to yield results which would be readily relatable to one another, with regard to pre-strain and out-of-plane deformation, Π_2 values as defined by [10], were considered. The values for Π_2 are defined as follows,

$$\Pi_2 = \frac{\epsilon_{ps} \cdot t}{q \cdot c} \tag{2.1}$$
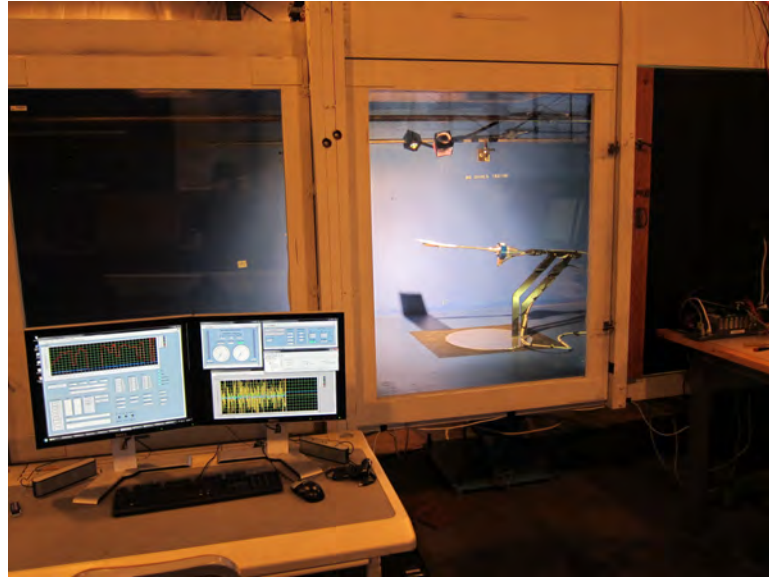
(a)
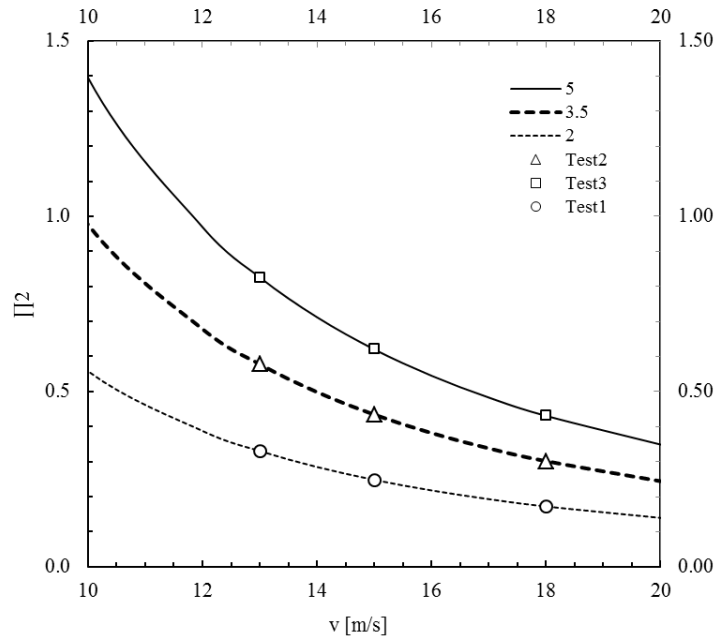
(b)

FIGURE 2.1: Exterior view of the test section of the low speed closed loop, closed test section wind tunnel at OSU (a); Values of Π_2 from eqn. 2.1, velocity and PS chosen for wind tunnel testing (b).

where ϵ_{ps} is the membrane pre-strain, t is the membrane thickness, q the dynamic pressure applied to the membrane, and c the wing chord length. Using a velocity range known to be relevant to MAV's with a Reynolds number (Re) between 60,000 and 90,000, values of pre-strain were chosen such that the maximum value of Π_2 for a given membrane would span the minimum range of the next membrane PS. The values of Π_2 chosen for the test can be seen in Fig. 2.1(b) for three different pre-strains of 5, 3.5 and 2 percent strain.

Values for AOA were chosen such that the wing would not experience flow separation, i.e. remain in the linear region of lift, thus resulting in predicable behavior easily characterized by linear aerodynamic theory. From preliminary testing results, a linear lift behavior was observed between AOA's of 0-10 degrees for membranes between 2% and 5% pre-strain. Due to interest in tip vorticity, it was also desired to have sufficiently high AOA such that strong predictable vortices would be generated. From these requirements an AOA range of 3-9 degrees was chosen. Three values for each of the three variables were chosen. This yielded a factorial design space of 3^3 or 27 tests. The resulting test matrix can be seen in Table 2.1.

TABLE 2.1: Wind Tunnel Test Matrix

Test 1			Test 2			Test 3		
PS [%]	AoA	V [m/s]	PS [%]	AoA	V [m/s]	PS [%]	AoA	V [m/s]
2	3	12	3.5	3	12	5	3	12
		15			15			15
		18			18			18
	6	12		6	12		6	12
		15			15			15
		18			18			18
	9	12		9	12		9	12
		15			15			15
		18			18			18

For the final phase of testing a rectangular planform wing with an aspect ratio of ~ 4 was chosen. A rectangular domain lends itself to linear theory structurally and is well-characterized aerodynamically. Aerodynamically, it is well-known that rectangular

wings generate strong wing-tip vortices, relative to other planforms. The tip vortices contain a significant amount of the wake flow energy and are highly indicative of the induced drag for a rectangular shape compared to other planforms. This allows closer comparison and correlation of strain to such aerodynamic effects, although any planform would exhibit the same correlation behavior due to the relationship of aerodynamic effects and structural deformation in flexible wings. An aspect ratio between 4-6 was chosen to be large enough to apply traditional aerodynamic analysis, such as lifting line theory, to the model in order to immediately compare measured and estimated quantities including lift and circulation. Structurally, a rectangular membrane under sufficient pretension exhibits behavior captured by the Poisson equation on a rectangular domain. This simplifies computation greatly and allows for a convenient rectangular domain to be defined and used directly with VIC data. The rectangular steel frame geometry used for this study can be seen in Fig. 2.3..
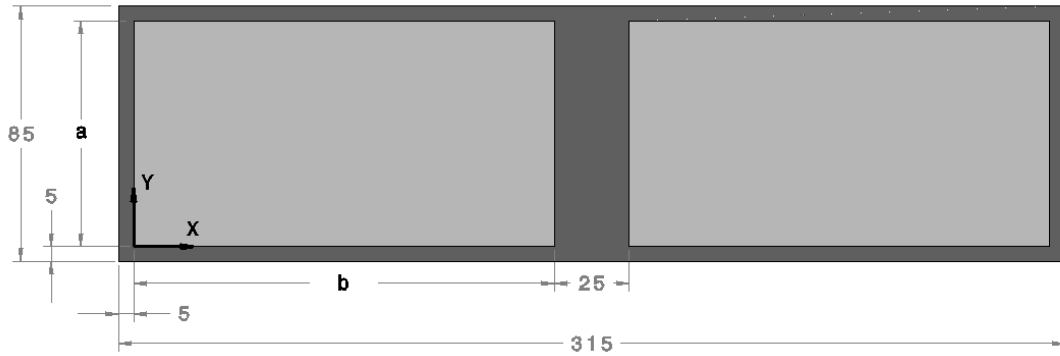
FIGURE 2.2: Schematic showing the wing frame (dark gray), the frame's dimensions and domain of the individual membrane areas (light gray); all values in millimeters.

Full-field measurements of strain and deflection of the membrane wing were performed using a visual image correlation (VIC) technique originally developed by researchers at the University of South Carolina [92, 93]. Images are captured with two high-speed AOS S-PRI cameras, capable of 1,000 frames per second and capable saving 1,000 frames at a resolution of 1280x1024 in an in-camera flash-memory buffer. The

cameras were positioned outside and above the wind tunnel and viewed through a clear window. The VIC reference image to measure displacement was of the wing at the specified AOA, with zero wind velocity. Because this condition was used to take the reference images, the pretension would not appear directly in the VIC results. The sequence of events for a given test was first to take a picture of the model at the set angle, with wind off. Next was to set the airspeed to the desired dynamic pressure, and when stable conditions were reached, take the pictures of the deformed wing as well as dynamic loads. Then the wind was stopped, and the model was moved to the next AOA. At the same time, the system was recording the aerodynamic loads, wind velocity and model AOA. This sequence was repeated for three wings with different membrane pretensions for the selected nominal AOA of 3, 6 and 9 degrees at the selected nominal wind velocities of 12, 15, and 18 m/s. The aerodynamic loads of a nominally rigid wing, built from a plate of thin sheet aluminum and attached to the same frame were also measured.

2.4. Force Estimation from Vorticity

In this approach, wind tunnel test data, numerical fluid models, and analytical structural models were used in order to estimate lift. Using VIC strain data from testing, the out-of-plane deformation of the membrane was reconstructed to fit a quadratic basis function using pseudo strain gauge sensors. Using the surface reconstruction information, a 3D solid model of the deformed membrane wing was generated and a computational fluid dynamics (CFD) analysis was performed to calculate wake behavior. Using the wake information generated from this analysis, specifically wing tip vorticity, aerodynamic lift was estimated.

2.4.1 Surface Reconstruction

In this work, it is assumed that the Poisson equation could be used to describe the membrane wing used in experiment, and proceed to use a least squares approach to estimate membrane deformation from pseudo strain sensors strategically placed throughout the membrane domain. To create the strain sensor, VIC stain data was collected over the full planform of the wing during wind tunnel testing. The full field strain domain was then partitioned into smaller individual areas, or "patches," representing the strains present on a sensor in that given location and over that given area; an example can be seen later in the text in Fig. 2.9. Using this technique, any combination of sensor quantity, size and location could be used.

Assuming the wake flow from the wing can be captured by a low order dimensional model, which has shown to be a reasonable assumption [2, 77, 94]; the pressure distribution applied to the membrane is assumed to be constant, resulting in a deformation which can be represented by a quadratic function. Using this assumption, the out-of-plan deformation of the membrane over the domain, $0 \leq x \leq a$ and $0 \leq y \leq b$, where a and b represent the dimension of the membrane boundary in the x and y direction respectively, as illustrated in Fig. 2.3.. Thus, the out-of plane deformation for the membrane, w, was modeled as,

$$w(x,y) = \frac{\alpha x(x-a)y(y-b)}{w(a/2, b/2)} \tag{2.2}$$

where α is a constant which represents the max amplitude of the membrane out-of-plane deformation. Independently differentiating equation 2.2 with respect to x and y, yields,

$$\frac{\partial w}{\partial x} = \frac{\alpha}{w(a/2, b/2)}(2x-a)y(y-b)$$
$$\frac{\partial w}{\partial y} = \frac{\alpha}{w(a/2, b/2)}x(x-a)(2y-b). \tag{2.3}$$

For a membrane subject to an evenly distributed load with small deformations, it is assumed that in-plane deformations are negligible and thus, strains are purely a result of out-of-plane deformation. Using this assumption, directional strains can be approximated as,

$$\epsilon_x = \frac{1}{2}\left(\frac{\partial w}{\partial x}\right)^2, \quad \epsilon_y = \frac{1}{2}\left(\frac{\partial w}{\partial y}\right)^2. \tag{2.4}$$

Using equation 2.2 through equation 2.4, an analytic formulation of strain over the wing domain $0 \le x \le a$ and $0 \le y \le b$, can be defined as,

$$C(x,y) = \frac{\epsilon_x + \epsilon_y}{2} = \frac{\alpha^2}{w(a/2,b/2)}\left[((2x-a)y(y-b))^2 + (x(x-a)(2y-b))^2\right]. \tag{2.5}$$

Assuming a strain sensor is used on the membrane surface which provides a non-directional strain output and has an area of s_i, VIC strain data over that area can be used to represent the sensor output as,

$$\epsilon_i = \frac{\epsilon_{x_i} + \epsilon_{y_i}}{2}, \tag{2.6}$$

where,

$$\begin{aligned}
\epsilon_{x_i} &= \frac{1}{s_i}\int_{s_i}\epsilon_x(x,y)ds, \\
\epsilon_{y_i} &= \frac{1}{s_i}\int_{s_i}\epsilon_y(x,y)ds,
\end{aligned} \tag{2.7}$$

where $\epsilon_x(x,y)$ and $\epsilon_y(x,y)$ represent values of VIC strain measurements. Given n number of strain sensors, the measured strain for each sensor on the wing can be defined as,

$$\mathbf{S} = \begin{bmatrix} \epsilon_1 \\ \epsilon_2 \\ \vdots \\ \epsilon_n \end{bmatrix}. \tag{2.8}$$

Using equation refeqn:5, corresponding analytic values to those in equation 2.8 can be defined. The analytic strain at each sensor position can be defined as,

$$\mathbf{C} = \alpha^2 \begin{bmatrix} C_1' & C_2' & \cdots & C_n' \end{bmatrix} \tag{2.9}$$

where $C_i' = C_{ii}/\alpha^2$. By observing from equation 2.2 that α is a constant throughout the domain, α can be factored out of each term of equation 2.9. Finally, by equating equation 2.8 and 2.9, a formulation is derived which can be used to solve for α,

$$\mathbf{S} = \alpha^2 \mathbf{C} \tag{2.10}$$

$$\alpha = \sqrt{\left(\mathbf{C}^T\mathbf{C}\right)^{-1}\mathbf{C}^T\mathbf{S}}. \tag{2.11}$$

Solving for α in this manner yields a least squared approximation of the constant α. Given the inherent variability in the output of the strain sensors, the variability in membrane structural properties, and irregularities in the fluid flow, this formulation generates a quadratic surface which best describes the actual out of plane deformation of the membrane. Using this surface reconstruction, a numeric fluid simulation can be performed to determine fluid behavior in the wake of the wing.

2.4.2 Numerical Fluid Model

A three dimensional, steady state, computational model was used to compute the fluid behavior induced by the deformed membrane wing. For typical MAV's, Re based

on wing chord length are commonly in the range of 10^4 to 10^5. With the given test wing described above, placed in a flow with a Re of 10^5 in air at 25 degrees Celsius and atmospheric pressure, yields a Mach number of 0.052, allowing an incompressible fluid assumption to be reasonably applied to the simulation. A symmetrical boundary condition was applied at the centerline of the wing model in order to reduce computation time. The half span simulation volume was sized to be five times larger than the chord in the flow direction, two chord lengths above and below the wing and one to the side of the wing. The volume was discretized into approximately 1.2 million hexahedral volume cells with a cell width of 0.1mm in the near wake region, with cells growing to 10mm near the simulation boundaries. The simulation volume is shown in Fig. 2.3. The Reynolds Averaged Navier Stokes equations were solved for an incompressible flow in conjunction with the Spalart-Allmaras turbulence model. As shown by [7, 8] the Spalart-Allmaras turbulence model proves to perform well in near wake regions such as wing tip vortex flows while remaining relatively computationally inexpensive.

(a)   (b)
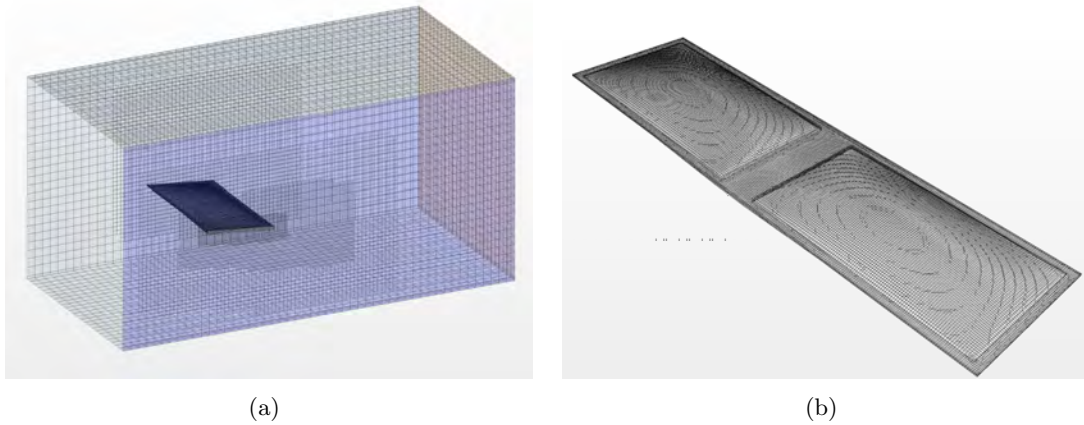
FIGURE 2.3: Half span CFD simulation domain (a) and meshed membrane wing (b) shown in full span.

The simulation used a computer-aided-design (CAD) model of the deformed membrane and the frame to which the membrane was attached. The surface of the membrane was modeled to match the quadratic form from equation 2.2. For a particular dynamic

pressure and AOA, the surface deformation constant from equation 2.11 was calculated and a model was generated accordingly. A side-by-side comparison of the actual deformed membrane during wind tunnel testing and the corresponding CAD model derived from the sensor surface reconstruction method discussed above, can be seen in Fig. 2.4.

(a)   (b)
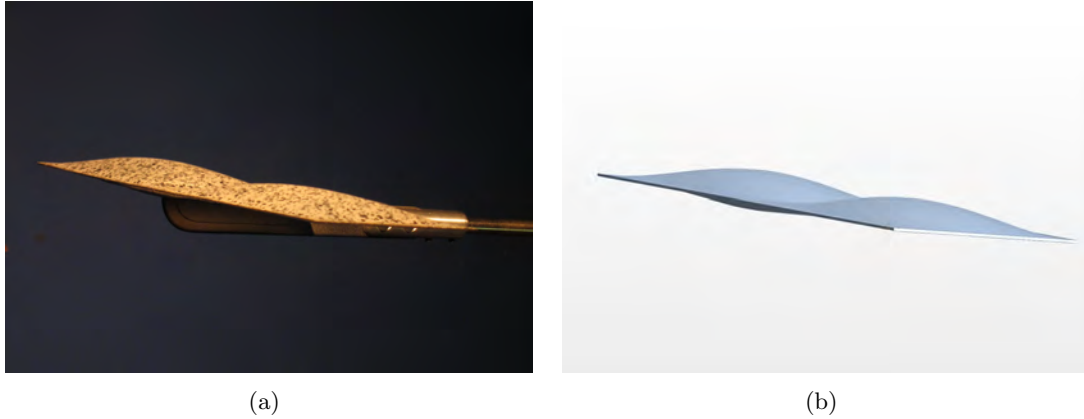
FIGURE 2.4: Speckled latex membrane wing during wind tunnel testing (a) and CAD model generated from the strain sensor surface reconstruction (b).

2.4.3   Lift from Circulation

For the purpose of this analysis, a simplified version of lifting line theory was utilized. The horseshoe vortex is a simplification of Prandtl's continuous lifting line theory. In this model, all vorticity is assumed to be present in a vortex of constant circulation bound to the wing. The bound vortex is connected at the wing-tips to two trailing vortices which extend, in theory, back to the starting vortex itself, thus forming a loop. This results in a shape reminiscent of a horseshoe in the local region of the wing. An illustration of this behavior can be seen in Fig. 2.5.
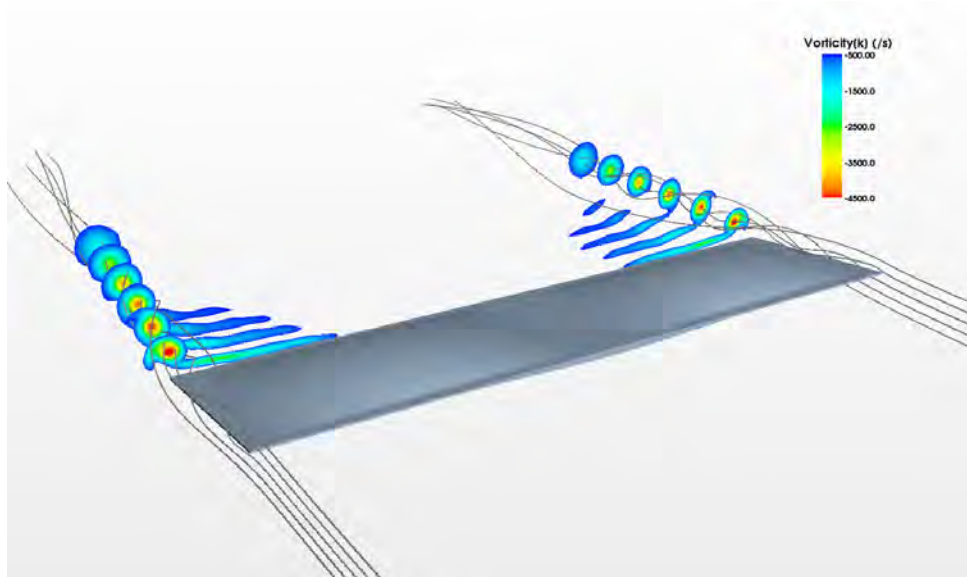
FIGURE 2.5: Vorticity contours of a 2% pre-strained membrane wing at AOA of 6 degrees and 18 m/s.

The Kutta-Joukowski theorem for steady flight states that lift is proportional to circulation as follows,

$$\frac{\partial L}{\partial x} = \rho U \Gamma \tag{2.12}$$

where $\partial L/\partial x$ is the lift per unit span (if x is in the span-wise direction and y the chord-wise), ρ is the fluid density, U is the free stream velocity, and is circulation per unit span. Circulation can be related to vorticity by Stokes' theorem,

$$\Gamma = -\oint_c V \cdot ds = -\iint_s (\nabla \times V) \cdot dS \tag{2.13}$$

where V is the flow velocity vector field, S is an area containing the vortex and c is the boundary (and a closed curve) of S. Using flow information from CFD simulations taken downstream of a wing, a velocity flow field can be extracted and equations 2.12 and 2.13 can be applied in order to derive an estimation of lift generated by the wing. Fig. 2.6 shows a vorticity contour and velocity vector field of the wake flow 15 mm behind a

rectangular membrane wing at 2 percent pre-strain, six degrees AOA and a flow regime corresponding to a Re of 90000. Also in this figure, the area of integration over the tip vortex can be seen, which was used to calculate the value of circulation per unit span from equation 2.13.
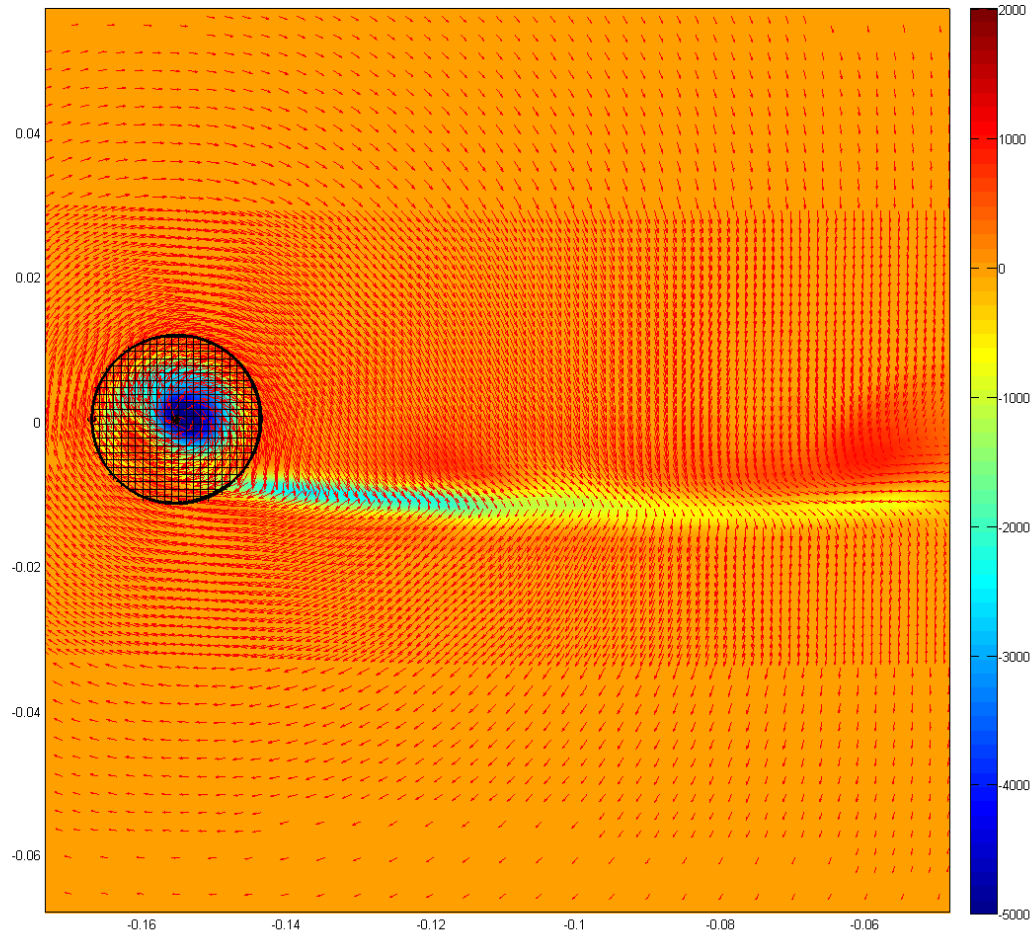
FIGURE 2.6: Contour map showing vorticity 15 mm behind wing; velocity vector field normal to free stream shown in red vectors; and circulation integration domain of wing tip vortex shown in black.

2.5. Force Estimation From Poisson Model

The linear Poisson equation, a partial differential equation, can be used to model a membrane under sufficient pretension undergoing small deformations. This section will briefly outline how the estimation of membrane deformation from strain outlined above can be used to obtain a rough estimate of the pressure distribution present on the membrane-wing; a quantity indicative of lift and strength of wing-tip vortex circulation.

The two dimensional Poisson equation is obtained through linearization of nonlinear membrane dynamical equations and/or minimization of energy of an axially deforming planar structure undergoing small transverse displacements. Such assumptions allow rotation angles of the structure and internal tension resultants to be represented as spatial derivatives and scalar constants, respectively. Thus, such a linear model is actually a model capturing the membrane's resistance to changes in its internal state of stress. Such approximations have been used to model membranes with success and become increasingly accurate as pretension increases and maximum deformation decreases. The Poisson equation can be written for a rectangular domain as,

$$T_x \frac{\partial^2 w}{\partial x^2} + T_y \frac{\partial^2 w}{\partial y^2} = F(x, y) \tag{2.14}$$

where T_x and T_y are the pretension resultants in the x and y directions, respectively, and $F(x, y)$ is the resultant pressure distribution on the membrane. Associated with this equation are boundary conditions for all edges of the domain, describing fixed edges, i.e. zero displacement.

If one makes an assumption regarding the functional form of the deformation of the membrane, i.e. quadratic in nature, the approach simplifies greatly. Supposing the membrane deformation can be represented by a single quadratic surface interpolating the boundaries of the membrane (thus satisfying the boundary conditions of Poisson's equation explicitly). Such a surface can be written as that used in equation 2.2. Once is determined

from equation 2.11, an estimate of the pressure distribution can be immediately found by substituting the equation for $w(x, y)$ back into Poisson's equation using the estimated value of α. Taking second derivatives of $w(x, y)$ and substituting into equation 2.14 yields an estimate of F from the strain values observed on the membrane.

Classical aerodynamic theory states that the derivative of lift with respect to span is proportional to circulation, as described in equation 2.12. Thus, one approach to estimate circulation is to utilize the estimated force from Poisson's equation and integrate this result analytically with respect to chord. This would yield an expression that describes the lift per unit span. If one were to integrate again with respect to span, the total lift resultant would be obtained. Therefore, by the fundamental theorem of calculus, one can integrate the estimated pressure distribution with respect to x, in order to yield an expression also describing the lift per unit span. Equating this to circulation using the classical expression for circulation as given in equation 2.12, one may divide by $\rho \cdot U$ to obtain an estimate for circulation. This provides a first-order model-based approach to estimating circulation directly from strain.

2.6.   Results and Discussion

2.6.1   Aerodynamic Loads

In order to verify lift predictions from sensed strain and CFD analysis, aerodynamic loads were measured for each wing configuration. The model was swept through AOA from 0 to 20 degrees at an air speed of 18 m/s corresponding to a chord line Re of 90000. Four wing configurations were tested; one with a 0.75 mm thick aluminum plate attached to the wing frame, and three with 0.13 mm thick latex membrane stretched over the frame, each with a different level of pre-strain. Membranes with an average percent pre-strain over the domain of the membrane of 2.13 ± 0.24, 3.36 ± 0.25 and 5.07 ± 0.41 were tested. Values of coefficient of lift versus AOA can be seen in Fig. 2.7 for each lifting surface.

Classical aerodynamic behavior is seen in that, the membrane wings continue to increase in lift at higher angles of attack (i.e., above 8-10 degrees) where the rigid plate experiences flow separation on the suction surface and fails to produce greater amounts of lift. It can also be seen that with increased membrane pretension, the lift values begin to approach that of the rigid wing.
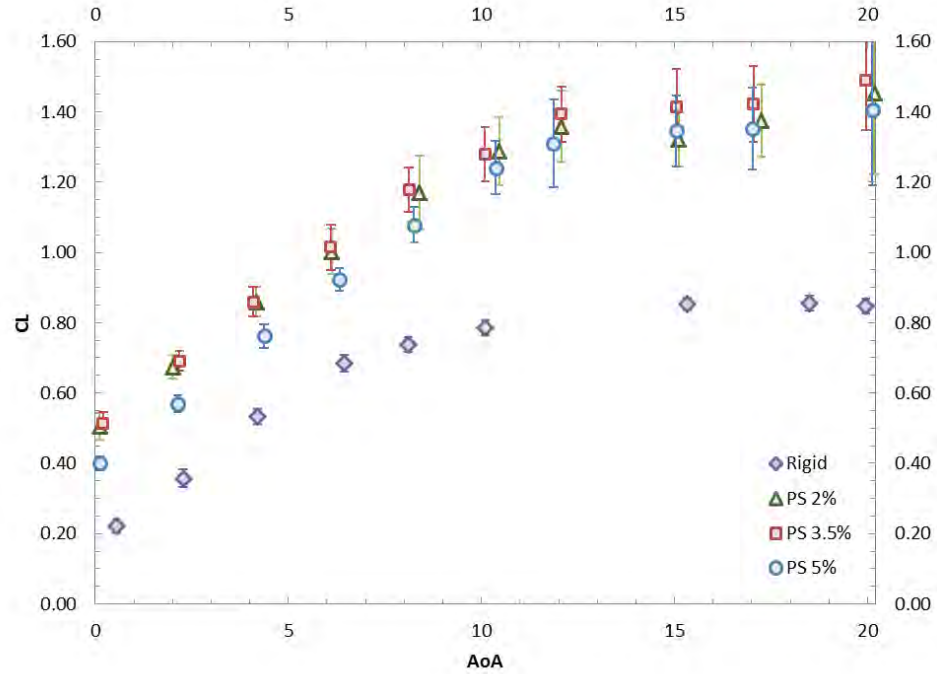
FIGURE 2.7: Comparison of coefficients of lift versus AOA; wind tunnel testing for wings with various membrane pre-tensions at 18 m/s or Re $9 \cdot 10^4$, compared to rigid wing as a reference.

2.6.2 Surface Reconstruction

For the three different membranes at 2, 3.5 and 5 nominal percent pre-strain, VIC images were taken at 3, 6 and 9 degrees AOA and each at a flow velocity of 12, 15 and 18 meters per second. A sample of one data set for a 2% pre-strain wing at 6 degrees AOA and 18 m/s can be seen on the left side of Fig. 2.8. Using this data, strain sensors were created with quantity, size and positions as defined in Table 2 and are visualized by the "patches" in Fig. 2.8(b) and Fig. 2.9. Full field error of the reconstructed surface

compared to the actual membrane surface as measured using VIC, can be seen in the center of Fig. 2.8. These results are favorable and show less than 10% error for max residual with respect to maximum deflection.

Comparing normalized camber, z/c, (where $z = \alpha \cdot 1$ mm, and c being the wing chord length in millimeters) of the reconstructed surface to that of the actual surface, as measured by VIC, shows favorable results. Values of camber for a single membrane at different AOA and wind velocities can be seen in Fig. 2.10, which shows relatively accurate values of reconstruction compared to that of the actual membrane. It can be seen that, while the estimate of the max deflection is quite accurate, it begins to deviate at higher AOA due to the fact that the surface departs from a quadratic shape. It can also be seen that an expected increase of camber with respect to velocity and with respect to AOA occurs, while an expected reduction of camber occurs with respect to increased pre-strain.
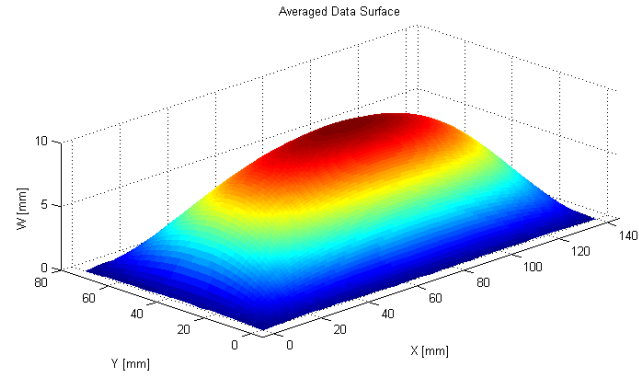
(a)
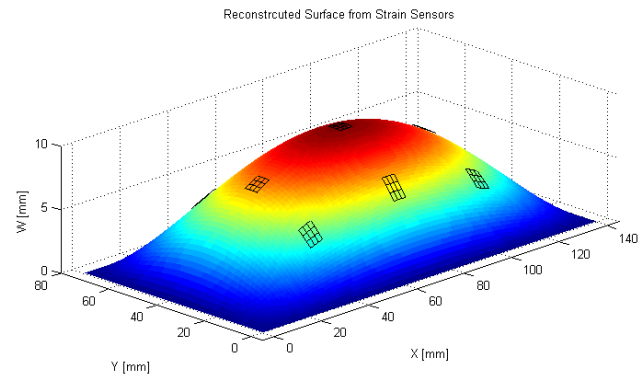
(b)
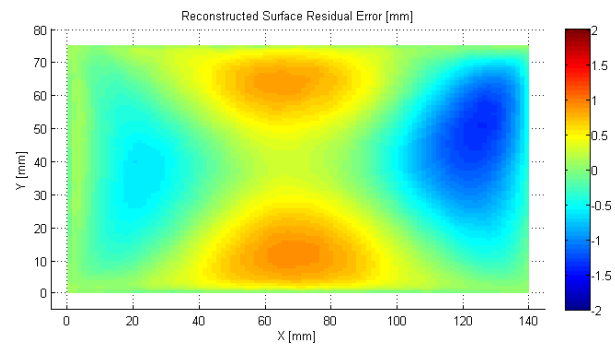
(c)

FIGURE 2.8: Comparison of membrane out-of-plane deformation for one half of the wing; VIC data (a) and quadratic surface reconstruction from pseudo strain sensors (b); Residual error from out-of-plane deformation of VIC data and reconstructed surface (c).

TABLE 2.2: Strain Sensor Configuration

Sensor	w [mm]	h [mm]	2x/b	y/c
1			0.5	0.5
2			0.5	0.2
3			0.5	0.8
4			0.25	0.5
5	5	5	0.25	0.2
6			0.25	0.8
7			0.75	0.5
8			0.75	0.2
9			0.75	0.8
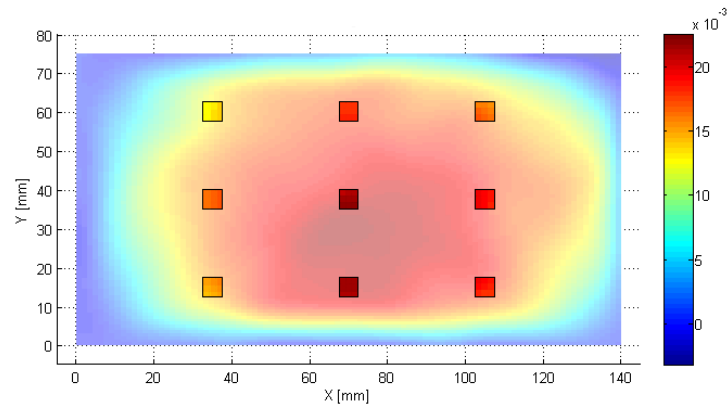
FIGURE 2.9: Representation of strain sensors from Table 2.2, derived from full field VIC total strain $(\epsilon_x + \epsilon_y)/2$.

(a)

(b)
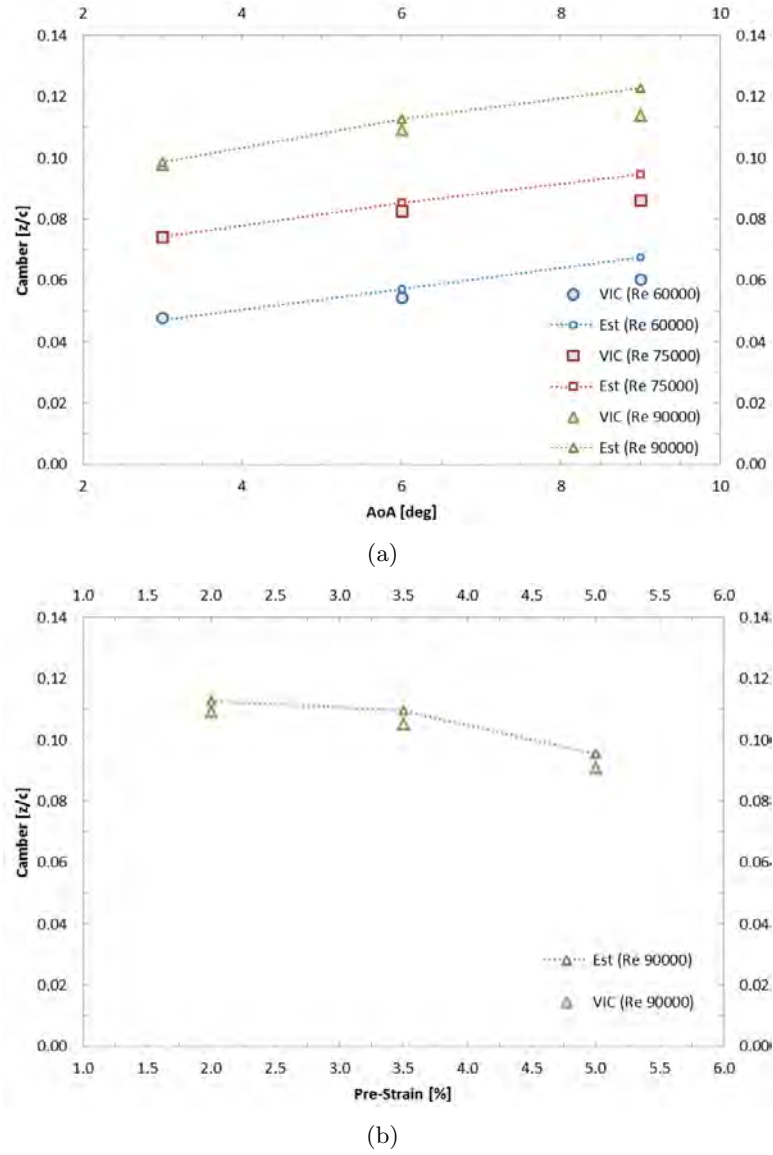
FIGURE 2.10: Comparison of normalized camber z/c versus AOA, between actual deflection (VIC) and strain sensor reconstruction (Est) for a 2% pre-strain membrane at different Re (a); a comparison of normalized camber versus amount of pre-strain, between actual deflection (VIC) and strain sensor reconstruction (Est) for a wing at 6 degrees AOA.

2.6.3 Material Characterization

To derive the tension fields created from pre-strain in the membrane, the elastic modulus of the latex material was determined empirically. A 25 mm by 100 mm speckled

sample of latex was vertically suspended in front of the same aforementioned VIC cameras system. In this test, weights were applied to one end of the latex and images were taken for each weight. Full field VIC strains were determined for each load. Due to the hyperelastic behavior of latex, the modulus was not constant throughout deformation. For this reason, a quasi-linear region is considered between the values of lowest pre-strain and max expected induced strain from loading. For this test, strains between 2 and 10 percent were observed, thus the modulus of elasticity was assumed to be linear in this region and yielded a magnitude of 1.14 MPa. Since VIC data also provides lateral strain as well as longitudinal strains, the Poisson ratio could be readily determined and was found to be 0.39.

2.6.4 Lift Calculation

Using the data collected and methods described above, lift estimations were calculated for the membrane wings. Load estimates as compared to actual loads measured during wind tunnel testing can be seen in Fig. 2.11. As can be easily observed, all load estimates/calculations are less in magnitude than the measured values. This is to be expected due to the low order nature of the methods employed. Comparing the force resultant from the CFD model to measured data, where the CFD value was derived from the integration of the numerical pressure gradient over the entire meshed wing surface, yields a result with a constant error offset of $\sim 15\%$ at 6 degrees AOA. This result provides confidence that the majority of the wake flow energy is present in the simulation and was captured by the reconstructed membrane surface.
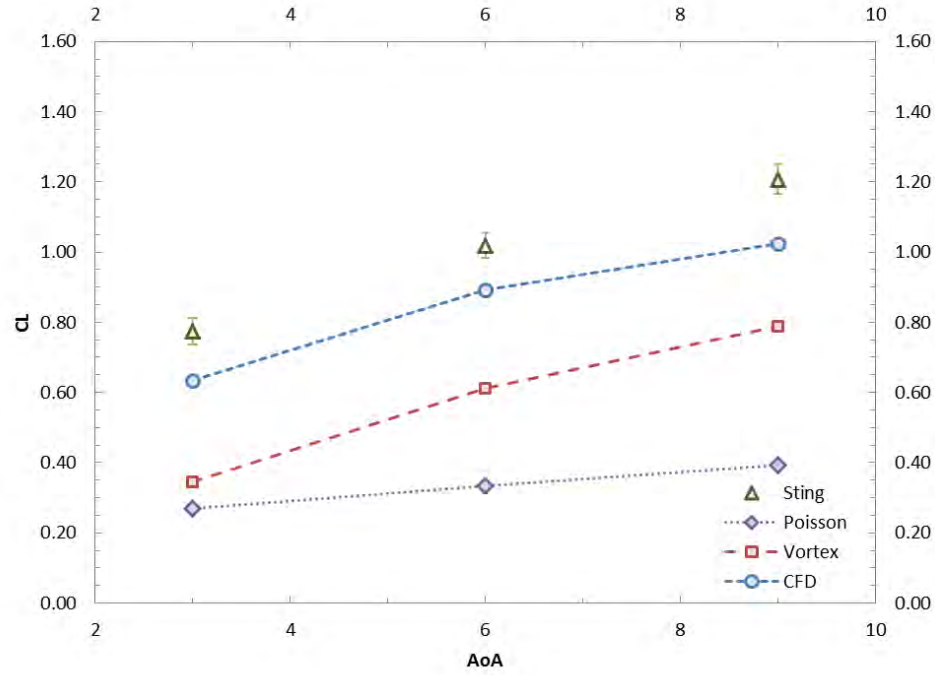
FIGURE 2.11: Comparison of aerodynamic load generated at different AOA for a 2% pre-strained wing using various force measuring/estimating techniques; sting balance measurement from wind tunnel tests, force calculation from CFD, force estimation from tip vorticity, and force estimation from Poisson model.

Next, the lift estimation from vorticity is observed. It can be seen that the force estimation increases with the same slope as that of the actual lift but is again off by a constant offset of ∼50% at 6 degrees AOA. This can be attributed to many factors, i.e. theoretical model fidelity and numerical model fidelity, but is likely most significantly affected by the fact that the tip vortex does not contain the complete lift circulation energy and will therefore not be completely capable of providing the full force estimation. Nevertheless, this behavior can certainly be correlated to tangible lift values, derived from strain and vorticity, through the inclusion of a constant offset applied to the result. This offset would likely be a constant value which would vary for different wing geometries.

Finally, the behavior of the force estimation from the Poisson model is observed. Here it can be seen that, the estimation behaves in a significantly different way from the previous estimation. In this case the model has a proportional error of approximately

66%. This allows us to conclude that the force estimation is off by a constant multiple as opposed to the constant offset seen by the vorticity estimation. This again gives rise to a correlatable lift estimation through the inclusion of a constant multiplied to equation 2.14.

2.7. Conclusion

In this study, lift was estimated for a pliant membrane wing using structural strain information, analogous to proprioceptive sensing found in biological fliers. Wind tunnel tests of three membrane wings, each at different membrane pre-strain values, were conducted; aerodynamic loads, membrane deformations and membrane strains were measured. Using a pseudo strain sensor configuration from VIC data and a basic analytic model, the membrane surface was reconstructed to a reasonable order of accuracy. A numeric fluid model was applied to this reconstructed surface to solve for wing tip vorticity behavior in the near wake field of the wing. Calculating the circulation from the tip vortex, lift could be directly derived using assumptions from linear aerodynamic theory.

Results from this approach gave favorable lift predictions. For a given membrane wing, it was observed that changes in the wing's structural state, due to changes in AOA and flow velocity, generated correct behavior in estimated lift as compared to actual measured lift. Absolute values of estimated lift were offset from actual values due to the assumptions applied and due to wing tip vortices not capturing the entirety of the wing circulation energy. Nevertheless, using a low order approximation of structural state and flow state, a distinct correlation between strain, vorticity and lift was made within the bounds of this study.

2.8.   Future Work

This work has strongly encouraged future research in a variety of ways. First, the assumptions that were used in formulating the overall estimation problem were fairly extensive. This was the goal of the present work; however it encourages future research which refines the assumptions made. Most significantly for this study was the use of a quadratic basis function for the deformed membrane surface. It is known that an infinite Fourier series solution can describe such a surface, thus to increase accuracy of the estimation, higher order terms could be incorporated into the basis function. An investigation of the trade-off of more complex flow and pressure state solver options versus simple aerodynamic principles should also be investigated in the future. Perhaps coupling of a panel solver to a finite element membrane model with strain estimation could yield an algorithm which uses both aerodynamic and structural theory to minimize the estimate error of both load and structural deformation in an iterative fashion.

2.9.   Acknowledgments

The authors would like to thank the support of the Air Force Office of Scientific Research, Flow Control & Aeroelasticity under Contract FA9550-10-1-0325, with Douglas R. Smith as project monitor and the Air Force Office of Scientific Research under the Multidisciplinary University Research Initiative grant FA9550-07-1-0540. The authors would also like to acknowledge Dr. Belinda Batten's continuous and critical support to the project and the University of Florida for assistance with contractual aspects.

Aerodynamic Load Estimation from Virtual Strain Sensors for a Pliant Membrane Wing

Trenton Carpenter, Roberto Albertani

3. AERODYNAMIC LOAD ESTIMATION FROM VIRTUAL STRAIN SENSORS FOR A PLIANT MEMBRANE WING

3.1. Abstract

An approach has been developed to utilize the strain sensed in a membrane wing to estimate aerodynamic loads. Through experimental and theoretical correlation of membrane strain state due to a normally distributed load, the pressure over the surface of the wing was estimated. Elastic deformations and strains of the membrane wing were measured in a low-speed wind tunnel using digital image correlation (DIC). Simultaneously, aerodynamic loads were measured using a six component load cell, inclinometer, and pitot tube. DIC displacement measurements were used to form a reduced order model of the membrane displacements via a snapshot proper orthogonal decomposition (POD) method. DIC strain measurements were used to form virtual strain sensors, which served as the sensory input to the estimation. The Poisson equation for a 2D linear-elastic membrane with out-of-plane deformation was used to calculate the normal pressure distribution from virtual strain sensors using POD basis functions and a recursive least squares minimization. Estimated pressure distributions were compared to a high fidelity 3D computational fluid dynamic model and pressures calculated from DIC deformations. Coefficients of lift and pitching moment for steady state flow conditions were estimated, and compared to, measured wind tunnel loads. Results show promise toward the application of a low fidelity estimation approach for real-time load estimation applications.

Nomenclature

α	Angle of attack [°]
Ω	Membrane domain
u	Membrane displacements in x-direction [m]

v Membrane displacements in y-direction [m]
w Membrane displacements in z-direction [m]
ε Strain Measurement [%]
ϵ Strain Estimate [%]
f Interpolant function
P Pressure, $[N]$
T Membrane tension, $[N/m]$
E Modulus of elasticity, $[Pa]$
ν Poisson ratio
h Membrane thickness $[m]$
ρ Membrane density $\left[kg/m^3\right]$
γ Viscous dampening parameter $[Ns/m]$
η Viscoelastic dampening parameter $\left[Ns/m^2\right]$
σ Standard deviation
U_{inf} Free stream flow velocity $[m/s]$
C_L Coefficient of lift
C_m Coefficient of pitching moment

3.2. Introduction

Herein, we present an estimation approach which uses structural state feedback from the deformation of a membrane, in the form of strain to predict aerodynamic loads experienced by the wing. A formulation using the Poisson equation is used to correlate membrane strain to a normally distributed pressure. A reduced order model of the membrane out-of-plane displacement is developed using proper orthogonal decomposition (POD) from digital image correlation (DIC) measurements. Full-field DIC strain measurements are partitioned into small area "patches" to create virtual strain sensors which serve as the input to the estimation. Using an elliptical partial differential equation, the classic Poisson equation for a membrane, and the reduced order model of the membrane displacement, a recursive least squares minimization is used estimate normally distributed pressure on the membrane. From the estimated pressure, lift and pitching moment are calculated. Steady air flow in a wind tunnel, and hydrostatic pressure in a test jig, are the

experimental conditions used to evaluate the estimation approach. An incompressible, time invariant, computational fluid dynamic (CFD) model of a rigid cambered airfoil, where camber is defined by time averaged DIC measurements, is developed as a comparative tool. Finally, estimated pressures and aerodynamic loads are compared to CFD calculations and experimental measurements.

Various load estimation strategies have been applied to membrane wings within literature which have similarities to the one presented here. Schmit and Glauser [77, 94] correlated strain measured in the frame of a membrane wing to a reduced order model of the wake flow developed with particle image velocimetry (PIV) measurements and proper orthogonal decomposition. By solving an inverse problem, Stanford et. al. [95], estimated the normal pressure distribution over the surface of a membrane wing with a multi-order polynomial as a basis for the pressure distribution. A least-squares minimization was used to minimize the error between measured membrane displacements and a finite element mesh. Waldman et. al. [3, 6] and Song et. al. [2] used a Poisson formulation for a membrane subjected to a uniform pressure distribution to develop nondimensionalized aero-elastic parameters for predicting the general deformation of a membrane due to steady air flow and constant pretension. Dickinson et. al. [96] evaluated an approach to solving general elliptical partial differential equations from noisy membrane displacement sensors. Ray [8] used an approach to calculate distributed pressure on a membrane from noisy structural sensors using regularization, finite elements, and a Kalman filter. Stanford et. al. [97] investigate fundamental phenomena occurring with a clap and fling membrane wing, using proper orthogonal decomposition (POD) of the wing displacement as a tool for analysis. Ray and Albertani [8], and Carpenter et. al. [98], measured strains produced on a membrane wing due to steady flow conditions and developed a correlation between membrane strain and wing tip vorticity to estimate circulation and lift.

Within the body of literature, limited work has been conducted using strain sensors to estimate aerodynamic loads on a membrane wing with a reduced order model. The mo-

tivation for this work was two fold. First, was developing an approach which utilized strain sensor, rather than displacements, to estimate aerodynamic loads. Second, we sought to explore the accuracy of a low fidelity estimation approach for future development toward real-time estimation applications. In this paper, we present the analytic formulations of the approach, our experimental procedures are explained, estimated values are compared to experimental measurements and numeric models, and results found are discussed.

3.3.   Methods

The approach used in this work utilizes the elastic deformation experienced by a membrane wing during flight, to estimate the normally distributed pressure on the surface of that membrane. Since a body exposed to a fluid flow can experience components of loads due to both normal and shear fluid forces, accounting for both force components is required for a complete model. Although for this work, it is assumed that the normal component of load on the membrane surface has a significantly greater effect on membrane deformation compared to the shear component. To simplify the formulation of loads on the wing, the shear component of the fluid force is neglected. In order to estimate the normally distributed pressure, $P(x, y)$, using inputs from strain, i.e., $P(\varepsilon_{xx}(x, y), \varepsilon_{yy}(x, y))$, a relationship between the load, displacements, and strain was defined.

3.3.1   Membrane Wing

Consider a rectangular planform wing, comprised of two perimeter reinforced, thin flexible membranes, one on each side of center-line. Each membrane cell was under a constant predetermined amount of pre-tension, subjected to an unknown normally distributed load defined as $P(x, y)$. On this wing, consider a Cartesian coordinate system, with a domain Ω where $0 \leq x \leq a$ and $0 \leq y \leq b$. The rigid perimeter of the membrane creates a zero Dirichlet boundary condition for $u(x, y)$, $v(x, y)$ and $w(x, y)$, the non-rigid-

body displacements in the x, y and z directions respectively. The configuration of the wing can be seen in Fig. 3.1, where the dark gray regions represent the "rigid" metal frame of the wing and the light gray regions represent the pre-tensioned membrane.
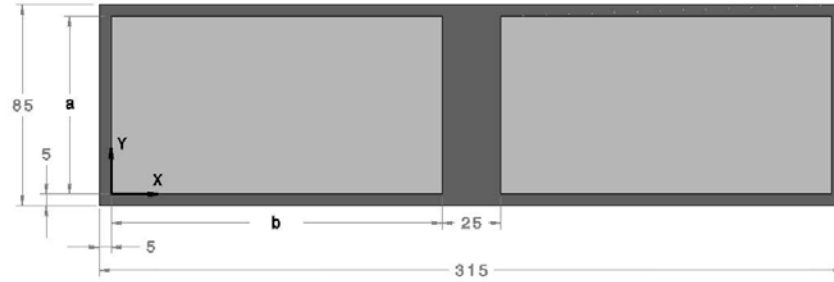
FIGURE 3.1: Schematic of the membrane wing used in the study, where the dark gray regions represent the metal frame and the light gray regions represent the pre-tensioned membrane. All dimensions shown in millimeters.

3.3.2 Virtual Strain Sensors

As an input to the load estimation problem, a finite number of directional virtual strain sensors, generated from full field DIC strain measurements, were dispersed throughout the membrane domain Ω. Using virtual strain sensors made for a convenient and practical approach for creating any desired sensor configuration with the same data sets. Ultimately, strain sensors embedded in the membrane could be used to collect the same information in real-time during in-flight conditions. For the duration of this work, the idealized virtual strain sensor will be considered as a pseudo real-time sensor input.

Virtual strain were created by taking an integral average of experimental, full-field strain measurements, over the sub-domain of the sensor. For this problem, shear strains comprised a small percent of the total strain energy and was predominately concentrated in the corners of the domain, away from the strain sensor locations. For this work, shear strains were neglected for the formulation of the sensor measurement. The process for acquiring these measurements can be found in Section 3.4.

More specifically, if $\varepsilon_{xx_{dic}}(x,y)$ and $\varepsilon_{yy_{dic}}(x,y)$ represent the experimentally measured full-field DIC strain over the domain Ω in the x and y directions respectively, and

Ω_i represents the rectangular domain of the individual ith sensor, then the magnitude of a single virtual strain measurement for a given location (x_i, y_i) is defined as,

$$\varepsilon_{xx_i} = \frac{1}{\Omega_i} \int_{\Omega_i} \varepsilon_{xx_{dic}}(x, y) \, \mathrm{d}x \, \mathrm{d}y \tag{3.1}$$

$$\varepsilon_{yy_i} = \frac{1}{\Omega_i} \int_{\Omega_i} \varepsilon_{yy_{dic}}(x, y) \, \mathrm{d}x \, \mathrm{d}y. \tag{3.2}$$

Using Eq. 3.1 and 3.2, a scalar value for strain is given for each (x_i, y_i) location and a strain sensor vector can be constructed for n number of strain sensors,

$$\boldsymbol{\varepsilon}_{sensor} = \left\{ \varepsilon_{xx_1} \ \cdots \ \varepsilon_{xx_n} \ \varepsilon_{yy_1} \ \cdots \ \varepsilon_{yy_n} \right\}. \tag{3.3}$$

Eq. 3.3 serves as the sensor input to the load estimation problem.

With the strain sensor measurements, the first step in the estimation is to reconstruct the full-field strain over the domain of the membrane. This will help alleviate issues with the least squares optimization algorithm (to be discussed later) settling on a local error minimum rather than the solution's global error minimum. This is of significance, since the spacial quantity of strain sensors is significantly smaller than the discretization of the solution. This will also prove to be useful for comparison later when the methods for calculating pressure are applied to both the estimated values of ϵ_{xx}, ϵ_{yy} and the DIC measurements of ε_{xx}, ε_{yy}.

3.3.3 Strain Field Estimation

To estimate the full-field distribution of ϵ_{xx} and ϵ_{yy} within the domain Ω, a reduced order model was created using a linear combination of polynomials, found to best fit the full-field DIC strain measurements. These functions were empirically chosen such that they conformed to the natural boundary conditions of ϵ_{xx} and ϵ_{yy}, allowed the solution to take the general form of the actual strain fields observed within the study, and formed an orthonormal basis.

The basis $f(c_i, x, y)$, is a linear combination of m number of weighted functions defined as,

$$f_{\epsilon_x} = \sum_{i=1}^{m} c_{\epsilon_x i} g_{\epsilon_x i}(x, y) \tag{3.4}$$

$$f_{\epsilon_y} = \sum_{i=1}^{m} c_{\epsilon_y i} g_{\epsilon_y i}(x, y) \tag{3.5}$$

where c_i is the ith weighting coefficient for the ith basis function $g_i(x, y)$.

The same integral averages, over the same sensor sub-domains, are taken from f_{ϵ_x} and f_{ϵ_y}, forming a vector strain estimate similar to that defined in Eq. 3.3,

$$\boldsymbol{\epsilon}_{interp} = \begin{Bmatrix} \frac{1}{\Omega_i} \int_{\Omega_i} f_{\epsilon_x 1} \, \mathrm{d}x \, \mathrm{d}y \\ \vdots \\ \frac{1}{\Omega_i} \int_{\Omega_i} f_{\epsilon_x n} \, \mathrm{d}x \, \mathrm{d}y \\ \frac{1}{\Omega_i} \int_{\Omega_i} f_{\epsilon_y 1} \, \mathrm{d}x \, \mathrm{d}y \\ \vdots \\ \frac{1}{\Omega_i} \int_{\Omega_i} f_{\epsilon_y n} \, \mathrm{d}x \, \mathrm{d}y \end{Bmatrix}. \tag{3.6}$$

Using Eq. 3.3 and Eq. 3.6, a relationship between the strain sensors and strain estimates is formed,

$$\boldsymbol{\varepsilon}_{sensor} = \boldsymbol{\epsilon}_{interp} + \eta \tag{3.7}$$

where η represents the error between the measured values of strain and the estimated values of strain for a given patch location. Utilizing the Nelder-Mead method, a least squares minimization approach, the system error η is minimized through manipulation of the interpolant's weighting coefficients c_i. Further discussion of this method can be found in [99, 100]. With the weighted coefficients, estimated full-field strain values are obtained from f_{ϵ_x} and f_{ϵ_y} defined by Eq. 3.4 and 3.5. An example of results from this approach can be seen later in this paper, in Sec. 3.5., Fig. 3.7.

3.3.4 Membrane Model

To develop a relationship between strain, displacements, and load, a force balance can be invoked on a differential element of the membrane. Figure 3.2 shows these forces on a differential element, where T_x and T_y are equal to the tension per unit length within the membrane, θ and ψ are the angles the membrane makes with the x and y axis respectively, w is the out-of-plane displacement of the membrane, h is the thickness of the membrane, and $P(x, y)$ is the normal pressure distribution applied to the membrane.
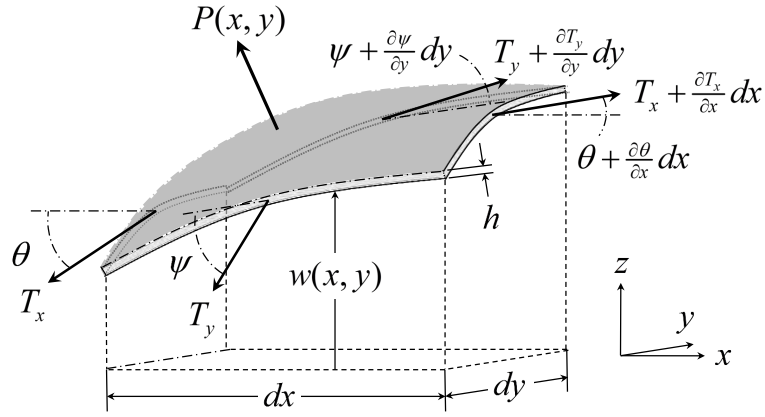
FIGURE 3.2: Internal reaction forces for an infinitesimal element of a thin membrane acted on by a normal pressure distribution.

By summing the vertical static and inertial forces acting on the differential element of the membrane and applying small angle approximations, the following relationship can be found,

$$\rho h \frac{\partial^2 w}{\partial t^2} - \gamma \frac{\partial w}{\partial t} - \eta \left(\frac{\partial^3 w}{\partial t \partial x^2} + \frac{\partial^3 w}{\partial t \partial y^2} \right) - \left[T_x \frac{\partial^2 w}{\partial x^2} + T_y \frac{\partial^2 w}{\partial y^2} + \frac{\partial T_x}{\partial x} \frac{\partial w}{\partial x} + \frac{\partial T_y}{\partial y} \frac{\partial w}{\partial y} \right] = P(x, y, t)$$

(3.8)

where ρ is the membrane material density, γ the viscous damping parameter and η the Kelvin-Voigt viscoelastic damping parameter. A more complete derivation of these damping parameters can be found in [8]. Equation 3.8, is a function of the internal tension terms

$T_x(x, y)$ and $T_y(x, y)$, as well as the first and second, spatial and temporal, gradients of the out-of-plane displacement $w(x, y)$. The tension terms $T_x(x, y)$ and $T_y(x, y)$ are due to both pre-stretching of the membrane as well as strains experienced due to deformation. To solve for $P(x, y)$, it is required that the amount of membrane pre-stretching, membrane material properties, and state of membrane deformation are known.

Assuming the membrane material follows a linear-elastic constitutive relationship, a reasonable assumption for low levels of strain [101], the material's modulus of elasticity and Poisson ratio are given as E and ν respectively. The pre-stretching prescribed to the membrane, which is always ≥ 0, is assumed to be constant. From DIC measurements of prestrain, values at a nominal prestrain of 2% were measured to have a full field average and standard deviation of $\epsilon_{PS_x} = 2.04 \pm 0.21$ and $\epsilon_{PS_y} = 2.22 \pm 0.27$. The measurement variability was found to be adequately uniform throughout the domain of the membrane, and was attributed to local variations in material properties, any non-uniformity in the prestrain stretching technique, and noise in the DIC measurements. For this work, these variances are neglected, and the spatial average of full-field DIC measurements were used to define ϵ_{PS_x} and ϵ_{PS_y} as constants. With this information, the internal tension can be defined as,

$$\begin{bmatrix} T_x \\ T_y \end{bmatrix} = \frac{Eh}{(1 - \nu^2)} \begin{bmatrix} 1 & \nu \\ \nu & 1 \end{bmatrix} \begin{bmatrix} \epsilon_{xx} + \epsilon_{PS_x} \\ \epsilon_{yy} + \epsilon_{PS_x} \end{bmatrix} \tag{3.9}$$

where ϵ_{xx} and ϵ_{yy} are the strains developed due to the deformation of the membrane. From linear elastic theory, ϵ_{xx} and ϵ_{yy} are commonly defined as,

$$\begin{aligned} \epsilon_{xx} &= \sqrt{1 + 2\frac{\partial u}{\partial x} + \left(\frac{\partial u}{\partial x}\right)^2 + \left(\frac{\partial v}{\partial x}\right)^2 + \left(\frac{\partial w}{\partial x}\right)^2} - 1 \\ &\approx \frac{\partial u}{\partial x} + \frac{1}{2}\left[\left(\frac{\partial u}{\partial x}\right)^2 + \left(\frac{\partial v}{\partial x}\right)^2 + \left(\frac{\partial w}{\partial x}\right)^2\right]. \end{aligned} \tag{3.10}$$

$$\epsilon_{yy} = \sqrt{1 + 2\frac{\partial v}{\partial y} + \left(\frac{\partial u}{\partial y}\right)^2 + \left(\frac{\partial v}{\partial y}\right)^2 + \left(\frac{\partial w}{\partial y}\right)^2} - 1$$
$$\approx \frac{\partial v}{\partial y} + \frac{1}{2}\left[\left(\frac{\partial u}{\partial y}\right)^2 + \left(\frac{\partial v}{\partial y}\right)^2 + \left(\frac{\partial w}{\partial y}\right)^2\right] \tag{3.11}$$

Note, a first order Taylor series approximation was used in Eq. 3.10 and 3.11. In traditional membrane problems, out-of-plane displacements are often assumed to be "small" and the in-plane displacements u and v are assumed to be negligible. Using this assumption, the strains developed in Eq. 3.10 and 3.11 simplify to be only a function of $\partial w/\partial x$. It has been observed in this study that the strain produced via the in-plane deformations components u and v are significant. Thus this assumption causes significant errors in the correlation of strain to displacement and ultimately the estimation of $P(x, y)$. Yet the alternative does not represent a highly desirable case for real-time applications either, since including u and v in the formulation of Eq. 3.8 creates an under-determinant, non-linear, partial differential equation. In an effort to preserve u and v within the formulation and at the same time keep Eq. 3.8 a determinant problem, an empirical relationship was formed such that $u(x, y)$ and $v(x, y)$ was defined as a function of $w(x, y)$; or $u(w(x, y))$ and $v(w(x, y))$. For a given location, (x, y), the arc length of $w(x, y)$, from 0 to a value x, in the x direction can be defined as,

$$S_x(x, y) = \int_0^x \sqrt{1 + \left(\frac{\partial w(x, y)}{\partial x}\right)^2} \, dx. \tag{3.12}$$

With this definition for arc length, the in-plane deformation[1] $u(x, y)$ can then be approximated as,

$$u(x, y) = x - x^* \text{ for,} \tag{3.13}$$

$$\frac{S_x(x, y)}{S_x(a, y)} = \frac{x^*}{a} \Rightarrow x^* = a\frac{S_x(x, y)}{S_x(a, y)} \tag{3.14}$$

---

[1]The relationships developed in Eq. 3.15 & 3.17 are derived through empirical inference.

$$u(x,y) = x - a\frac{S_x(x,y)}{S_x(a,y)}.$$ (3.15)

Similarly, the arc length in the y direction, and the in-plane deformation $v(x,y)$, can be approximated as,

$$S_y(x,y) = \int_0^y \sqrt{1 + \left(\frac{\partial w(x,y)}{\partial y}\right)^2} \, dy$$ (3.16)

$$v(x,y) = y - b\frac{S_y(x,y)}{S_y(x,b)}$$ (3.17)

Given Eq. 3.9, 3.15 & 3.17, the pressure distribution in Eq. 3.8 can be found if $w(x,y)$, and its derivatives are known. Moreover, it can be observed that every variable within the formulation of Eq. 3.8 is ultimately a function of $w(x,y)$. Therefore, once $w(x,y)$ is found, any number of differentiation and integration schemes can be utilized to solve Eq. 3.8 for the pressure distribution $P(x,y)$. For this work, a second order accurate, explicit, finite difference scheme was used for both integration and differentiation.

3.3.5 Surface Deformation Estimation

To estimate the membrane deformation $w(x,y)$ from strain sensor input, a method similar to that used in Section 3.3.3 was employed. A reduced order model with a least squares estimator, applied to the formulation above, was used to approximate the true surface deformation. To form the basis, a method of snapshot proper orthogonal decomposition (POD) was used similar to [71, 102]. POD was applied to the time varying DIC measurements of $w(x,y)$ for all testing conditions. It was found that the first four POD modes comprised 99.8% of the original system energy. These modes, as seen in Fig. 3.3, became the basis set used as the interpolant for estimating $w(x,y)$.

The interpolant $f(c_i, x, y)$, is expressed as a linear combination of $p = 4$ basis functions and was defined as,

$$f_w = \sum_{i=1}^{p} c_{wi} g_{wi}(x,y)$$ (3.18)
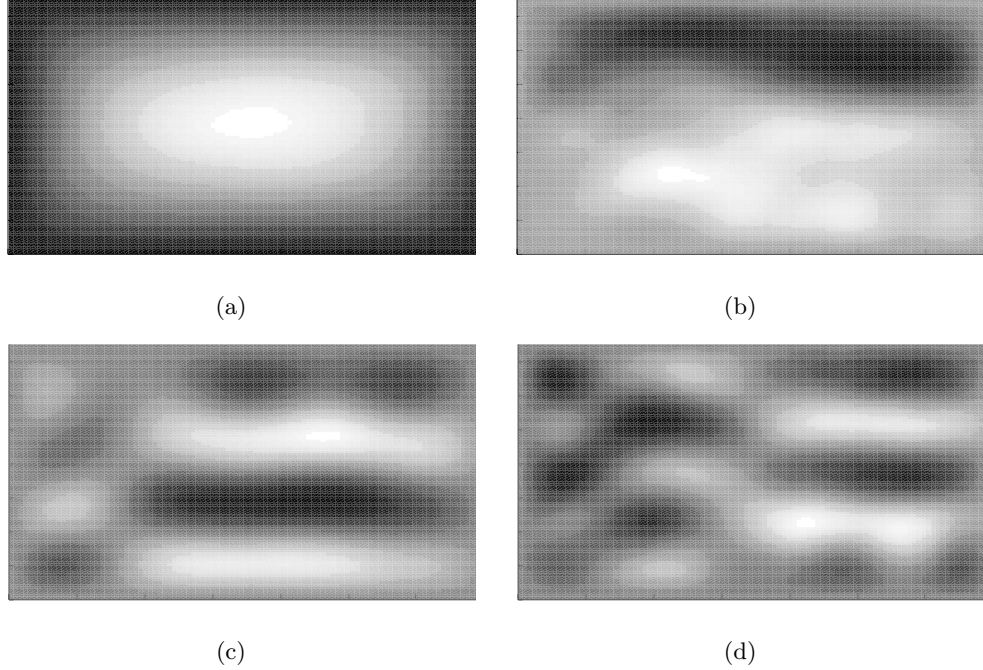
FIGURE 3.3: First four POD modes of $w(x, y)$ used to form the set of basis to estimate out-of-plane deformation. Contour plots (a)-(d) represent POD mode 1-4 respectively.

where c_{wi} is the ith weighting coefficient for the ith basis function, $g_{wi}(x, y)$. With Eq. 3.18, the estimation of the strain field from the membrane deformation is now possible. By substituting Eqs. 3.15, 3.17 and 3.18 into Eqs. 3.10 and 3.11, and numerically integrating and differentiating as necessary, full-field strain interpolants for ϵ_{xx} and ϵ_{yy} were developed simply as a function of c_{wi}, which can be represented as, $f_{w_x}(c_{wi})$ and $f_{w_y}(c_{wi})$. A relationship to find the interpolant's weighting coefficients can now be formed in the same manner as that in Eq. 3.7,

$$\begin{Bmatrix} f_{\epsilon_x} \\ f_{\epsilon_y} \end{Bmatrix} = \begin{Bmatrix} f_{w_x}(c_{wi}) \\ f_{w_y}(c_{wi}) \end{Bmatrix} + \eta \tag{3.19}$$

where, in this case, η represents the error between the estimated strain distribution (derived from the strain sensors) and the derived strain values from the estimated surface deformation. Applying the same least squares optimization approach as before, the weight-

ing coefficients, c_{wi} from Eq. 3.18 are found and an estimate of the out-of-plane deformation, $w_{est}(x, y)$ is generated. Now, $w_{est}(x, y)$ and its subsequent derivatives, can be substituted into Eq. 3.8 and 3.9, in order to calculate the pressure distribution $P(x, y)$ over the membrane domain Ω.

3.4.   Experimental Setup

In this approach, the source from which the loads on the membrane originate are irrelevant from a structural analysis standpoint. What is of consequence to solving the structural problem is simply the total pressure difference between the upper and lower surface of the membrane. In order to evaluate the validity and accuracy of the method proposed above, the pressure estimation must be compared to a known pressure state before comparing to a highly dynamic and unknown pressure state as that induced by a fluid flow over a wing. For this reason, two experiments were conducted to provide different loading scenarios for the estimation routine to evaluate. The first was a hydrostatic pressure case, where a pre-tensioned membrane was subjected to a steady, evenly distributed, known pressure. DIC measurements of strain and deformation were taken of the deformed membrane. A pressure transducer measured the magnitude of gauge pressure applied to the membrane surface. In the second scenario, the membrane wing, defined in Fig. 3.1, was placed in a low speed wind tunnel and subjected to various steady conditions of wind speed and angle of attack. Aerodynamic loads generated by the wing were measured, and DIC measurements of the membrane deformation were taken. A time invariant CFD model was created of the wing in each condition in order to have a numerical approximation of the pressure distribution as a basis for comparison.

3.4.1 Digital Image Correlation

Full-field measurements of strain and deformation were performed using a digital image correlation (DIC) technique [92, 93]. Images were captured with two high-speed AOS S-PRI cameras, capable of 1,000 frames per second (fps) and capable of saving 1,000 frames at a resolution of 1280x1024 pixels in an in-camera flash-memory buffer. The cameras were positioned above the membrane, approximately perpendicular to the membrane surface, with a stereoscopic angle of approximately 40° between cameras. For the wind tunnel experiment the cameras were mounted outside and above the wind tunnel and viewed through a clear window. Cameras were calibrated while viewing through the windows, correcting for distortion effects from the windows themselves. The DIC reference images were of the membrane subject to no load (zero wind velocity). Since this condition was used to take the reference images, the pretension did not appear directly in the DIC results. However, pretension was measured for each test specimen using the DIC system prior to being fixed to the metal wing frame or the static pressure test pane.

| (a) | (b) |
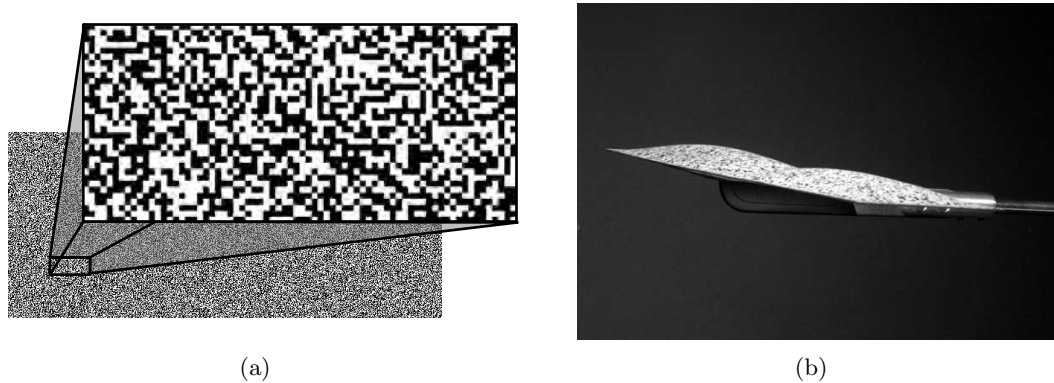
FIGURE 3.4: (a) Random digital pattern printed on the surface of the latex membrane used for DIC measurements. (b) Speckled membrane wing showing out-of-plane deformation during wind tunnel testing (air flow from left to right).

To create a test specimen, an over sized, bare latex sheet was "speckled" with a random digital pattern printed on by an laser printer; an example of which can be seen in Fig. 3.4(a) and 3.4(b). For each experiment, the overall size of the digital pattern

was customized for the given camera arrangement. The pattern was scaled such that the average "speckle" object size was approximately 5x5 pixels as seen by the cameras. Within each image, the area of interest, or domain Ω, was approximately 700x350 pixels, equating to, on average, 0.2 mm per pixel and an average object size of 1x1 mm. The subset window size was set to 40x40 pixels which contained an average 15 to 20 identifiable objects. The step over size was set to 10 px, or a 25% step over, equating to approximately 2400 interpolated data points over the area of interest.

3.4.2 Hydrostatic Pressure Test

In order to provide a well known loading condition for the estimation routine to compute, a hydrostatic pressure test was devised. The geometry of the pressure test membrane domain was identical to that of a single membrane wing domain shown in Fig. 3.1. Each specimen was speckled, prestrained, and attached to a rectangular plexiglass plate, creating a single membrane test pane. Prestraining of the membrane was accomplished with a custom designed stretching apparatus and measured using imaging and DIC. These test panes were then fixed to a plexiglass plate with a vacuum sealant tape. The plexiglass plate had two ports with access to the sealed chamber behind the membrane. One of these ports was attached to the positive side of a differential pressure transducer, while the negative side was exposed to atmospheric pressure. The second port was connected to a syringe, which when displaced would reduce the volume within the sealed chamber, creating a positive pressure and deforming the membrane. Images were taken of the deformed and undeformed membrane surface, and pressure readings were taken for each image. Nominal pressure values recorded for this test were between 100 Pa and 500 Pa in increments of 100 Pa. The pressure test utilized vacuum bag sealant tape to seal the membrane to the fixture, creating a near perfect seal. Pressure readings maintained constant pressure at one tenth of a Pascal with no observable change due to leaking over the period of time that the measurements were taken. The hydrostatic

pressure test, pressure transducer, and DIC cameras can be seen in Fig. 3.5(a).

3.4.3   Wing Tunnel Experiment

The wind tunnel used to conduct all experiments was a low-speed wind tunnel at Oregon State University. The wind tunnel had a closed loop, closed test section, capable of speeds from 1 to 18 meters per second (m/s) and with a 1.3 x 1.5 meter test section, as seen in Fig. 3.5(b). The installation of the test wing can also be seen mounted to a one degree of freedom model armature inside the test section. The model armature was used for angle of attack (AOA) sweeps in steady-state flow conditions. The angle of the apparatus was measured by an inclinometer sensor with an accuracy of $\pm 0.1°$. Loads were measured using a six component strain gauge load cell. The load cell was capable of measuring loads up to 100 N normal force and 200 N axial force with a resolution of 0.05 N and 0.10 N respectively. The wind tunnel flow velocity was monitored by a pitot tube probe installed in the test section ahead of the model, connected to a pressure transducer with a resolution of 0.05 mmH_2O. Air temperature was monitored by a J-type thermocouple sensor mounted inside the test section. All channels were monitored simultaneously and recorded during testing.

The sequence of events for a given test was first to take a picture of the model at the set angle, with wind off. Next, the airspeed was set to the desired dynamic pressure, and when stable conditions were reached, images were taken of the deformed wing at 300 fps. At the same time, the system was recording the aerodynamic loads at 100 Hz, wind velocity at 2 Hz and model AOA at 2 Hz. This sequence was repeated at AOA of 3, 6, and 9 degrees at the selected nominal wind velocities of 12, 15, and 18 m/s, corresponding to Reynolds numbers between 60,000 and 90,000.
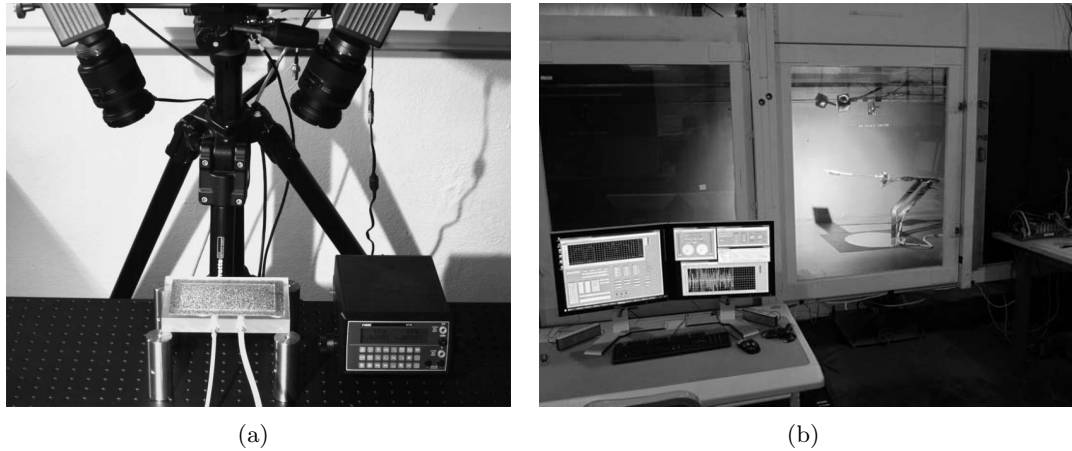
FIGURE 3.5: (a) Bench-top hydrostatic pressure experiment with stereo cameras for DIC, and HEISE pressure transducer. (b) Exterior view of the test section of the low speed closed loop, closed test section wind tunnel at Oregon State.

3.4.4 Numerical Fluid Model

To compute the fluid behavior and loads induced by the membrane wing, a three dimensional, steady-state, computational fluid dynamic (CFD) model was used. The test wing described above, was placed in a steady flow with a Re of 60,000-90,000 in air at 25 degrees Celsius and atmospheric pressure of 1 bar. This situation yields a Mach number of 0.037-0.052. This, being a sufficiently low value, allows an incompressible fluid assumption to be justifiably applied to the model. To reduce the computation time, a symmetric boundary condition was applied at the center-line of the wing model.
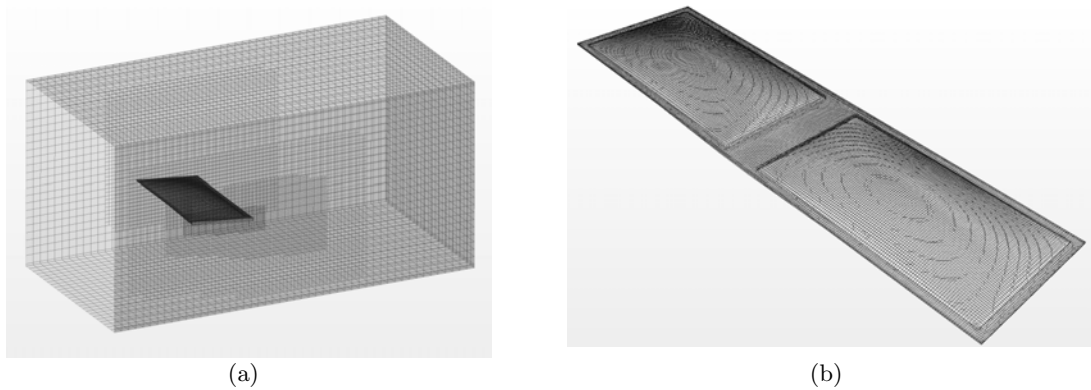
FIGURE 3.6: (a) Half span CFD simulation domain. (b) Meshed membrane wing analyzed in CFD. Membrane deformation was derived from time averaged DIC measurement from wind tunnel testing.

The half span simulation volume was sized with respect to the flow direction to be $5 \cdot c$ behind the wing, $2 \cdot c$ above, below and in front of the wing and $1 \cdot c$ to the outboard side of the wing. The volume was discretized into approximately 1.2 million hexahedral volume cells with an average cell width of ~ 0.1 mm in the near wake region, and growing cells up to ~ 10 mm near the simulation boundaries. Zero slip boundary conditions were used on the walls and wing surfaces, a constant velocity boundary condition was used on the inlet surface and a constant pressure boundary condition was used on the outlet surface. The simulation volume is illustrated in Fig. 3.6(a).

To create a three dimensional model of the deformed wing, DIC measurements were time averaged for each simulation case of velocity and AOA, and imported into a CAD model. This is the same process used in [98] and assumes the steady state, time averaged simulation results will compare adequately with time averaged dynamic results; as investigated by [103]. The results of this process can be seen in Fig. 3.6(b) for a membrane wing with 2% prestrain and 6 degrees AOA and free stream velocity of $13 m/s$ equating to $Re = 60000$. The Reynolds Averaged Navier Stokes (RANS) equations were solved for an incompressible flow in conjunction with the Spalart-Allmaras turbulence model. As shown by [104, 105], the Spalart-Allmaras turbulence model proves to perform

well in near wake regions such as flow around finite wings, while remaining relatively computationally inexpensive.

3.5. Results

The results for both hydrostatic pressure on a membrane and steady flow over a membrane wing in a wind tunnel are shown below. Comparisons of measured data and numerical models are used to compare the accuracy and behavior of the estimated parameters, ϵ_{ii}, $w(x,y)$ and $P(x,y)$. Aerodynamic coefficients for both lift (C_L), and pitching moment (C_m), are compared to measured wind tunnel loads.

3.5.1 Material Properties

Latex rubber sheets were used to construct the membrane wings for all tests. Due to the relatively low levels of deformation, resulting in $\epsilon_{ii} \leq 30\%$, a linear-elastic constitutive model was used to identify the elastic modulus and Poisson ratio using similar techniques as [101, 106]. To model the dynamics of the system, a constant material density was assumed as well as an assumption that the system behaved according to linear viscous dampening and Kelvin-Voigt viscoelastic damping effects. Further discussion and derivation of dampening parameters can be found in [8].

For all results, the following material parameters were used to model the rubber membrane; nominal pre-strain in x and y directions of 2%, linear elastic modulus of 1.6 MPa, Poisson ratio of 0.4, constant thickness of 0.14 mm, membrane density of 960 kg/m^3, viscous damping coefficient of 5 N s/m and Kelvin-Voigt viscoelastic damping coefficient of 0.0001 N s/m^2.

3.5.2 Strain Fields

For both test cases, DIC was used to measure full field strain and displacement of the deformed membrane. A five-by-five grid of virtual strain sensors, as seen in Fig. 3.7(b),

(a)

(b)

(c)
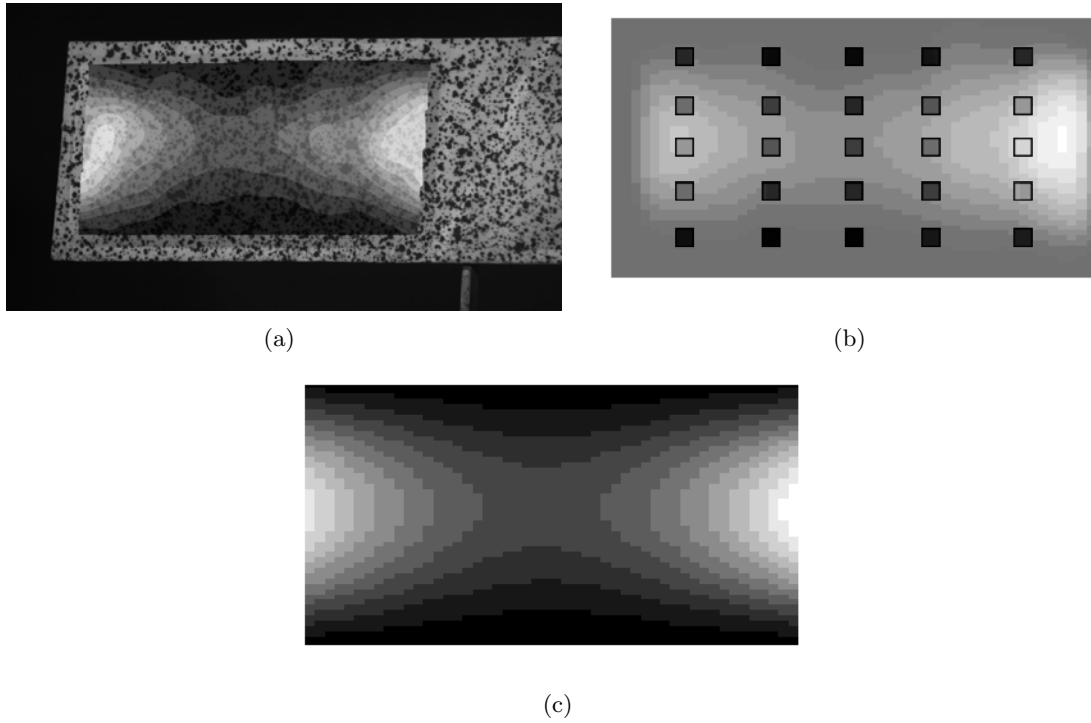
FIGURE 3.7: (a) DIC ϵ_{xx} strain measurements from wind tunnel test. (b) Virtual ϵ_{xx} strain sensors. (c) Estimated ϵ_{xx} strain field.

were distributed over the membrane to provide sensed strain as input into the estimation routine. Optimization of sensor placement and selection may provide improvements upon the results and is a topic for further study in future work. The estimation routine then produced estimated strain fields $\epsilon_{xx}(x, y)$ and $\epsilon_{yy}(x, y)$, out-of-plane displacement $w(x, y)$ and pressure distribution $P(x, y)$ using the methods previously described. An example of the measured strain fields, distributed virtual sensors, and the estimated strain field, can be as seen in Fig. 3.7 for a particular wind tunnel test.

The estimated strain fields compared well in terms of overall strain energy and overall strain magnitude. Errors in total strain energy were found to be less than 4% for all cases and local errors in strain magnitude less than 12% for all cases. Due to the nature of the selected basis, the estimated strain fields exhibit a stiffness to high frequency responses, which reduced the routine's ability to model spacial high frequency phenomena.

This characteristic of the basis function coupled with the least quares approach, inherently rejects an certian amount of sensor noise. A similar behavior is seen in the estimation of out-of-plane displacement.

3.5.3   Surface Deformation

Observing the estimation of out-of-plane displacement, $w(x, y)$, is a good midpoint evaluation for the capability of the approach since the estimation of deformation was derived from strain and since the pressure distribution utilized $w(x, y)$ and its derivatives in its formulation. The nine wind tunnel test cases in Fig. 3.8 show overlays of time averaged, normalized membrane deformation, at a y-position of 50% span from center-line of the wing. Averages were taken from the discrete time-variant estimation of the membrane deformation. Virtual strains were measured at 300 Hz for a duration of one second. The overlay images in Fig. 3.8 show the average and standard deviation for DIC measurements (gray line and light gray area), and the average and standard deviation for the estimated displacement, (black line and dark gray area).

Figure 3.8 shows a cross section of the membrane DIC and estimated out-of-plane deformations at 50% span. The gray line with the light gray area show the time aver-aged DIC displacement and standard deviation, while the black line and dark gray area represent the estimation. The standard deviations give a good indication of the wing's dynamic character for each of the testing conditions. Observing the displacements in Fig. 3.8, accuracy of the estimated average is quite favorable and is capable of estimating time averaged deformations for all test conditions. For U_∞ of 13 m/s and 15 m/s, the dynamic response of the estimate also compares well to the measured system; given that these cases were vibrating within a first and second modal behavior. At U_∞ of 18 m/s, large dynamic vibrations of the fourth order occur in the measured system. The estimate exhibits the same modal characteristics but does not accurately exhibit the same magnitudes of os-cillation. Since the purpose of this work was to derive global aerodynamic parameters,
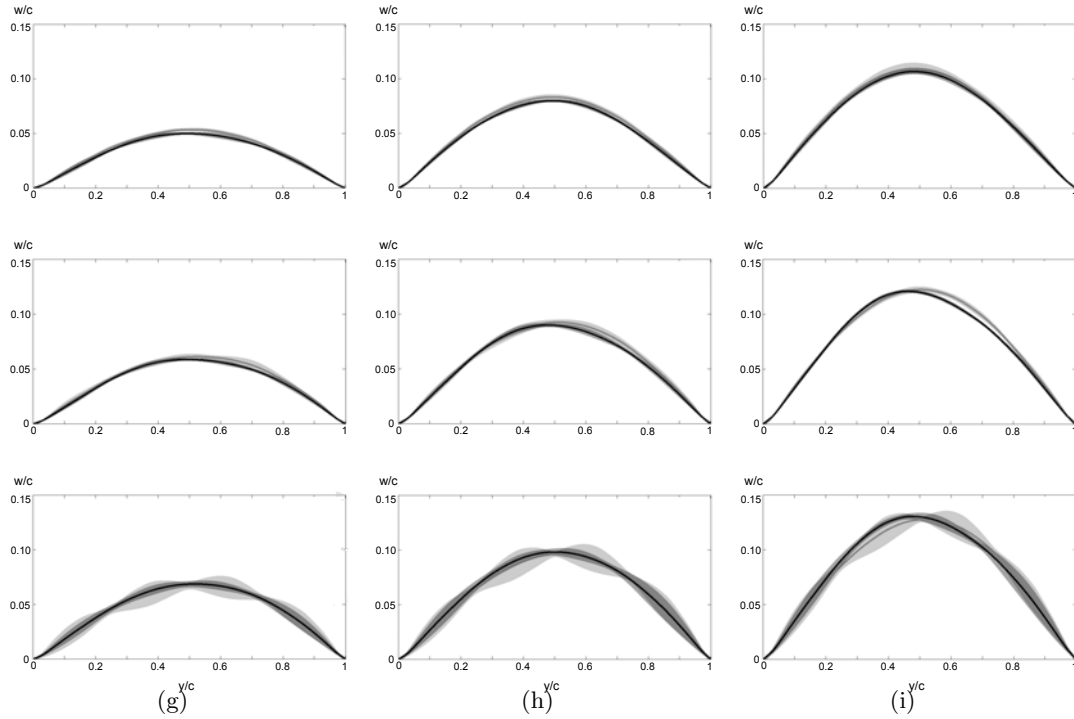
FIGURE 3.8: Normalized membrane displacement (w/c) on the vertical axis, vs normalized chordal position (y/c) on the horizontal axis. Cross sections take at the 50% span position from center-line of the wing, and where y/c = 1, represents the leading edge, and y/c = 0, represents the trailing edge. Time averaged DIC membrane displacement (gray line), with $\pm 1.5\sigma_{DIC}$ (light gray area) and time averaged estimated membrane displacement (black line), with $\pm 1.5\sigma_{EST}$ (dark gray area). (a) AOA 3°, U_∞ 13m/s, Re 60k. (b) AOA 6°, U_∞ 13m/s, Re 60k. (c) AOA 9°, U_∞ 13m/s, Re 60k. (d) AOA 3°, U_∞ 15m/s, Re 75k. (e) AOA 6°, U_∞ 15m/s, Re 75k. (f) AOA 9°, U_∞ 15m/s, Re 75k. (g) AOA 3°, U_∞ 18m/s, Re 90k. (h) AOA 6°, U_∞ 18m/s, Re 90k. (i) AOA 9°, U_∞ 18m/s, Re 90k.

the rejection of these higher frequency behaviors may prove advantageous but will require further investigation.

3.5.4 Pressure Distribution

With both estimated strain fields and estimated deformations, the calculation of pressure distribution could be made using the formulation given in Eq. 3.8. Estimated values of pressure distribution were evaluated against the ideal pressure distribution (hydrostatic) and numeric model of pressure distribution (wind tunnel). As well, pressure distributions were calculated from filtered full field DIC measurements. By comparing the estimate to the ideal or numeric distribution, the error produced from the estimation algorithm can be evaluated. By comparing the distribution calculated from DIC to the ideal/numeric, we see error effects from errors in the formulation assumptions. By comparing the DIC distribution to the estimated distribution, we will see the combination of error introduced due to the least squares routine, the choice of basis functions and sensor placement.

Contour plots of pressure distributions for a hydrostatic pressure test at 100 Pa are shown in Fig. 3.9. Figure 3.9(a) shows the ideal hydrostatic pressure applied to the membrane, in this case a magnitude of 100 Pa. Figure 3.9(b) shows the pressure distribution calculated from full field DIC measurements, and Fig. 3.9(c) shows the estimated pressure distribution from virtual strain sensors. Figure 3.10 shows the same data as Fig. 3.9, but presented as cross-wise sectional cuts of the pressure distributions as a function of normalized chord. Each figure represents a different span-wise position at $x/a = 0.25, 0.5, 0.75$, also represented by black lines in Fig. 3.9 for reference.

The hydrostatic pressure test shows reasonable results for the formulation to calculate steady state pressure distributions. The DIC distribution shows measurement noise variation, but has a mean value centered around the ideal distribution. Due to the choice of basis, the estimate exhibits a stiffness toward estimating a flat pressure distribution.

(a)

(b)

(c)
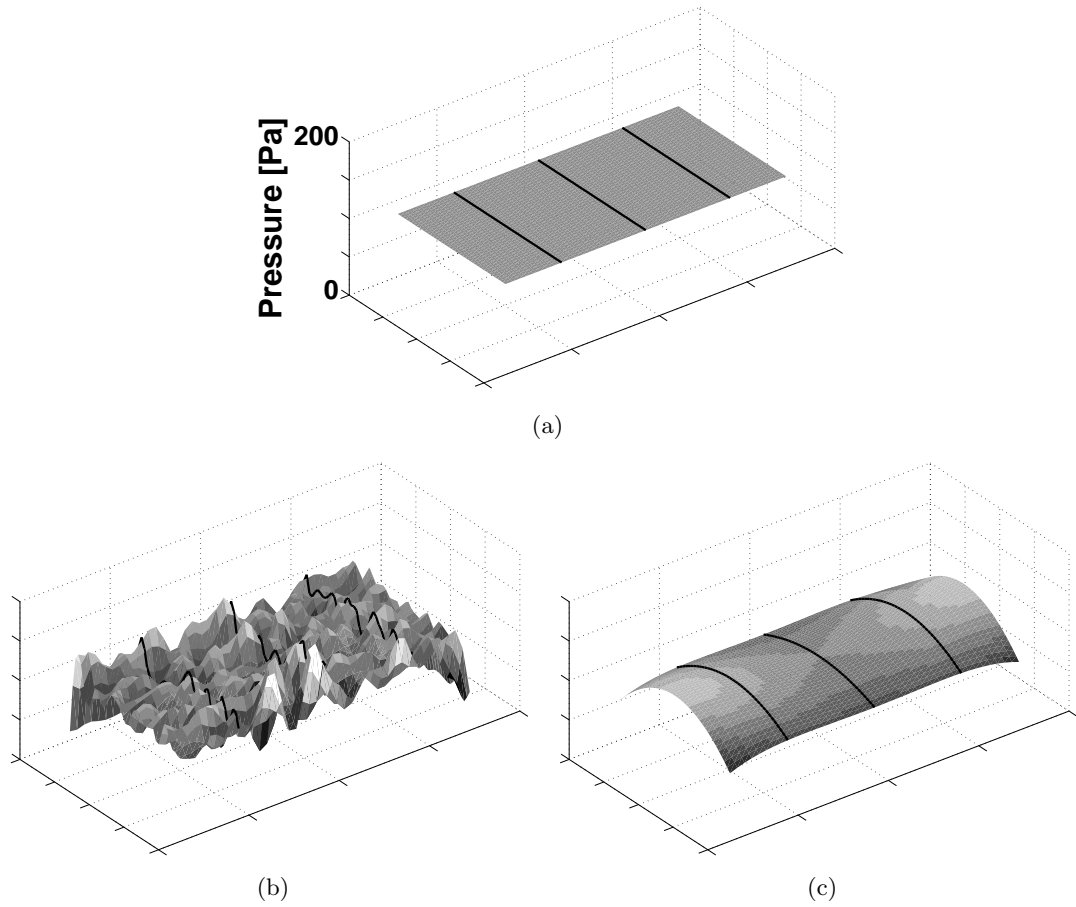
FIGURE 3.9: (a) Ideal hydrostatic pressure distribution for 100Pa. (b) Pressure distribution of hydrostatic test calculated directly from full field DIC measurements. (c) Pressure distribution of hydrostatic test estimated from virtual strain sensors. Black lines represent chord-size cross sectional cuts at span-wise positions of $x/a = 0.25, 0.5, 0.75$.

(a)

(b)

(c)
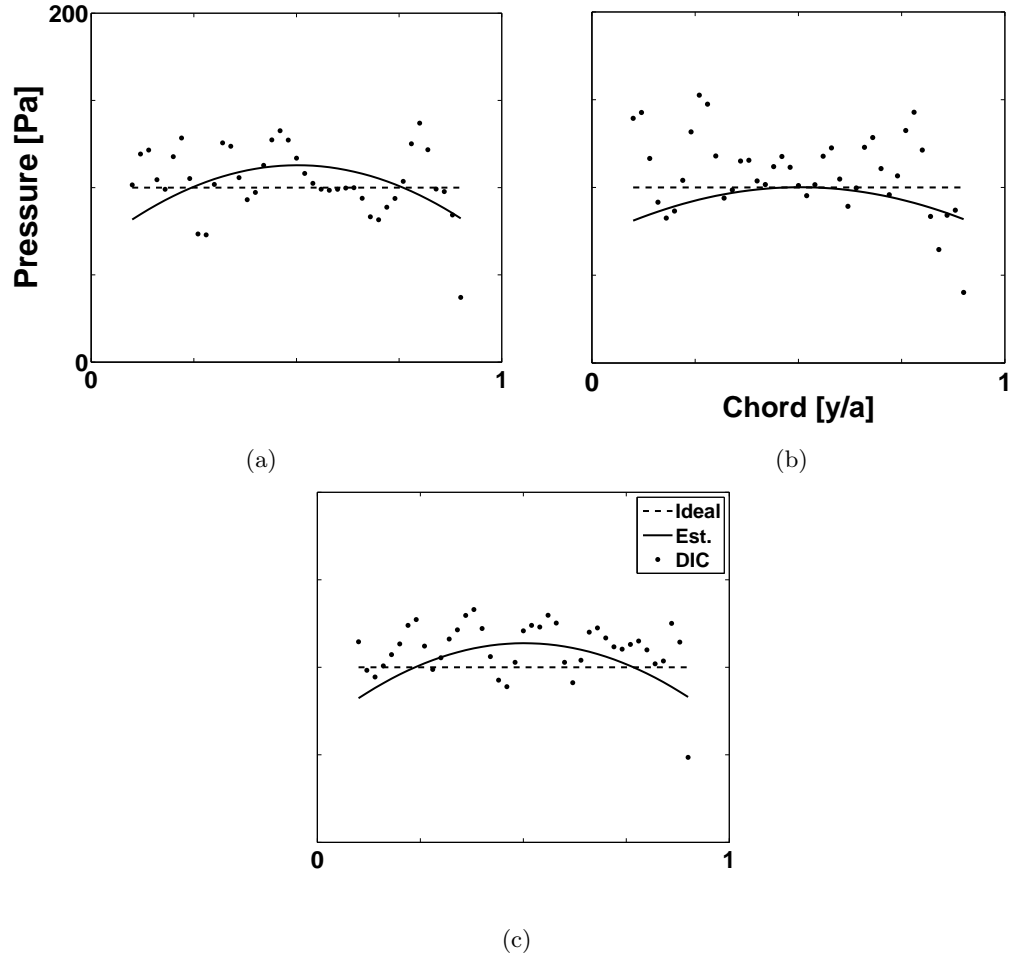
FIGURE 3.10: Normalized chordal cross section cuts at various span positions of hydro-static pressures; ideal pressure (dotted line), estimated pressure (solid line), DIC calculated pressure (points). Span positions (a) $x/a = 0.25$, (b) $x/a = 0.5$, (c) $x/a = 0.75$ are also shown for reference by black lines in Fig. 3.9.
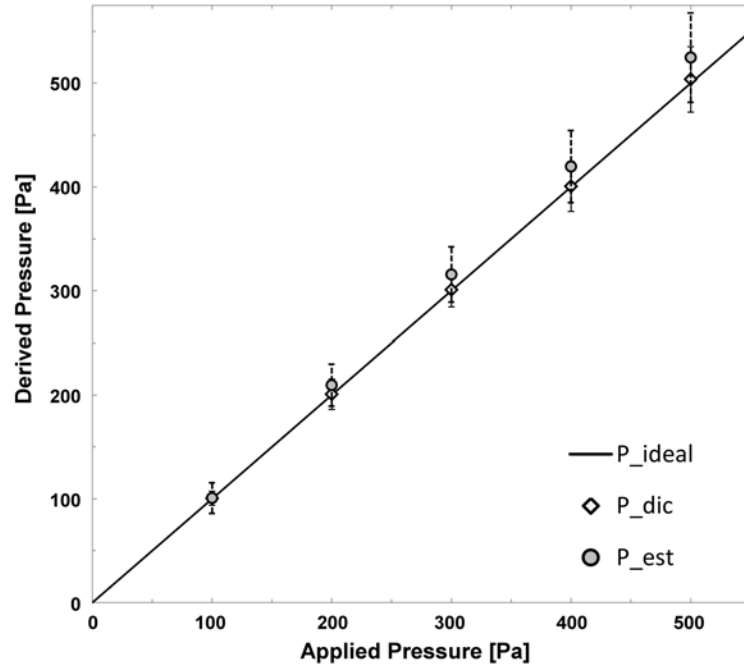
FIGURE 3.11: Pressure applied during the hydrostatic test plotted against the average pressure estimated, with value's 95% confidence interval.

Nevertheless, the average value for the estimated pressure distribution does correlate well as seen in the results in Fig. 3.11.

While the hydrostatic pressure case had a known applied load, the pressure applied to the membrane due to a steady fluid flow has a more complicated solution. For this reason the estimated pressure distributions were compared to a steady CFD simulation. To compare the time varying DIC measurements to the time invariant CFD, the DIC measurements were averaged over the 300 snapshots which were taken at 300 Hz. Likewise the virtual strain sensors were averaged to produce a single time averaged estimate for each test case in the wind tunnel. The pressure distributions for a particular wind tunnel test at 6° AOA and RE 60000 (12 m/s) are shown in Fig. 3.12. Figure 3.12(a) shows the total pressure distribution derived from the steady CFD simulation, Fig. 3.12(b) shows the calculated pressure distribution from full field DIC measurements, and Fig. 3.12(c) shows the estimated pressure distribution from virtual strain sensors. Figure 3.13 shows

(a)

(b)

(c)
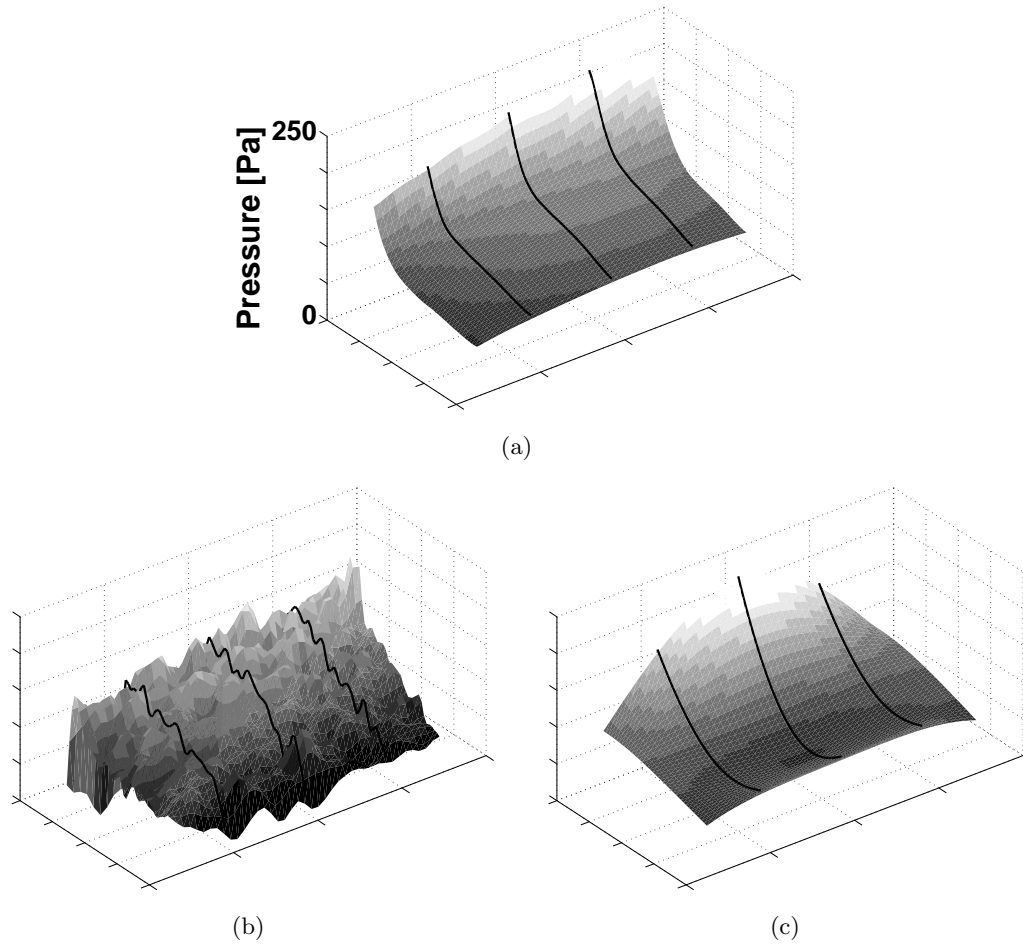
FIGURE 3.12: (a) Pressure distribution from steady CFD simulation, for wind tunnel test at 6° AOA, Re 60k. (b) Pressure distribution from time averaged wind tunnel test data at 6° AOA & Re 60k, calculated directly from full field DIC measurements. (c) Pressure distribution of wind tunnel test at 6° AOA & Re 60k, estimated from virtual strain sensors. Black lines represent chord-size cross sectional cuts at span-wise positions of $x/a = 0.25, 0.5, 0.75$.

the same data as Fig. 3.12, but presented as cross-wise sectional cuts of the pressure distributions as a function of normalized chord. Each figure represents a different span-wise position at $x/a = 0.25, 0.5, 0.75$, also represented by black lines in Fig. 3.12 for reference.

Observing the pressure distributions shown in Fig. 3.12, the CFD, calculated DIC and estimated pressure distributions correspond well to one another in both shape and magnitude. Again, variance is present in the DIC pressure due to differentiation of noise
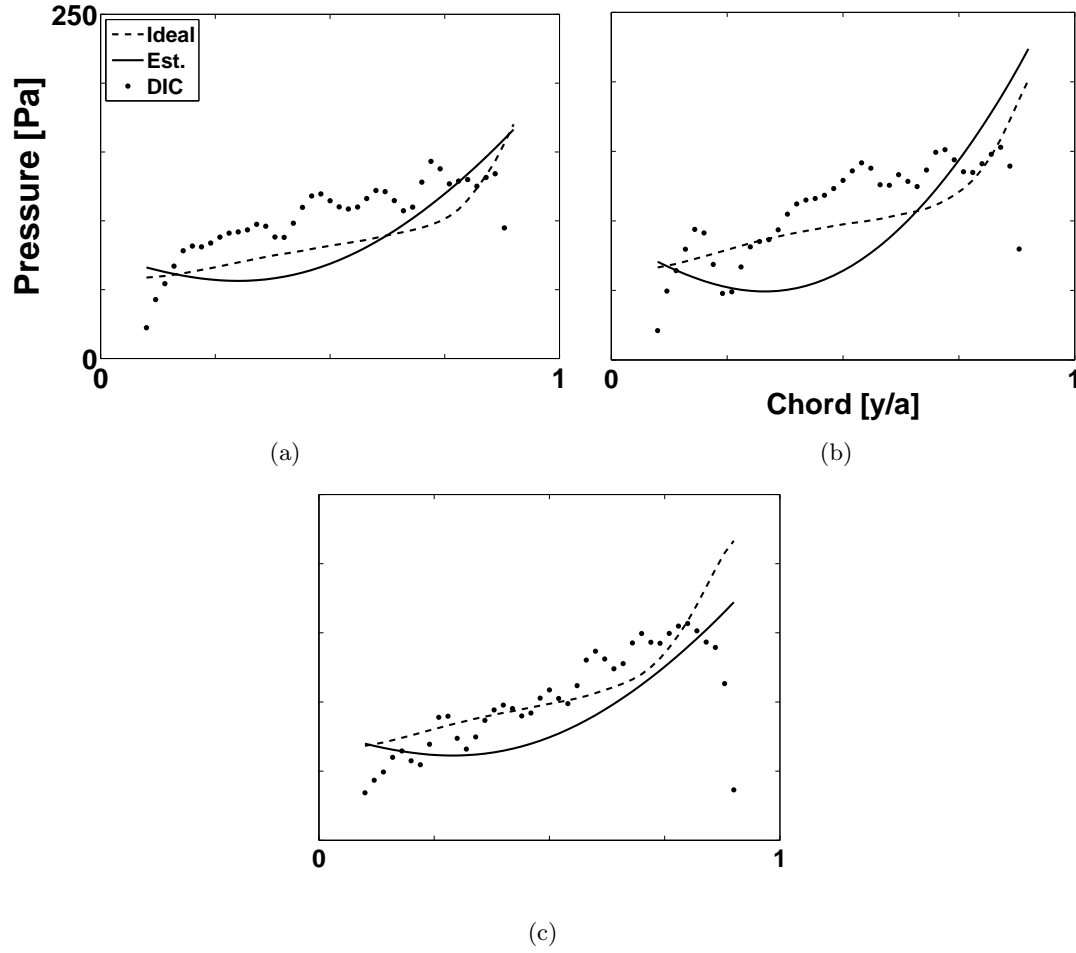
FIGURE 3.13: Normalized chordal cross section cuts of pressures at various span positions from wind tunnel test data at 6° AOA & **Re** 60k; CFD pressure (dotted line), estimated pressure (solid line), DIC calculated pressure (points). Span positions (a) $x/a = 0.25$, (b) $x/a = 0.5$, (c) $x/a = 0.75$ are also shown for reference by black lines in Fig. 3.12.

inherent in the DIC technique. Nevertheless, the results give confidence that the calculations previously presented were capable of adequately representing the physics of the system. Comparing the estimated pressure to the CFD and DIC pressure, it is again apparent that the overall shape diverges from the CFD and DIC estimates. It is assumed that the choice of basis or the least squares solution are causing the estimated solution to diverge from the actual solution. Nevertheless, the estimated pressure distributions do a fair job of representing the behaviors in both the time averaged cases as well as the time variant cases. Average residual error in the estimated pressure distribution as compared to the DIC pressure distribution were $\leq 10\%$ for all test scenarios.

3.5.5 Aerodynamic Loads

The ultimate objective of this work was to identify aerodynamic parameters from strain sensors which would be potentially useful for flight control. Both lift and pitching moment are critical loads in influencing the dynamics of an aircraft. To derive these values, the pressure distribution was integrated over the domain of the membrane to produce a resultant load. With the total resultant force applied to the wing and knowledge of the wing geometry, angle of attack, and flow velocity, the coefficient of lift can be calculated. The center of pressure in the y (chord-wise) direction was found, allowing the pitching moment about the 25% chord position (backward from leading edge) to be calculated.

For all wind tunnel test conditions, coefficients of lift and pitching moment about $0.25 \cdot c$ were measured for the actual wing via a six degree of freedom load cell and also estimated via virtual strain sensors. Time varying data from the load cell and estimation routine were averaged to identify a measurement of the steady state coefficient of lift and pitching moment for a given angle of attack. Figure 3.14(a) shows the coefficient of lift as a function of angle of attack for a single test condition at a Re of 60000. The theoretical function of lift within the linear, pre-stall regime, of $C_L(\alpha) = 2\pi \cdot \alpha + C_{L_{\alpha=0}}$, is included for reference as a dotted line. In addition, the lift measured due to a rigid plate substituted

for the flexible membrane is also shown for reference. Figure 3.14(b) shows the measured coefficient of lift and the estimated coefficient of lift as a function of angle of attack for all three flow conditions. Similar to the coefficient of lift, the coefficient of pitching moment was measured and estimated for three tested flow conditions as shown in Fig. 3.14(c). In Fig. 3.14, all error bars represent the 95% confidence interval of the time averaged measurement or estimate.

From Fig. 3.14(a) it is apparent to see the expected increase in lift coefficient of the membrane wing with respect to the rigid flat plate for the same Reynolds number. Figure 3.14(b) illustrates the increase of lift with Reynolds number due to the increase of the membrane camber, inflated by the dynamic pressure. Note, the "rigid" wing was constructed by replacing the membrane with a plate of aluminum. Given the non symmetric construction of the frame and the plate, a camber effect is created, resulting in on zero lift at zero AOA. It can be seen that the estimation deviates from test data with increasing angle of attack. A possible reason for this could come from the approach considering only the normal component of load and neglecting shear. Since shear loads become more prominent at higher angles of attack as flow separation is approached, this approach can not capture this load effects.

In general estimated lift and pitching moment are lower with respect to the experimental data and deviate with increasing angle of attack but all estimated values are within 12%. As shown in Fig. 3.14(c), the membrane wing exhibits static stability characteristics, about the aerodynamic center $(0.25 \cdot c)$ due to its increasing negative pitch angle with increasing AOA. Again, data are consistent between load cell measured values and estimates from the virtual strain sensors.

(a)

(b)

(c)
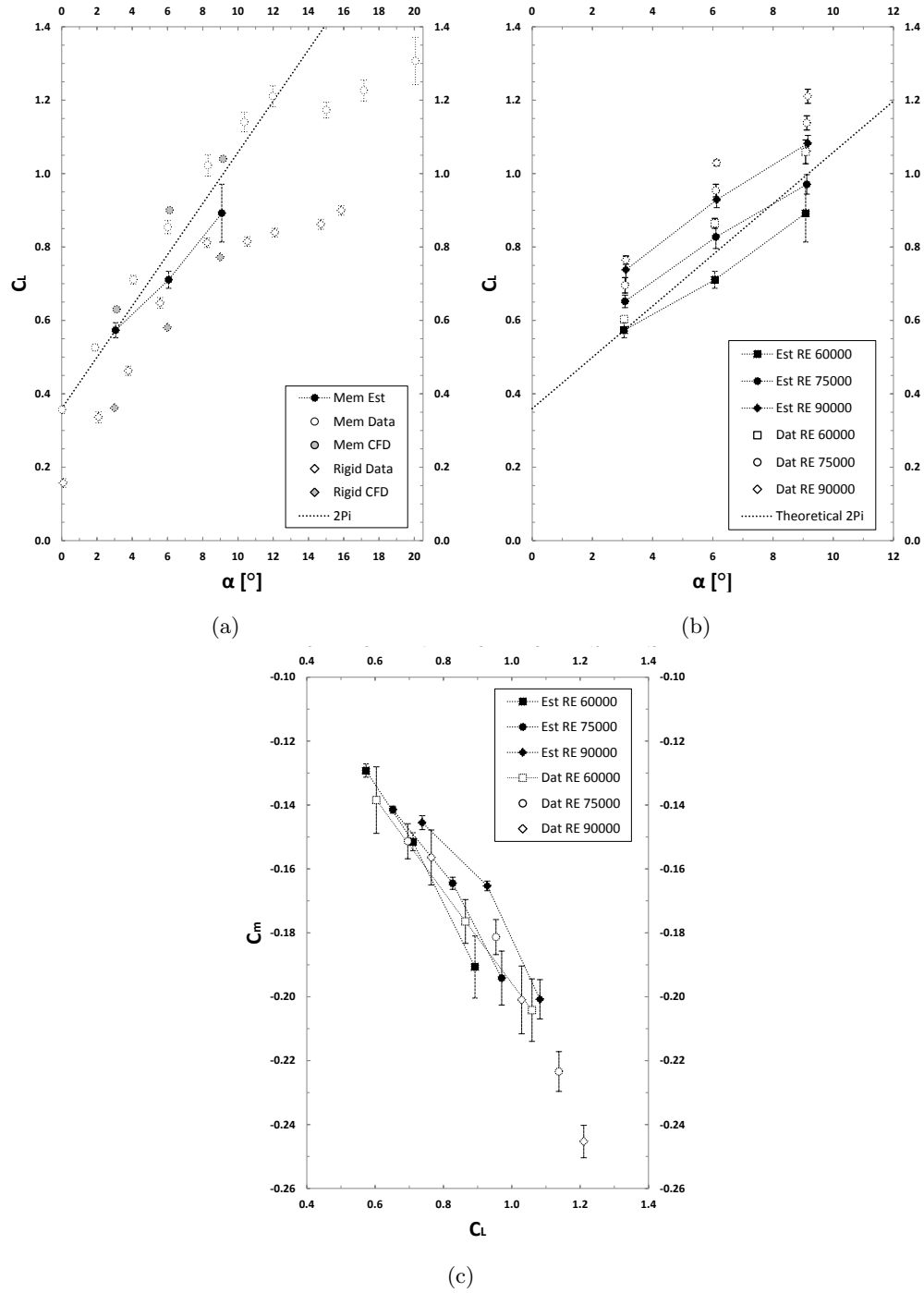
FIGURE 3.14: (a) Various coefficients of lift vs AOA for membrane wings in wind tunnel at a flow of *Re* 60000. (b) Measured and estimated coefficients of lift for membrane wing in wind tunnel at various flow speeds. (c) Measured and estimated coefficients of pitching moment for membrane wing in wind tunnel at various flow speeds. The theoretical line of $2 \cdot \Pi$ is included for reference. All error bars represent 95% confidence interval based on 300 time averaged samples for both DIC and estimated values. Lines between estimated values are for the reader's convenience and not to imply a trend.

3.6.   Conclusion

An approach was developed to estimate the aerodynamic loads generated on a membrane wing. Virtual strain sensors were defined over the domain of the membrane and used as inputs to an estimation routine. Using an analytic model of a membrane subject to a normally distributed load, input from virtual strain sensors was used to estimate the aerodynamic load on the membrane. Two tests were conducted to evaluate the accuracy of the estimation routine, as well as comparison to a steady numeric fluid model.

A hydrostatic pressure test was conducted in order compare a known input load, in this case a static pressure, to the estimated load. With a known input to the system, the output from the estimation routine could be directly evaluated for its accuracy. Results were favorable, the average hydrostatic pressure estimate was within 5% error to the actual applied hydrostatic load. Observing these results, the error of the estimate increases proportionally with the total magnitude of displacement, indicative that the estimation error scales proportionally to the input load for the range of loads applied.

Wind tunnel tests were conducted in which dynamic pressure distribution generated by the steady fluid flow over a membrane wing was estimated. From the estimated pressure distribution, coefficients of lift and pitching moment were calculated. These results were compared with an incompressible, time invariant RANS simulation and aerodynamic loads measured by a load cell connected to the wing model during wind tunnel testing. The estimated aerodynamic parameters show the potential for estimating aerodynamic lift and pitching moment from strain.

Although the loads studied in this work were induced by steady flow conditions, the formulation of the problem allows for adaption to time varying loads and it would seem feasible to estimate aerodynamic loads for dynamic flow scenarios. This work has provided an approach to estimating aerodynamic loads present on a flexible membrane wing subject to steady flow conditions. Further development of this work could provided higher

accuracy estimates, estimates of dynamic loads and real-time estimates of aerodynamic parameters.

Acknowledgments

Modeling effects of membrane tension on dynamic stall for a thin membrane wing

Trenton Carpenter, Roberto Albertani

Mattia Alioli, Marco Morandini, Pierangelo Masarati

4. MODELING EFFECTS OF MEMBRANE TENSION ON DYNAMIC STALL FOR A THIN MEMBRANE WING

4.1. Abstract

An approach for predicting time varying aerodynamic loads on a pitching membrane airfoil due to rotational pitching and steady airflow is presented. Membrane wings display unique aerodynamic characteristics due to their aero-elastic nature, which can provide performance improvements over their rigid airfoil counterpart. Extensive research has been conducted on the dynamics of flexible wings, but limited research exists on practical, computationally inexpensive, predictive models accounting for the dynamic behavior surrounding these wings. The model presented herein, utilizes potential flow theory for a thin cambered airfoil with finite span, combined with a linearized representation of the membrane physics to predict lift under static conditions. Quasi-steady rotational effects from convection lag and added mass effects are considered in a classic potential flow approach, modified for a membrane airfoil. A first order state space representation of the transient flow effects is used to model the dynamic separation delay of the pitching membrane airfoil. Theoretical models and experimental data for rectangular, 2:1 aspect ratio, rigid and flexible airfoils are presented. Comparisons of the static and dynamic lift predictions are made to wind tunnel data, and show favorable accuracy over a wide range of flow conditions ($Re = $ 50k-84k), reduced frequency ($k = $ 0, 0.05, 0.1), and membrane pre-tenstions ($\lambda_o = $ 1.02, 1.058, 1.085 and ∞).

4.2. Nomenclature

α Angle of attack [rad, °]

α_o Zero lift angle of attack $[rad, °]$
AR Wing aspect ratio
c Normalized chord length $[unity]$
ε Ozwald efficiency
K_p Potential flow lift constant
K_i Induced drag constant
κ Radius of curvature for a circular arc airfoil $[1/m]$
ϕ Segment angle of a circular arc airfoil $[rad, °]$
P Pressure, $[N]$
T Membrane tension, $[N/m]$
E Modulus of elasticity, $[Pa]$
ν Membrane Poisson ratio
h Membrane thickness $[m]$
ρ_m Membrane material density $[kg/m^3]$
ρ_∞ Free stream air density $[kg/m^3]$
Re Reynolds Number
U_∞ Free stream flow velocity $[m/s]$
k Reduced frequency
X_{st} Degree of trailing edge separation, static conditions $[unity]$
$X(t)$ Degree of trailing edge separation, dynamic conditions $[unity]$
$C_{L,dat}$ Coefficient of lift, wind tunnel data
$C_{L,p}$ Coefficient of lift, static attached potential flow
$C_{L,v}$ Coefficient of lift, due to leading edge separation
$C_{L,mem}$ Coefficient of lift, due to membrane displacement
$C_{L,att}$ Coefficient of lift, total static attached flow
$C_{L,sep}$ Coefficient of lift, static separated flow
$C_{L,st}$ Coefficient of lift, static conditions
$C_{L,qs}$ Coefficient of lift, quasi-steady dynamic conditions
$C_{L,dyn}$ Coefficient of lift, dynamic conditions

4.3. Introduction

Dynamic stall of pitching airfoils is a complex phenomena due to the delayed transient response of the fluid flow around the airfoil. Investigations into the physics of the phenomena have been the source of many studies for decades [107–111]. Due to the significant effects that pitching rates have on aerodynamic performance, many predictive models have been developed to estimate the aerodynamic effects caused by this phenom-

ena [112–115]. In this work, a predictive lift model is presented for the dynamic stall phenomena of a dynamically pitching, perimeter reinforced, membrane wing. This problem is unique compared to previous research in that the airfoil under consideration is highly flexible, introducing a new set of dynamic characteristics. A combined analytic and empirical model is presented which utilizes existing and novel formulations of the dynamic aero-elastic phenomena surrounding the problem.

4.4. Methods

The dynamic stall model presented in this work accounts for variation of lift due to a combination of leading edge separation, membrane deformation, quasi-steady and transient delayed lifting effects from dynamic pitching. This model utilizes a state-space representation of the time varying, delayed stall effects due to dynamic motion [114]. For static angles of attack (AOA), loads generated by leading edge separation were modeled using a leading edge suction analogy for thin airfoils [116]. The position of trailing edge separation, for static AOA, was estimated using wind tunnel test data to tune an empirical trailing edge separation model. The separation model linearly varies the predicted load between the analytic lift model for fully attached flow and fully separated flow. The static contribution of lift from membrane deformation was modeled by applying several assumptions to the physics of the membrane, and applying the idealized deformations to potential flow theory. The scope of this work is to model lift on the membrane wing, although other load parameters could be modeled using similar methods.

4.4.1 Static Lift Model

This approach employs a static lifting curve as the "backbone" of the dynamic stall prediction. This characteristic lift curve is generated by first defining the lift characteristics for fully attached and fully separated flow, under static AOA conditions. Transition

between these two curves due to stall, is determined using wind tunnel test data. First, lift for fully attached and fully separated flow conditions must be defined.

Potential Flow

Given the virtually zero thickness of the wings in the present study[2], the moderately low Reynolds number flow conditions (Re $50 - 84k$), and low Mach numbers ($M = 0.018 - 0.029$), incompressible, inviscid, potential flow theory for thin airfoils is used to define the lift model for static AOA. Given a camber line of an arbitrary wing, on which a vortex sheet singularity is applied, and flow tangency is enforced, along with the Kutta condition at the trailing edge, the lift for a finite length wing can be written as,

$$C_{L,p} = K_p(\alpha + \alpha_o) \tag{4.1}$$

where α is the angle of attack (AOA), α_o is the AOA at zero lift ($C_{L,p} = 0$), and K_p is the potential flow constant defined in this work as,

$$K_p = \frac{2\pi}{\left(1 + \frac{2\pi}{\pi \varepsilon AR}\right)} \tag{4.2}$$

where ε is the Ozwald efficiency factor, and AR is the aspect ratio of the given wing planform.

Leading Edge Separation

Leading edge separation is a common occurrence on thin airfoils [117]. Given low AOA and adequately energetic flow conditions, flow on the low pressure side of the wing will reattach to the surface a short distance beyond the leading edge. The contribution of lift due to this separation can be predicted using Polhamus' leading edge suction analogy

---

[2]The membrane section of the wing has a thickness to chord ratio of 1:1000, ($c/h = 0.14mm/0.00014mm$), while the leading and trailing edges have a thickness to chord ratio of 1:65, ($c/h_{frame} = 0.14mm/(0.00014mm + 2 \cdot 1mm)$) from the metal perimeter frame.

[116]. This approach assumes the normal force produced on the wing by the leading edge vortex is equally balanced by the strength of the potential flow which constrains and holds the vortex to the surface of the wing. Assuming flow reattaches past the leading edge separation bubble, the component of lift due to leading edge separation for a non swept wing[3] can be written as,

$$C_{L,v} = (K_p - K_p^2 K_i) \cos(\alpha) \sin^2(\alpha) \tag{4.3}$$

where K_i is the induced drag constant defined for this work as $K_i = 1/\pi \varepsilon AR$.

Membrane Displacement

Modeling a membrane sheet subject to induced flow is a complex, coupled aero-elastic, dynamic problem. Due to the nature of this problem, simple close-form solutions are quite often not possible for these systems. Typical solution strategies utilize coupled structural and fluid solvers [52, 118], or inverse based approaches [96, 119], which provid *a posteriori* solutions to membrane displacements and loads. Conversely, if several simplifying assumptions are made about the physics of the membrane and the loads applied to it, a prediction of the membrane displacement and the resulting loads can be made *a priori*, as demonstrated by [6]. In this case, it is assumed that the membrane displacement can be modeled as a circular arc, and the load applied to the membrane is an evenly distributed pressure. In this case, the membrane is modeled as, massless, linear elastic, constrained along all edges, experiencing constant internal tension due to deformation, and subjected to constant positive pre-tension in its undeformed state. Provided these assumptions, the state of membrane deformation can be equated to an aero-elastic coefficient,

$$Ae = \frac{Eh}{\frac{1}{2}\rho U_\infty^2 c} = \frac{Eh}{qc} \tag{4.4}$$

---

[3]For this work the wing has a rectangular planform, thus the sweep angle is zero, $(\Lambda = 0^\circ)$.

where E is the linear modulus of elasticity of the membrane, h is the membrane thickness, ρ is the density of the fluid, U_∞ is the free stream velocity of the fluid, c is the wing chord, and q is the dynamic pressure. If the membrane out-of-plane displacement is assumed to fit the form of a circular arc, and the value of maximum displacement normalized to the chord length is defined as z, then it can be shown that,

$$\frac{C_L}{Ae} = f(\lambda_o, z) \tag{4.5}$$

where f is a function to be determined, λ_o is defined as the stretch ratio due to pretension, i.e. $\lambda = (1 + \epsilon)$, where ϵ is the strain of the membrane due to deformation and/or pretension. Equation 4.5 shows that if the AOA, flow conditions, and membrane properties are known, then the amount of membrane displacement can be determined. Using the geometric properties of a circular arc segment and the potential flow solutions to lift for a circular arc airfoil, a relationship between the AOA and membrane displacement z, can be found for a finite aspect ratio rubber membrane wing as,

$$\alpha + \sin^{-1}\left(2\eta\frac{Ae}{K_p}(\kappa - \lambda_o\phi)\right) - \frac{\phi}{4} = 0 \tag{4.6}$$

where ϕ and κ are the arc segment angle and radius of curvature respectively, as seen in Fig. 4.1, and $\eta = (1 + 1/AR)$, accounts for the difference in span vs chord curvature. For a chord length, c, equal to unity, ϕ and κ can be defined in terms of normalized max out-of-plane displacement, $z = z_{max}/c$, as,

$$\phi = 2\sin^{-1}\left(\frac{\kappa}{2}\right) \tag{4.7}$$

$$\kappa = \frac{8z}{4z^2 + 1}. \tag{4.8}$$

Given the implicit nature of Eqn. 4.6, any number of numeric solving tools can be used to determine z given α, material properties and flow conditions.
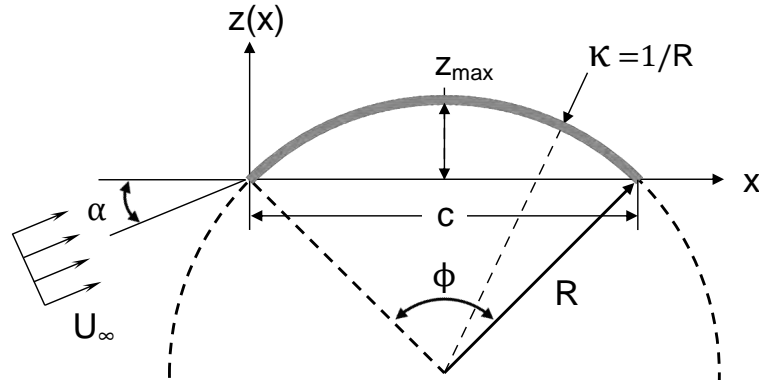
FIGURE 4.1: Geometry of a circular arc segment used to generalize the chordal shape of a displaced membrane airfoil.

Using potential flow theory, the coefficient of lift for a thin two dimensional circular arc airfoil is defined as,

$$C_{L,arc} = 2\pi \sin(\alpha + \frac{\phi}{4}).$$ (4.9)

Generalizing this solution to a finite span wing, the contribution of lift due to the cambering effect of the membrane can be defined as,

$$C_{L,mem} = K_p \left(\sin(\alpha + \frac{\phi}{4}) - \sin(\alpha) \right).$$ (4.10)

With this result, for a given AOA, Eqn. 4.6 can be used to find the value of camber z. Substituting z into Eqn. 4.8, κ into Eqn. 4.7, and finally ϕ into Eqn. 4.10, the value of lift due to membrane displacement for a finite aspect ratio wing is found.

Membrane Stability

A phenomenon unique to membrane airfoils is the potential for camber instability at zero AOA. Sufficiently compliant membranes subject sufficiently high dynamic pressure will exhibit non zero camber at zero AOA, while sufficiently stiff membranes subject to lower dynamic pressure will have zero camber at zero AOA. Consequently, if the membrane is stable at zero AOA, there will be zero lift at zero AOA, and conversely, if the membrane
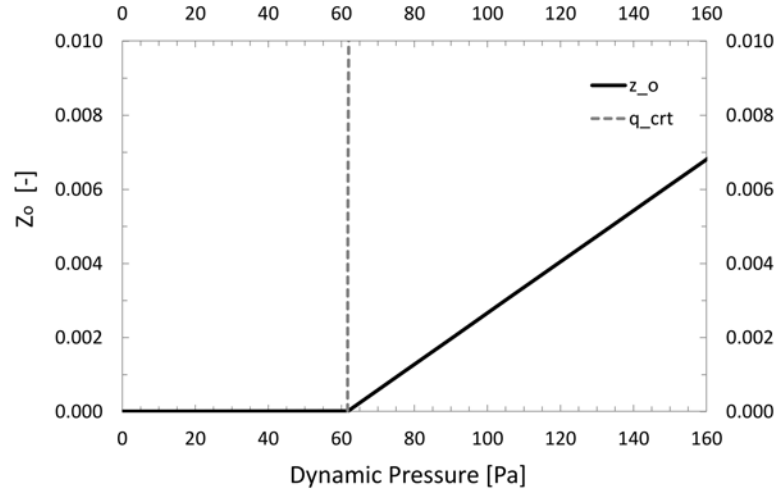
FIGURE 4.2: Value of camber at zero AOA for increasing dynamic pressure. Region left of the grey dashed line represents stable membrane conditions, and the region right of the dashed line represents unstable conditions.

is unstable, there will be a non-zero lift at zero AOA. As shown by Waldman [6], there exists a stability criteria that can be equated to Ae. Extending Waldman's solution of the Young-Laplace equation to a finite aspect ratio wing, we find that a critical dynamic pressure exists, above which, membrane cambering will occur at zero AOA. This critical dynamic pressure is defined as,

$$q_{crt} = \lim_{z \to 0} \left[4\frac{\eta}{\varepsilon} Eh \left(\lambda_o \frac{\phi}{\kappa} - 1 \right) \right]. \tag{4.11}$$

Under the scenario where the membrane is stable, i.e. operational dynamic pressure, q, is less than q_{crt}, then $z_o = 0$ and no modification of the lift model is required. But if $q > q_{crt}$, the membrane is unstable, and $z_o \neq 0$. This effect is illustrated in Fig. 4.2, where the black line represents the maximum normalized membrane displacement at zero AOA, and the dashed grey line separates the region of stability and instability. In the case of unstable conditions, a contribution of lift must be added to account for the non zero camber. It is assumed that additional flow energy beyond q_{crt} contributes to forcing the membrane to displace. Under this condition, an equilibrium can be found between

the excess flow energy $(q - q_{crt} > 0)$ and the tension in the membrane. Assuming the displacement of the membrane follows a circular arc in both chord and span, a relationship between excess flow energy and membrane tension at zero AOA for a finite aspect ratio can be defined as,

$$\frac{8}{\pi c^2} \eta E h (\lambda_o \phi - \kappa) - q = 0, \quad \text{for } q > q_{crt}$$

$$z_o = 0, \qquad\qquad\qquad \text{otherwise.}$$

$$(4.12)$$

An implicit formulation of z given a dynamic pressure q was obtained. The same numeric procedure used on Eqn. 4.6 can be applied to Eqn. 4.12, to solve for z_o given membrane pretension, modulus, thickness, wing aspect ratio, $\alpha = 0$, and dynamic pressure. Using z_o an estimate of camber at zero AOA, the lift due to this camber can be found using Eqn. 4.10 evaluating $\alpha = 0$. If this coefficient of lift is defined as, C_{Lo}, then a zero lift angle offset, α_o, can be determined as,

$$\alpha_o = \begin{cases} \sin^{-1}\left(\frac{C_{Lo}}{K_p}\right), & q > q_{crt} \\ 0, & \text{otherwise.} \end{cases}$$

$$(4.13)$$

Finally, substituting Eqn. 4.13 into Eqn. 4.1, the lift due to potential flow, the contribution of lift due to unstable membrane displacement at zero AOA is accounted for. It should be noted that this unstable membrane displacement at zero AOA can bifurcate about zero camber, allowing for equal displacement in both positive and negative directions. This model assumes the direction of unstable displacement to be in the direction of positive lift, thus generating a positive lift contribution. This model does not consider the bifurcating effect which would occur if the wing was to sweep from a positive AOA to a large negative AOA.

Attached Flow Model

At this point, a complete model of C_L for static AOA and attached flow can be assembled. If we considering the main contributions of lift on a thin membrane wing to be

from potential flow, leading edge separation, and cambering due to membrane displacement, then the principle of superposition can be used to combine Eqn. 4.1, 4.3, and 4.10, to represent the total lift under attached flow conditions as,

$$C_{L,att} = C_{L,p} + C_{L,v} + C_{L,mem}. \tag{4.14}$$

Each lift contribution and the complete attached lift model is shown in Fig. 4.3. Fully "attached" flow is considered flow which reattaches beyond the leading edge separation bubble and remains attached until the trailing edge. Under the range of AOA where fully attached flow conditions apply, Eqn. 4.14 represents the coefficient of lift that would be expected for a perimeter reinforced, self cambering, thin membrane wing, with a finite aspect ratio, experiencing leading edge separation.
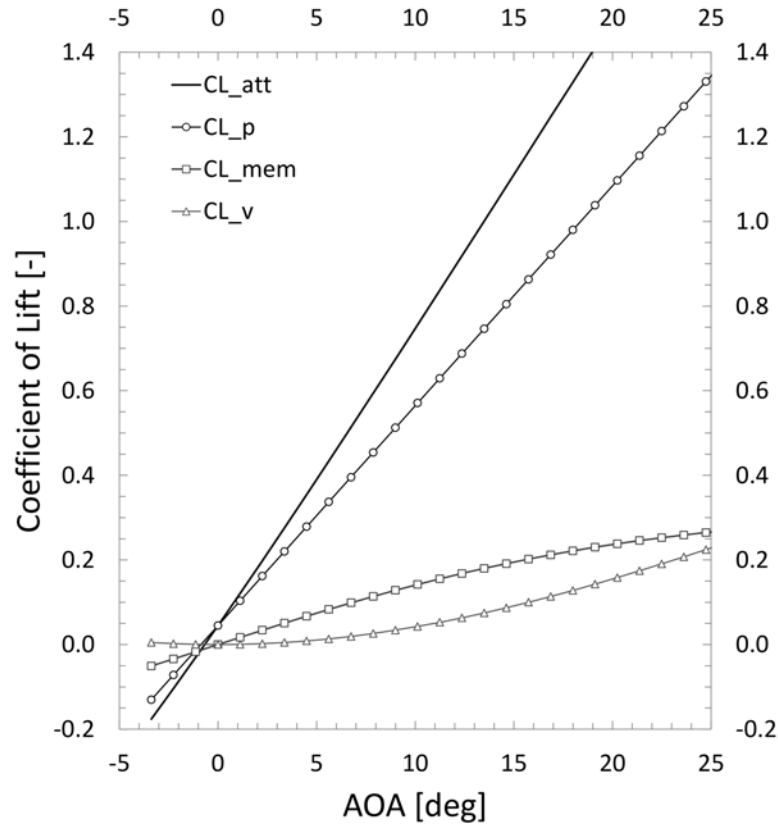
FIGURE 4.3: Coefficient of lift vs. AOA, depicting contributions to the attached flow lift model due to, potential flow, leading edge separation, membrane cambering with AOA, and membrane cambering for unstable conditions at $\alpha = 0$ *(Image depicts behavior for an unstable membrane condition at zero AOA. Conditions: $E = 1.14\ MPa$, $h = 0.14\ mm$, $c = 0.14\ m$, $\lambda_o = 1.02$, $U_\infty = 8\ m/s$, $AR = 2$, $\varepsilon = 0.9$).*

Separated Flow Model

To model the lift coefficient of a fully separated airfoil, we consider test data for angles of attach beyond complete stall. It is generally accepted that the magnitude of lift becomes reasonably independent of airfoil shape after full separation [114, 120]. Wind tunnel data[4], [122], are applied to an empirical two dimensional lift model for fully separated

---

[4]Observing this test data, for all airfoils and flow conditions there appears to be a positive shift in lift coefficient of ~ 0.05, likely due to some asymmetry existing in the experimental setup. This provides a sinusoidal peak amplitude of ~ 1.05 rather than 1.1 as published in other works [120, 121].

flow as,

$$C_{L,sep2D} = \frac{\pi}{3}\sin(2\alpha). \tag{4.15}$$

Extending this model to a finite aspect ratio wing, a lift model for three dimensional flow is defined as,

$$C_{L,sep} = \frac{\pi\sin(2\alpha)}{3 + \frac{1}{\varepsilon AR}}. \tag{4.16}$$

With the attached flow model from Eqn. 4.14 and the separated flow model from Eqn. 4.16, the transition between these two states due to the development of stall must be defined.

4.4.2 Degree of Trailing Edge Separation

For this approach, it is assumed that the phenomena of stall occurs via a point of flow detachment on the suction side of the airfoil, starting at the trailing edge and progressing upstream toward the leading edge. Consider the degree of trailing edge separation as $0 \le X_{st} \le 1$. By definition, a value of $X_{st} = 1$ represents a condition of fully attached flow, and a value of $X_{st} = 0$ represents fully separated flow. If we consider the trend of X_{st} with respect to increasing static AOA, it is expected that X_{st} will remain at a value of 1 for low AOA. As stall occurs, it will transition smoothly yet rapidly toward zero and will remain zero for large AOA. The degree of separation model used in this study is an extrapolation of the low pass Butterworth gain function, define as,

$$X_{st} = \frac{1}{\left[1 + \left[\left(\frac{\alpha}{\alpha^*}\right)^2\right]^{n_1}\right]^{n_2}} \tag{4.17}$$

where α^*, n_1, and n_2 are factors which need to be identified for given wing configuration and flow condition. Using this definition of trailing edge separation, a complete static lift model which transitions from fully attached to fully separated flow conditions can be defined as,

$$C_{L,st} = C_{L,att}X_{st} + C_{L,sep}(1 - X_{st}). \tag{4.18}$$

In order to determine α^*, n_1, and n_2, wind tunnel test data is used to construct a least squares regression to minimize the error between lift data and the static AOA model, $C_{L,st}$. An example of the results from fitting $C_{L,st}$ to wind tunnel data for a particular membrane wing and flow velocity, is shown in Fig. 4.4, along with $C_{L,att}$, $C_{L,sep}$, and X_{st}.
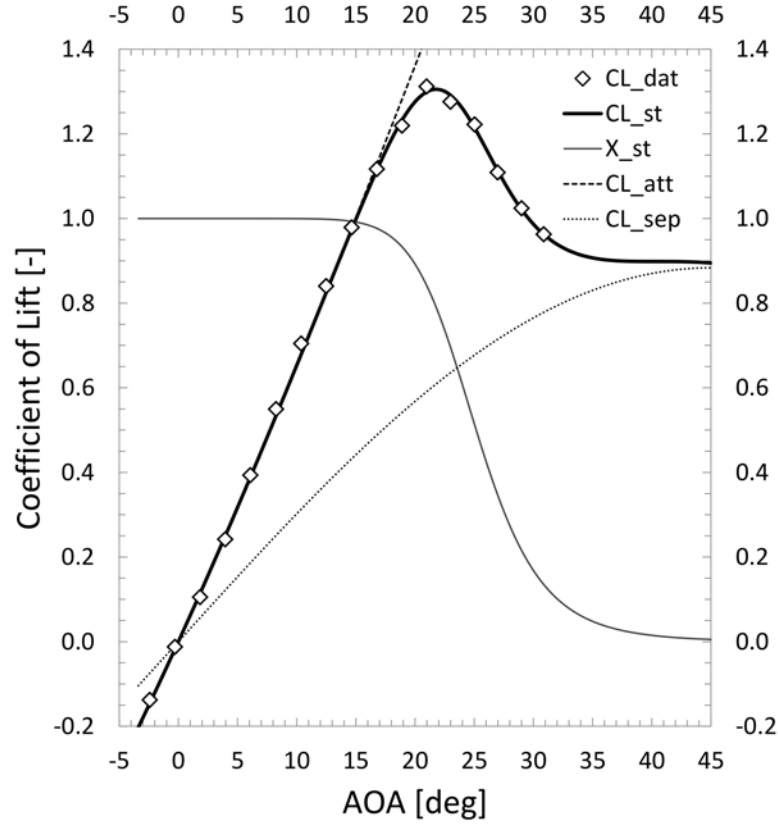
FIGURE 4.4: Model of coefficient of lift for static AOA fit to wind tunnel test data for a membrane wing. *Conditions:* $E = 1.14 \; MPa$, $h = 0.14 \; mm$, $c = 0.14 \; m$, $\lambda_o = 1.058$, $U_\infty = 10 \; m/s$, $AR = 2$, $\varepsilon = 0.9$.

The static lift curve $C_{L,st}$ represents the "backbone" of the dynamic stall model. As non zero pitching rates, $\dot{\alpha} \neq 0$, are introduced, actual lift behavior will begin to deviate from $C_{L,st}$ due to the introduction of quasi-steady and transient flow effects.
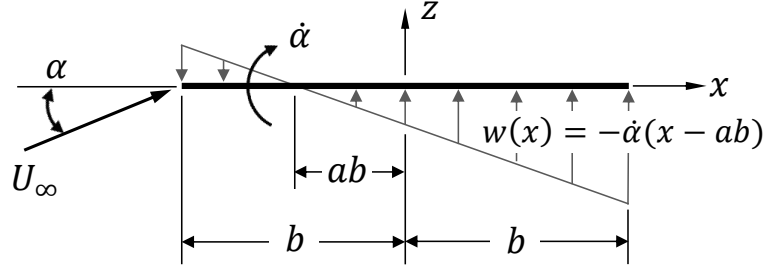
FIGURE 4.5: Velocity distribution normal to surface of a pitching airfoil rotating about the quarter chord position.

4.4.3 Dynamic Stall Model

Many forms of dynamic stall models exist for pitching airfoils. The majority of approaches can be categorized into three different varieties; physics based models accounting for time varying flow effects (Boddes-Leishman, $\varnothing$ye, Ris$\varnothing$), models which directly manipulate a load curve due to AOA and pitch rates (ONERA), and models using a modified AOA value for dynamic conditions (Boeing-Vertol) [115, 123]. In this work, the dynamic stall model used, is a time varying, physics based model [114]. Quasi-steady rotational effects, i.e., circulation changes and boundary convection lag, equate to instantaneous delayed lift and added mass loads. These effects are considered using a potential flow approach for a thin airfoil. Consider a thin airfoil pitching about a quarter chord axis, or position from mid chord $a = -1/2$, see Fig. 4.5. Applying thin airfoil theory, the following solutions can be obtained using the normal velocity distribution, $w(\theta)$, due to rotation about ab,

$$
\begin{aligned}
A_o &= \alpha - \frac{1}{\pi} \int_0^\pi \frac{w(\theta)}{U_\infty} d\theta \\
A_n &= \frac{2}{\pi} \int_0^\pi \frac{w(\theta)}{U_\infty} \cos(n\theta) d\theta
\end{aligned}
\tag{4.19}
$$

where $x = -\frac{c}{2} \cos\theta$ based on a coordinate system at mid-chord, and $w(x) = -\dot{\alpha}(x - a\frac{c}{2})$. Evaluating this solution about the quarter chord, an effective AOA can be defined which

accounts for quasi-steady rotational flow effects,

$$\alpha_{qs} = \alpha + \frac{c}{2U_\infty}\dot{\alpha}. \tag{4.20}$$

From this solution, it is evident that the quasi-steady rotational effects scale proportionally to $\frac{c}{2U_\infty}$. Substituting the effective AOA from Eqn. 4.20 into $C_{L,st}$ from Eqn. 4.18, a model which describes quasi-steady dynamic lift is obtained as follows,

$$C_{L,qs} = C_{L,att}(\alpha_{qs})X_{st}(\alpha_{qs}) + C_{L,sep}(\alpha_{qs})(1 - X_{st}(\alpha_{qs})) \tag{4.21}$$

For low AOA where trailing edge separation has not yet developed, $C_{L,qs}$ accounts for variations in load due to non zero pitch rates. As AOA increases into the stall regime, the separation point is delayed with respect to time in its progression along the airfoil. This transient, delayed separation effect, is accounted for using a first order differential equation which describes the relaxation behavior of the separation point.

$$\tau_1\dot{X}_d + X_d = X_{st}(\alpha - \tau_2\dot{\alpha}) \tag{4.22}$$

where τ_1 is a dynamic separation point relaxation time constant. Recall the observation from Eqn. 4.20, that $\dot{\alpha}$ scales proportionally to $\frac{c}{2U_\infty}$. Here we define a quasi-steady separation point time scaling constant, $\tau_2 = \tau_2^*\frac{c}{2U_\infty}$, where τ_2^* is a tuning parameter.

Assuming a known kinematic pitching motion of the airfoil about the quarter chord position, where $\hat{\alpha}_s$ and $\dot{\hat{\alpha}}_s$ are the known initial static AOA and pitch rate, Eqn. 4.22 can be solved for $X_d(t)$ using a numeric ordinary differential equation solver and an initial condition of $X_d(t)|_{t=0} = X_{st}(\hat{\alpha}_s - \tau_2\dot{\hat{\alpha}}_s)$. $X_d(t)$ represents the dynamic separation point of the cambered airfoil due to a time varying pitching motion. With quasi-steady separation effects and transient separation effects modeled, a complete dynamic stall model is defined
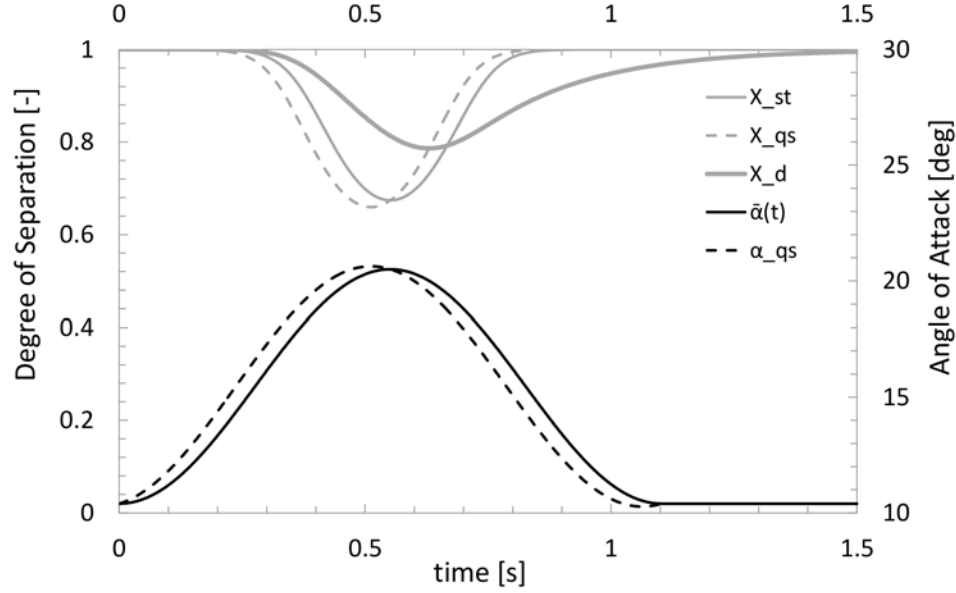
FIGURE 4.6: Comparison of separation behavior for a single sinusoidal pitching motion from $\alpha = 10$ to 20 degrees.

for a given pitching motion as,

$$C_{L,d} = C_{L,att}(\alpha_{qs})X_d(t) + C_{L,sep}(\alpha_{qs})(1 - X_d(t)) \tag{4.23}$$

To illustrate the mechanics of dynamic separation presented in this model, consider a thin airfoil, pitching about the quarter chord, where the airfoil undergoes a single oscillation of the kinematic motion defined as,

$$\hat{\alpha}(t) = \frac{1}{2}\hat{\alpha}_{amp}\sin(2\omega t - \frac{\pi}{2}) + \frac{1}{2}\hat{\alpha}_{amp} + \hat{\alpha}_s$$
$$\dot{\hat{\alpha}}(t) = \hat{\alpha}_{amp}\omega\cos(2\omega t - \frac{\pi}{2}) \tag{4.24}$$

where ω is the angular frequency, (also defined as $\omega = kU_\infty/c$, k is the reduced frequency), $\hat{\alpha}_s$ is the motion start angle, and $\hat{\alpha}_{amp}$ is the peak-to-peak amplitude of oscillation. Figure 4.6 show the degree of trailing edge separation for static AOA, X_{st}, for quasi-steady separation, X_{qs}, and transient dynamic separation, X_d, for a single pitching motion from 10 to 20 degrees AOA. The kinematic motion profile and the quasi-steady AOA are also

included on the figure for reference. The static separation follows the kinematic motion proportionally as expected. Four characteristics can be observed from Fig. 4.6: 1) the effective quasi-steady AOA increases in angle compared to kinematic AOA for positive pitch rates, 2) equals the kinematic AOA where $\dot{\hat{\alpha}}(t) = 0$, 3) is reduced in value for negative pitch rates, and 4) ultimately converges when the motion stops. As expected, the quasi-steady separation follows the effective quasi-steady AOA proportionally. Dynamic separation displays a time varying lag behavior, and exhibits a time delay to ultimately converge to static angle values of separation, as expected for time varying separation.

4.5.   Experimental Setup

A variety of tests were conducted in a low speed wind tunnel to produce measurements of lift and membrane displacement for a wing pitching with static and dynamic AOA. These measurements were used as a basis of comparison to the methodology previously discussed. Tests were conducted on wing models with varying membrane pretension, subject to various flow conditions and pitching rates. Variables consider in the test were, membrane pretension (λ), flow velocity (U_∞), pitch rate ($\dot{\alpha}$), reduced frequency (k), and starting pitch angle (α_{st}). Pitching amplitude (α_{amp}) was held constant at $10°$ peak-to-peak, and pitching axis was held constant at 25% chord position throughout the tests.

4.5.1   Test Article

The test article used in the wind tunnel was a 2:1 aspect ratio, rectangular, perimeter reinforced membrane wing. The wing was constructed of two shaped steel frames, sandwiching a rubber latex membrane, held at a prescribed in-plane pre-tension. The wing had a span of $280mm$ and chord of $140mm$, with a frame width and thickness of $5mm$ and $1mm$ respectively. The leading edge of each frame member has a radius of $0.9mm$ and a taper on the trailing edges. A schematic of the wing geometry is illustrated

in Fig. 4.7, and images of the actual test article can be seen in Fig. 4.8.

4.5.2 Test Conditions

To use test data for comparison and validation of the purposed model, it was important to envelope the range of each parameter to capture the sensitivity of the variable. A target range for flow conditions were a Reynolds number between 50k-100k, which are applicable values for applications to small-scale, low velocity aircraft. Target reduced frequency values of, $k = \{0, 0.05, 0.1\}$, were used while operating withing the pitching motor's operational envelope, shown in Fig. 4.9.

Given the compliant nature of the membrane wings used, it was desired that values of camber at different test conditions were comparable. Three target cambers were selected using the Waldman's membrane displacement approach [6], resulting in three membrane wings with corresponding stretch ratio, $\lambda = \{1.02, 1.058, 1.085\}$. In addition to these stretch ratios, a stretch ratio of $\lambda = \infty$ was also tested in order to see the influence of the frame on the aerodynamics of the wing, compared to the frame plus a compliant airfoil. Considering the test constraints and variable target ranges, the result of the experimental design can be seen in Fig. 4.10. Each line represents a membrane wing model with different pre-tension, each point represents a test condition (with a label corresponding to each unique test condition), and the points circled with a dotted line representing conditions of unstable membrane displacement at zero AOA.

In addition to testing the four membrane configurations, ($\lambda = \{1.02, 1.058, 1.085, \infty\}$), a 2:1 flat plate was also tested to serve as a basis of comparison to a well known aerodynamic profile. The geometry of this 2:1 flat plate wing conformed to the leading edge, trailing edge and thickness dimensions defined by Mueller [124]. This, so called "Mueller" flat plate, was tested for static AOA conditions and all dynamic AOA conditions.
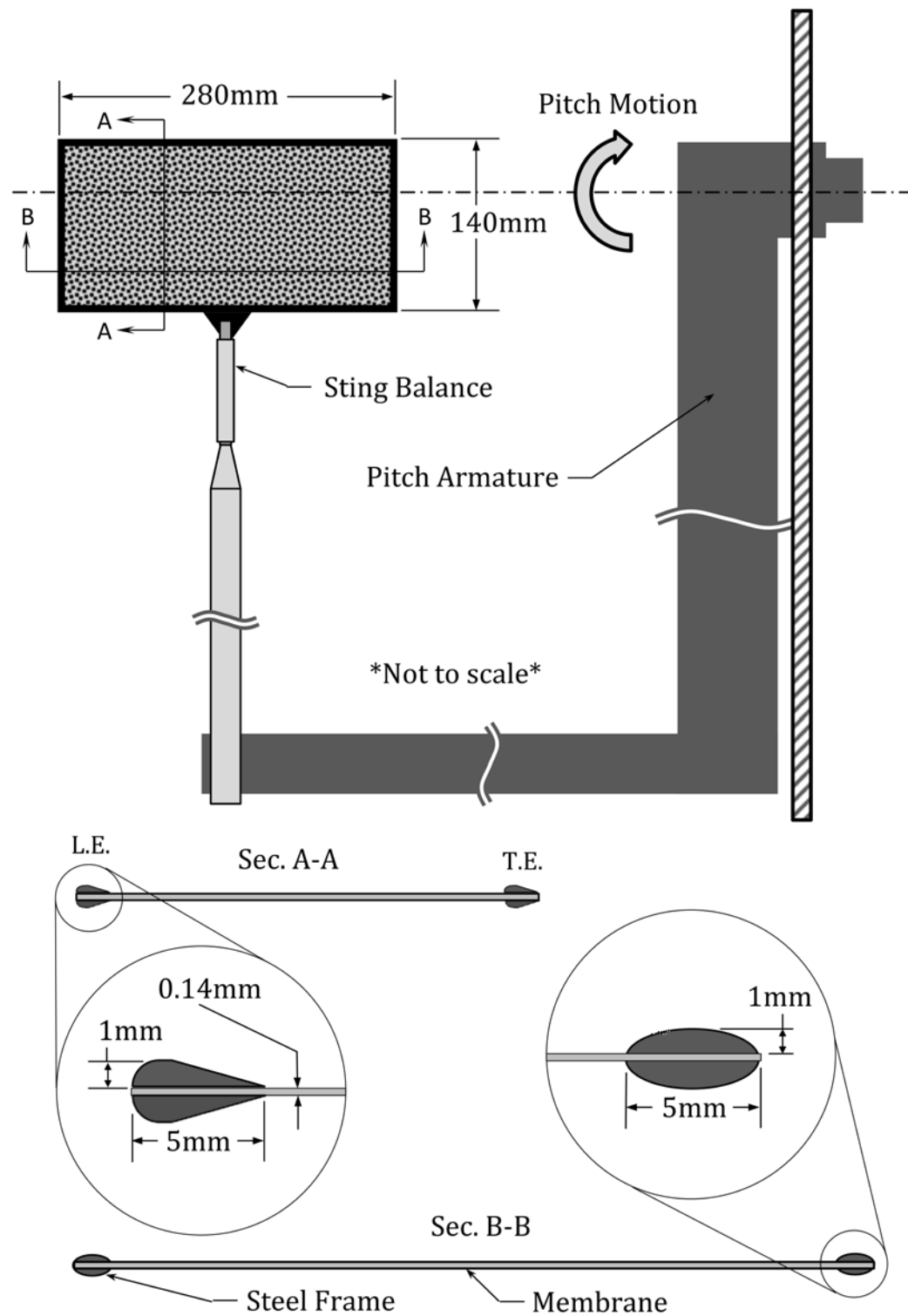
FIGURE 4.7: Wind tunnel pitching fixture and membrane wing with frame geometry. The pitching armature extends through the wind tunnel wall and connects to a servo motor mounted outside the wind tunnel. The motor rotation axis is represented as a dotted center-line which passes through the plane of the wing.

(a) Top View (b) Bottom View
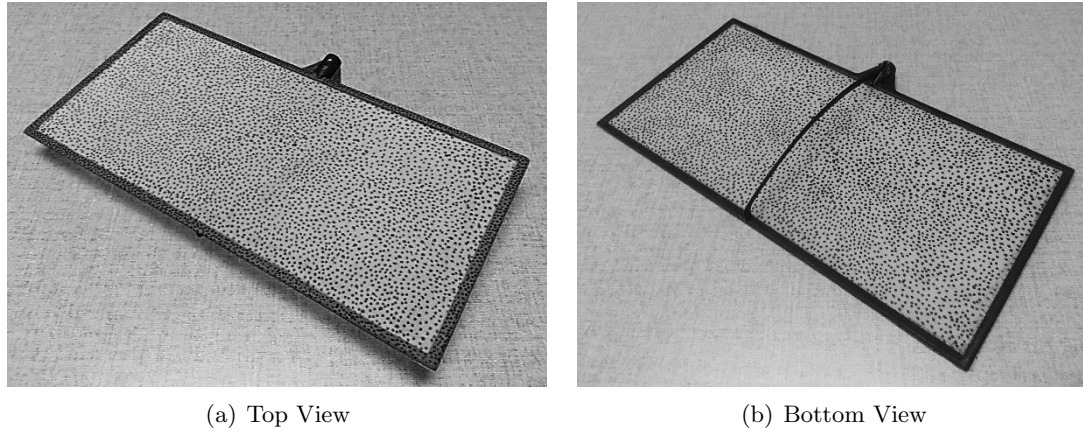
FIGURE 4.8: 2:1 membrane wing, with steel perimeter and speckled rubber latex membrane, used in wind tunnel experiments.
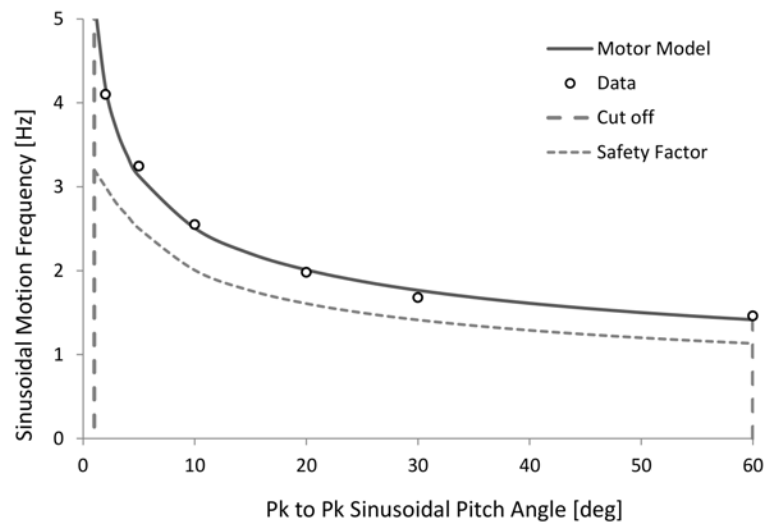
FIGURE 4.9: Empirical model of wind tunnel armature's max pitching frequency.
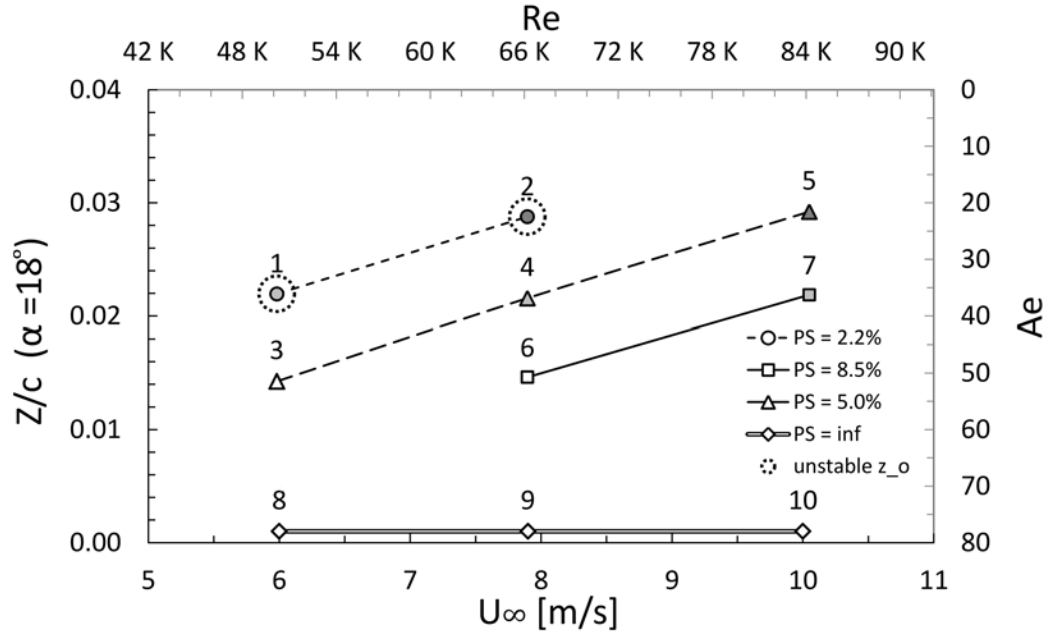
FIGURE 4.10: Predictions of membrane camber for different test conditions of flow velocity and membrane pretension. All points represent the different combinations of membrane pre-tension and flow conditions tested. Conditions with unstable membrane displacement at zero AOA are circled. Each condition is given a test configuration number, as seen by the label above each point.

For each condition in Fig. 4.10, data was collected at static AOA, for $\alpha = -2°$ to $30°$, at $2°$ increments. Load data was recorded for each angle at $1000\ hz$ for 1 second. Digital image correlation (DIC) images[5] were taken of each angle at $500\ hz$ for 0.2 seconds. For all wing configurations, dynamic sweeps were conducted using $\alpha_{st} = \{0°, 5°, 10°\}$, $\alpha_{amp} = 10°$, and $k = 0.1$. To reduce the size of the test matrix, dynamic sweeps of $k = 0.05$ were conducted for only test condition 1, 4, 7-10, and the "Mueller" flat plate.

---

[5]The total number of images was limited by internal camera memory, see hardware specifications.

TABLE 4.1: Dynamic Pitching Motions

Motion	k	α_st	α_amp	RE	f [hz]
1	0.05	0.0	10.0	50000	0.68
2	0.05	0.0	10.0	66000	0.9
3	0.05	0.0	10.0	84000	1.14
4	0.05	5.0	10.0	50000	0.68
5	0.05	5.0	10.0	66000	0.9
6	0.05	5.0	10.0	84000	1.14
7	0.05	10.0	10.0	50000	0.68
8	0.05	10.0	10.0	66000	0.9
9	0.05	10.0	10.0	84000	1.14
10	0.1	0.0	10.0	50000	1.36
11	0.1	0.0	10.0	66000	1.8
12	0.1	0.0	10.0	84000	2.28
13	0.1	5.0	10.0	50000	1.36
14	0.1	5.0	10.0	66000	1.8
15	0.1	5.0	10.0	84000	2.28
16	0.1	10.0	10.0	50000	1.36
17	0.1	10.0	10.0	66000	1.8
18	0.1	10.0	10.0	84000	2.28

4.5.3 Membrane Pre-Tension

A technique for prescribing uniform pretension to the latex membrane wing was developed using a two dimensional stretching jig. First, an over sized sheet of latex was fixed to two rigid plates along the edges of the membrane; typically the short edges if the aspect ratio is not 1:1. Then, the edge plates of the jig were displaced a predetermined amount to generate the desired amount of tension. Each plate had a degree of freedom to allow edge plates to freely rotate in the membrane plane. This rotation, allowed for a more evenly distributed tension along the length of the edge plates. When the desired displacement was reached, the strain produced in the membrane was measured using DIC, and averaged over the area of interest (AOI). When the desired strain was achieved, the last two edges of the membrane were fixed to the jig and displaced orthogonal relative to the first direction. DIC was used to measure the strain field and report an average strain value and standard deviation. Once the desired strain field was achieved, the metal wing frame was applied with a rubber adhesive and fixed to the membrane while the membrane remained fixed in the pretension jig. While the method produced reasonably "constant" strain feilds, it did not correct for variations due to the Poisson effect [125].

For all test specimens, the standard deviation of the strain field was kept less than $\pm10\%$ of the average measured strain.

4.5.4   Digital Image Correlation

Full-field measurements of strain and deformation were performed using digital image correlation [92, 93]. Images were captured with two high-speed AOS S-PRI cameras, capable of 1,000 frames per second (fps) and capable of saving 1,000 frames at a resolution of 1100x1710 pixels in an in-camera flash-memory buffer. The cameras were positioned above the membrane, approximately perpendicular to the membrane surface, with a stereoscopic angle of approximately $40°$ between cameras. For the wind tunnel experiment, the cameras were mounted outside and above the wind tunnel and viewed through a clear window. Cameras were calibrated while viewing through the windows, correcting for distortion effects from the windows. The DIC reference images were of the membrane subject to no load (zero wind velocity). Since this condition was used to take the reference images, the pretension did not appear directly in the DIC results. However, pretension was measured for each test specimen using the DIC system prior to being fixed to the metal wing frame.

DIC is often a black art when it comes to identifying parameters like camera settings, lighting, pattern applied to the specimen, and the parameters defined in the correlation software. Since the accuracy of the data returned from DIC becomes a function of these variables, it is necessary to develop a method for defining them. First the user must estimate the desired density of data points to be generated by the correlation method. This will provide a baseline target for setting up the camera system. For example, if the user desires 100 by 50 data points in a 2:1 aspect ratio area of interest, and the resolution of the image is 1000 by 500 pixels, if a 50% step-over was used, then the correlation subset window would need to be set to 20 by 20 pixels. With this subset window size, the size and density of the pattern can be defined in pixels. As a rule of thumb, any given subset
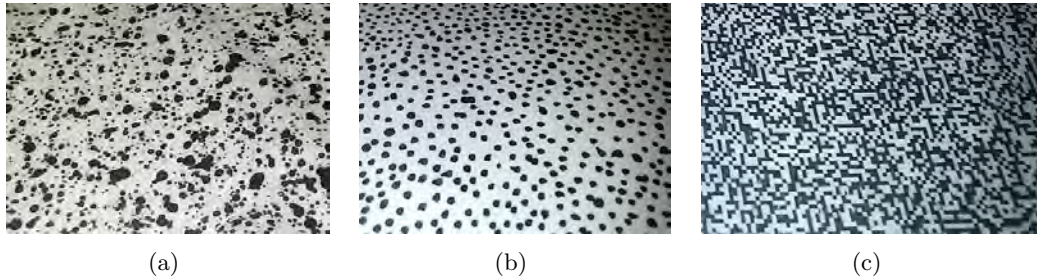
<div align="center">(a)   (b)   (c)</div>

FIGURE 4.11: DIC patterns generated via varying techniques; (a) Spray paint "speckeling", (b) felt tip marker dots, (c) printed digital pattern.

of the image should contain 3 to 10 identifiable "objects", and each object should have a minimum width of 3-5 pixels [126]. Once the cameras are focused on the specimen, and the AOI fills as much of the image as is practical for the given test, a ruler can be placed on the specimen to approximately measure the average near-field and far-field pixel length. With a known length per pixel, and the above criteria, the user can set about generating a random pattern with the appropriate object size and density.

In order to generating a repeatable DIC pattern with a specific object size and density on thin latex, several approaches were tried; spray paint speckling, by-hand marker dots, and printing a random computer generated pattern. Samples of all three methods are shown in Fig. 4.11. In general, the spray paint method proved to be the most difficult to control and produce repeatable results. Due to its inconsistency, this method also produced varying quality results. The "marker" method produced high quality results if the size of the marker aligned with the desired object size. While object density was easily controllable, object size was not, due to the fact that only a few size of dots could be produced based on the size of marker used. This method is also highly time consuming to produce a single specimen and becomes more impractical when many specimens are desired. The laser printer method offered the best results in terms of tunability of the pattern size and density, ease of production, and repeatably. The printing method used in this work was simple and effective. A low tack double sided masking tape was applied to a piece of paper, then a washed and dried piece of latex was placed onto the tape. This

could then be fed directly into a standard PC laser printer producing a specimen ready for testing.

4.5.5 Wind Tunnel Testing

The wind tunnel used to conduct the experiments was a low-speed, closed loop, closed test section, wind tunnel, capable of speeds from 1 to 18 meters per second (m/s) and with a 1.3 x 1.5 meter test section. As illustrated in Fig. 4.12, the test wing can be seen mounted to a sting balance, attached to a one degree of freedom pitching armature inside the test section. The motorized armature and motor control system was been developed to pitch a wing model about a desired axis, producing static or dynamic AOA.
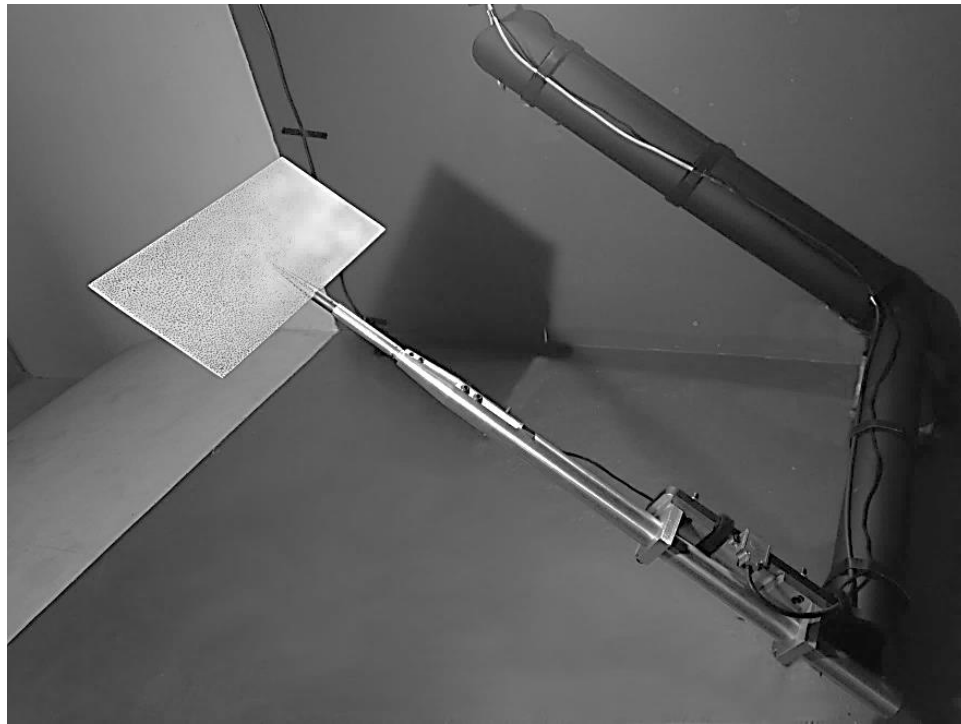

FIGURE 4.12: Wind tunnel pitching apparatus, showing a 2:1 flat plate wing with rear mounted sting balance.

The unique armature configuration connects trailing edge of wing allowing pitch motion to occur with minimal intrusion from the apparatus interfering with the three dimensional flow around the wing. Aerodynamic loads from the wing were measured

by a six degree-of-freedom sting balance fixed directly at the trailing edge. The system was capable of simultaneously pitching, measuring aerodynamic loads and performing non-intrusive strain and deflection measurements via DIC. Load and angle channels were recorded at 500Hz, and DIC images were taken at 500 frames per second.

The wing model angle was measured by a motor encoder and an inclinometer sensor with an accuracy of $\pm 0.05°$. The sting balance was capable of measuring loads up to 13 N normal force and 9 N axial force with a resolution of 0.01 N and 0.005 N respectively. The wind tunnel flow velocity was monitored by a pitot tube probe installed in the test section ahead of the model, connected to a pressure transducer with a resolution of 0.05 mmH_2O. Air temperature was monitored by a RTD sensor mounted inside the test section.

4.6.   Results

To evaluate the validity of the proposed approach of estimating dynamic lift due to pitching, experimental wind tunnel loads and membrane displacements are compared to the purposed model under varying conditions of flow velocity, pretension, pitching frequency, and AOA pitching ranges. Initially, the components composing the static lift curve, $C_{L,p}$, $C_{L,v}$, $C_{L,mem}$, $C_{L,att}$, $C_{L,sep}$, and X_{st}, will be evaluated for their validity compared to time averaged, static test data. Second, dynamic lift predictions, $C_{L,qs}$, and $C_{L,d}$, will be compared to dynamic test data as a function of α and time for varying dynamic pitching conditions.

4.6.1   Static Model

The coefficient of lift with respect to AOA for a 2:1 "Mueller" rigid flat plate; which has an elliptical leading edge, sharp beveled trailing edge, and a thickness of 3.2 mm is considered. Due to a well shaped, round leading edge, and a reasonably finite thickness, we would expect minimal leading edge separation. Thus for this wing, it is assumed

$C_{L,v}(\alpha) = 0$. The flat plate also has no elastic behavior to consider, thus we can drive $C_{L,mem} \to 0$ by setting λ_o to a relatively high value, such as $\lambda_o = 6$, i.e. a prestrain of 500%. With these two constraints, $C_{L,p} = C_{L,att}$, meaning the calculation of potential flow should adequately model the flat plate for pre-stall AOA. Finally, a commonly accepted Ozwald efficiency factor for rectangular wings of $\varepsilon = 0.9$ [127] for all wings within the study is applied.
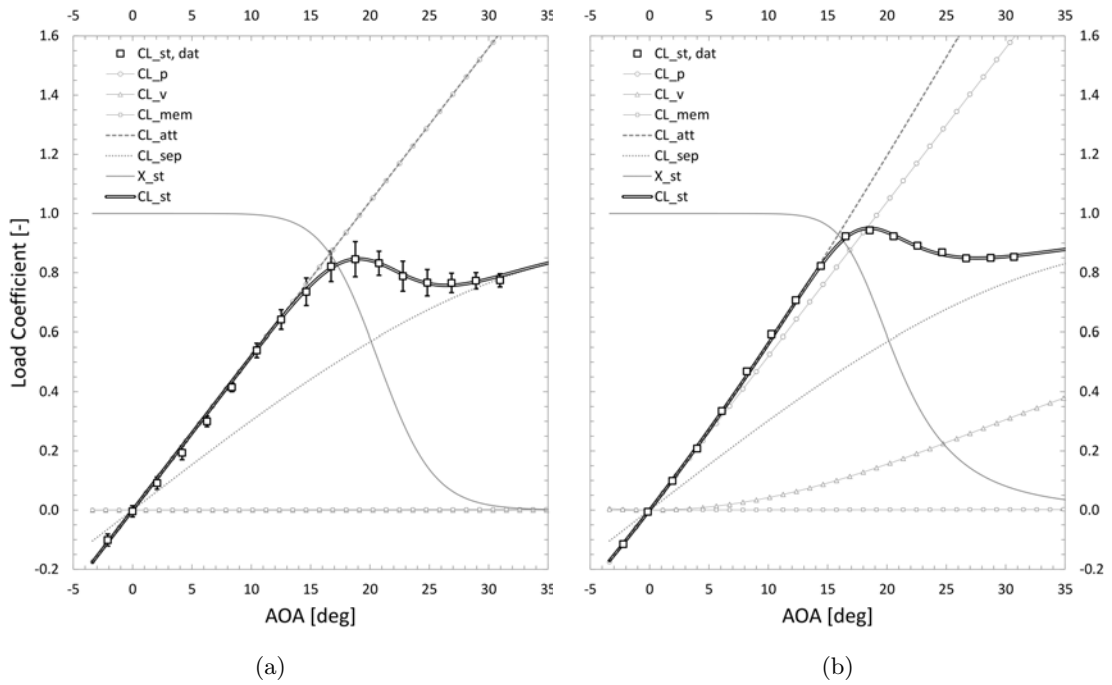
FIGURE 4.13: Static lift model and wind tunnel data, (a) 2:1 "Mueller" rigid flat plate, (b) membrane wing with "rigid" membrane.

Observing Fig. 4.13(a), it can be noticed that both $C_{L,v}$ and $C_{L,mem}$ have been driven to zero, and $C_{L,p} = C_{L,att}$. For $\alpha < 12°$, the potential flow component of lift accurately predicts measured lift. For high AOA, wind tunnel data approaches $C_{L,sep}$ in an asymptotic fashion as expected. Using data, $C_{L,att}$, and $C_{L,sep}$, a regression fit is used to generate X_{st}, from which $C_{L,st}$ can be calculated. It should be noted that this rigid wing, $C_{L,st}$ is invariant to changes in flow velocity within the ranges of this study ($Re = 50\text{k}-84\text{k}$).

Note, the error bars in Fig. 4.13(a) represent 95% confidence intervals which in most cases are smaller in magnitude than the square points representing the measurement in the figure. To reduce figure complexity, confidence intervals will not be presented on further graphs.

Next, consider the 2:1 perimeter reinforced membrane wing, where the membrane is replaced with a thin "rigid" plate of comparable thickness; creating an infinitely stiff membrane. For this wing, leading edge separation is expected due to its thin nature and leading edge geometry, thus $C_{L,v}(\alpha) \neq 0$. Referring to Fig. 4.13(b), $C_{L,mem}$ is still driven to zero, and $C_{L,att} > C_{L,p}$ due to the contribution of leading edge vortex, $C_{L,v}$. As previously noted, $C_{L,att}$ accurately models lift for low angles of attack, and the data appears to converge toward $C_{L,sep}$ for large AOA. Although, we notice the convergence of $C_{L,st}$ toward $C_{L,sep}$ is significantly slower for the perimeter reinforced wing than the flat plate.
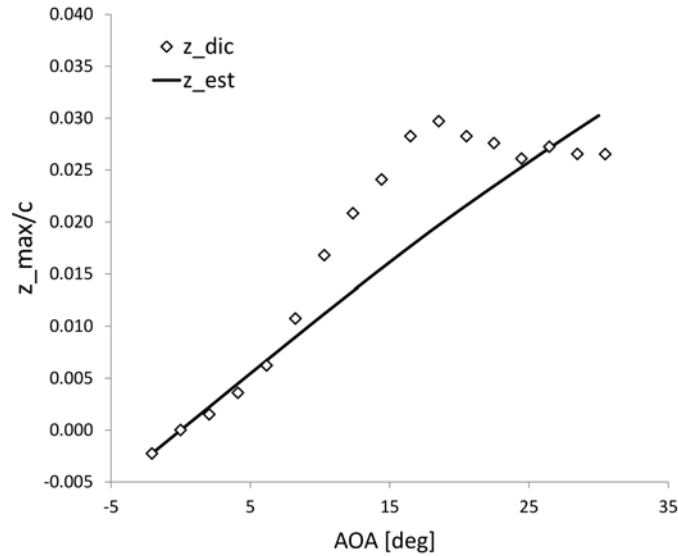

FIGURE 4.14: Measured maximum displacement from DIC data (diamonds), and predicted maximum displacement from Eqn. 4.6.

In general, results from Fig. 4.13 indicate the model has the capability to accurately predict lift over a large range of static AOA, for the 2:1 rigid flat plate and 2:1 membrane

wing with an infinitely rigid membrane, experiencing leading edge separation. Compliant membranes will be considered next.

Utilizing DIC data, the prediction of max camber, $z(\alpha)$, can be evaluated for its accuracy and overall physical behavior. Figure 4.14 represents the average maximum measured and predicted static camber, z_{dic} and z_{st} respectively, for a flow velocity of $U_\infty = 8 \ m/s$ ($Re = 66$k), and prestretch $\lambda_o = 1.058$ (or 5.8% average prestrain). The predicted maximum camber fairly accurately models measured displacements up to about $\alpha = 8°$. Beyond this AOA, z_{dic} increases at almost twice the rate until the onset of stall around 18°. After the onset of stall, z_{dic} slightly drops in magnitude from the peak displacement and remains approximately constant for increasing AOA. Equation 4.6 represents the physics of the system for small AOA, not surprising given the linearizing assumptions built into the prediction. Given the abrupt change in displacement at $\alpha = 8°$, it is assumed there is a secondary fluid-structure which this model does not capture. A possible source of further studies to extend this prediction to capture the high AOA membrane response. Given the results of the membrane camber predictions presented above, it is expected that the estimated coefficient of lift will be slightly under predicted for intermediate AOA, $\alpha = 8°$ to 18°.
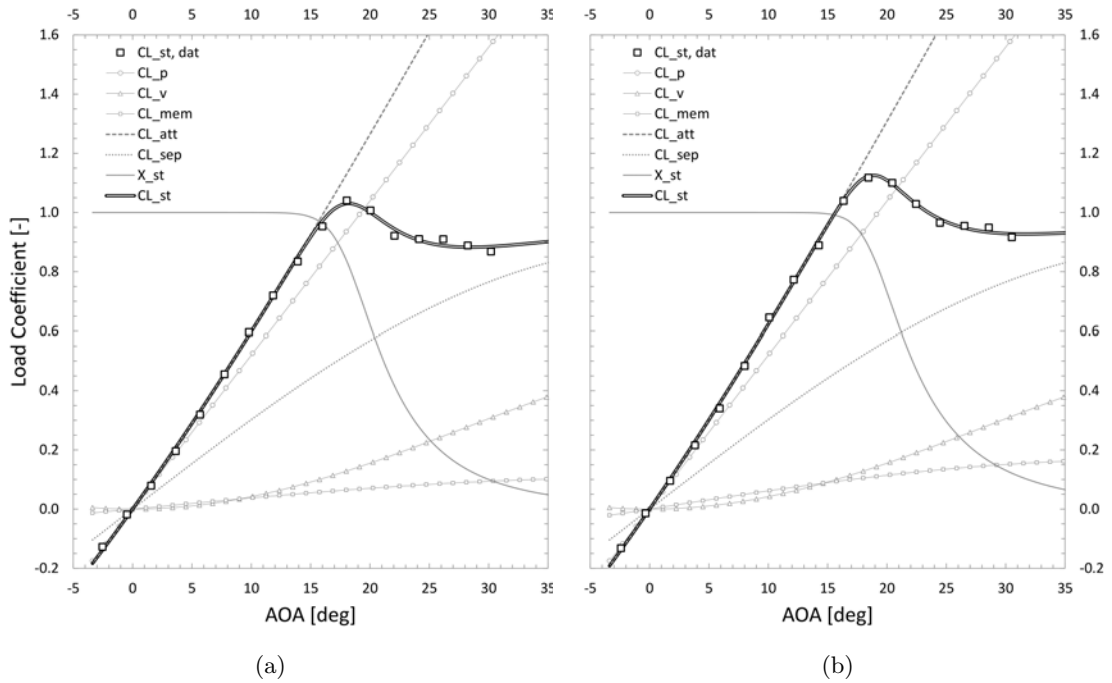
FIGURE 4.15: Static lift model (a) membrane at 5.8% prestrain and flow velocity of 6 m/s ($Re = 50k$), (b) membrane at 5.8% prestrain and flow velocity of 8 m/s ($Re = 66k$).

Figure 4.15(a) shows lift coefficient verus AOA for test condition "3", $\lambda_o = 1.058$, $U_\infty = 6\ m/s$ ($Re = 50k$), while for Fig. 4.15(b), depicts test condition "4", $\lambda_o = 1.058$, $U_\infty = 8\ m/s$ ($Re = 66k$). The lift contributions from leading edge separation, $C_{L,v}$ and membrane camber, $C_{L,mem}$, are non-zero for increasing AOA and cause the lift prediction to increase at a comparable rate to the wind tunnel data. While both cases are at the same pretension, due to the difference in dynamic pressure, more membrane camber and an increased lift slope and peak lift are expected for the higher flow velocity case. Indeed, due to the increased contribution of $C_{L,mem}$ for the higher velocity case, attached lift slope and peak lift are greater as illustrated in Fig. 4.15. Considering membrane stability at zero AOA, both conditions are assumed to be stable, i.e., zero camber and thus zero lift at zero AOA. Notice, measured and predicted lift are zero at zero AOA for both conditions.

Recalling from the test conditions depicted in Fig. 4.10, test condition "2", $\lambda_o = 1.02$ and $U_\infty = 8\ m/s$, was predicted to be unstable at $\alpha = 0°$. Observing the values of

lift at $\alpha = 0°$ from Fig. 4.16(b), indeed data shows a non-zero value of lift at zero AOA, indicating a true unstable membrane condition. The lift prediction accounts for the amount of non-zero lift, through predicting an AOA shift applied to $C_{L,p}$ from Eqn. 4.13. This correction appears to adequately account for the non zero lift at zero AOA.
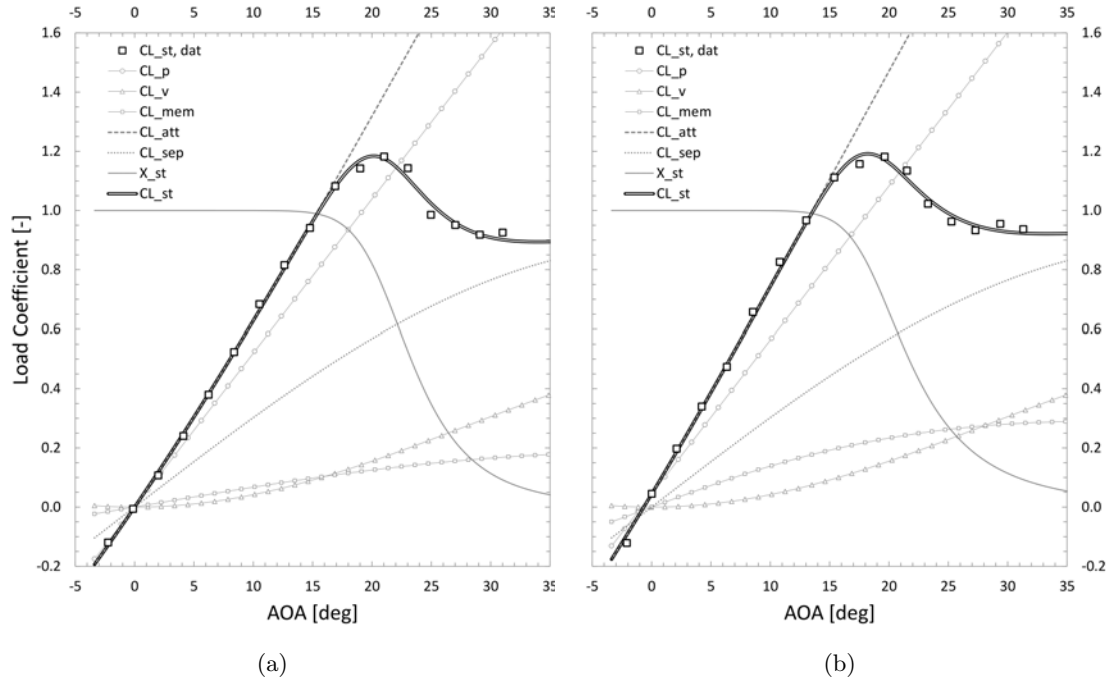
FIGURE 4.16: Static lift model, (a) membrane at 8.5% prestrain and flow velocity of 10 m/s ($Re = 84k$), (b) membrane 2.0% prestrain and flow velocity of 8 m/s ($Re = 66k$).

Comparing $C_{L,st}$ between Fig. 4.16(a) and Fig. 4.16(b), test conditions "7" and "1" respecively, two different flow conditions and prestrains are depicted, yet very similar lift characteristics are seen between the two static lift curves. These test conditions were targeted purposefully since they have the same predicted magnitude of camber. In all cases were we have the same estimated camber, {2, 5}, {1, 4, 7}, {3, 6}, the same trend is seen where the lift profiles are nearly identical. This states that camber is a driving factor in lift production for this type of wing.

Since the dynamic stall model applies modifications to the static lift model in order to account for pitch rates and time variant separation, it is important that the static

model accurately depicts the actual lift of the wing. As demonstrated in these results, the static lift model accurately predicts static attached flow conditions, and through the used of data to predict the trailing edge separation, the complete static lift model adequately represents the lift behavior for the rigid and membrane wings within the study.

4.6.2 Dynamic Stall Model

Having devised an adequate static lift model, dynamic conditions are now considered. Wings were tested under different flow velocities, $U_\infty = \{6, 8, 10m/s\}$ (Re 50k,66k,84k), two reduced frequencies, $k = \{0.05, 0.1\}$, and three AOA ranges, $\hat{\alpha} = \{0° \text{ to } 10°, 5° \text{ to } 10°, 10° \text{ to } 20°\}$. First, the empirical time constants τ_1 and τ_2^* must be determined.

FIGURE 4.17: Dynamic lift model for rigid membrane, pitching at $k = 0.05$ for $\alpha_s = 0°$ and $\alpha_{amp} = 10°$, flow velocity of 8 m/s ($Re = 66k$), (a) C_L vs α, showing both static and dynamic lift models with static and dynamic wind tunnel data, (b) C_L vs time, showing dynamic lift, quasi steady lift, static lift, and wind tunnel data.

For pitching maneuvers at low AOA, or where $X_st(\alpha) = 1$, the rate of trailing edge separation $\dot{X}_{st} = 0$, i.e. there is no separation at low AOA. Thus, results are time

invariant and are directly proportional to $\dot{\hat{\alpha}}$. For these low AOA maneuvers, $C_{L,d}$ is invariant to changes made to τ_1. Under these conditions τ_2^* can be tuned using dynamic wind tunnel data. Consider a single sinusoidal oscillation, where $\hat{\alpha} = \{0° \text{ to } 10°\}$, at a reduced frequency of $k = 0.05$. For this motion, the rigid membrane wing was subjected to a flow velocity of $U_\infty = 8 \ m/s$ (Re 66k), the results are presented in Fig. 4.17. Using this data, a value of $\tau_2^* = 4$ was found to produced accurate dynamic lift predictions, both as a function of α and time as seen in Fig. 4.17(a) and 4.17(b) repectively. All subsequent tests were modeled with the same value of τ_2^*.
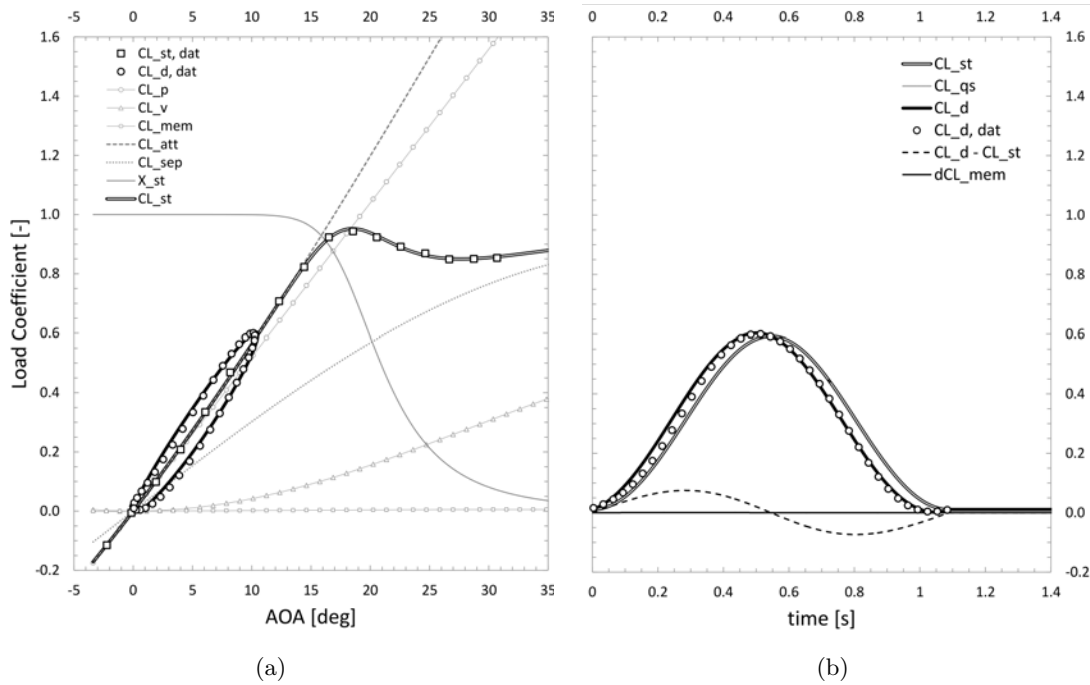

(a)   (b)

FIGURE 4.18: Dynamic lift model for rigid membrane, pitching at $k = 0.05$ for $\alpha_s = 10°$ and $\alpha_{amp} = 10°$, flow velocity of $8 \ m/s$ ($Re = 66k$), (a) C_L vs α, showing both static and dynamic lift models with static and dynamic wind tunnel data, (b) C_L vs time, showing dynamic lift, quasi steady lift, static lift, and wind tunnel data.

Next, τ_1 is tuned using data from a high AOA sweep. Fig. 4.18 shows the same wing, flow conditions and pitch rate, but for a motion where $\hat{\alpha} = \{10° \text{ to } 20°\}$. In this case, a value of $\tau_1 = 8.5$, produced accurate predictions with respect to AOA and time. This value of τ_1 was used for all further predicitons.

FIGURE 4.19: Dynamic lift model for a membrane at 8.5% prestrain, pitching at $k = 0.05$ for $\alpha_s = 10°$ and $\alpha_{amp} = 10°$, flow velocity of 10 m/s ($Re = 84k$), (a) C_L vs α, showing both static and dynamic lift models with static and dynamic wind tunnel data, (b) C_L vs time, showing dynamic lift, quasi steady lift, static lift, and wind tunnel data.
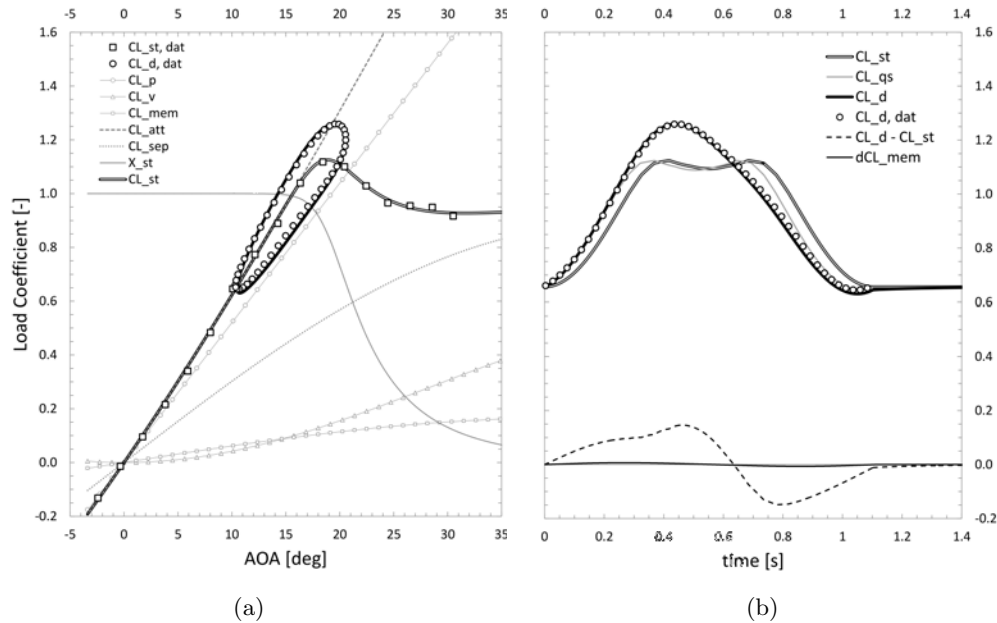
FIGURE 4.20: Dynamic lift model for a membrane at 5.8% prestrain, pitching at $k = 0.05$ for $\alpha_s = 10°$ and $\alpha_{amp} = 10°$, flow velocity of 8 m/s ($Re = 66k$), (a) C_L vs α, showing both static and dynamic lift models with static and dynamic wind tunnel data, (b) C_L vs time, showing dynamic lift, quasi steady lift, static lift, and wind tunnel data.
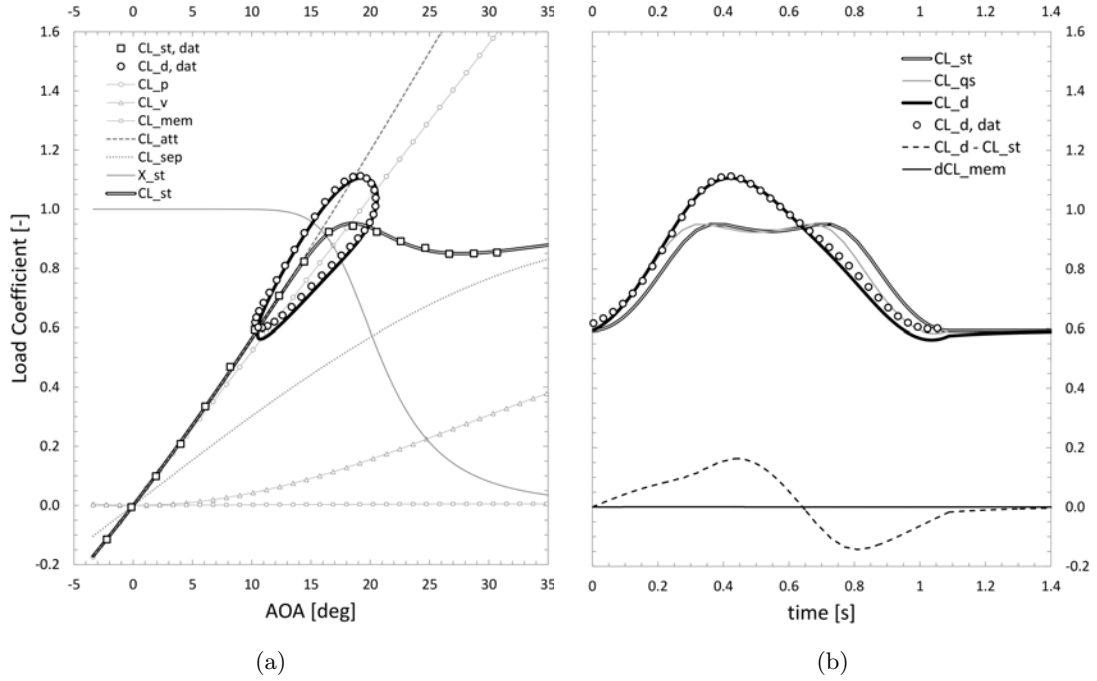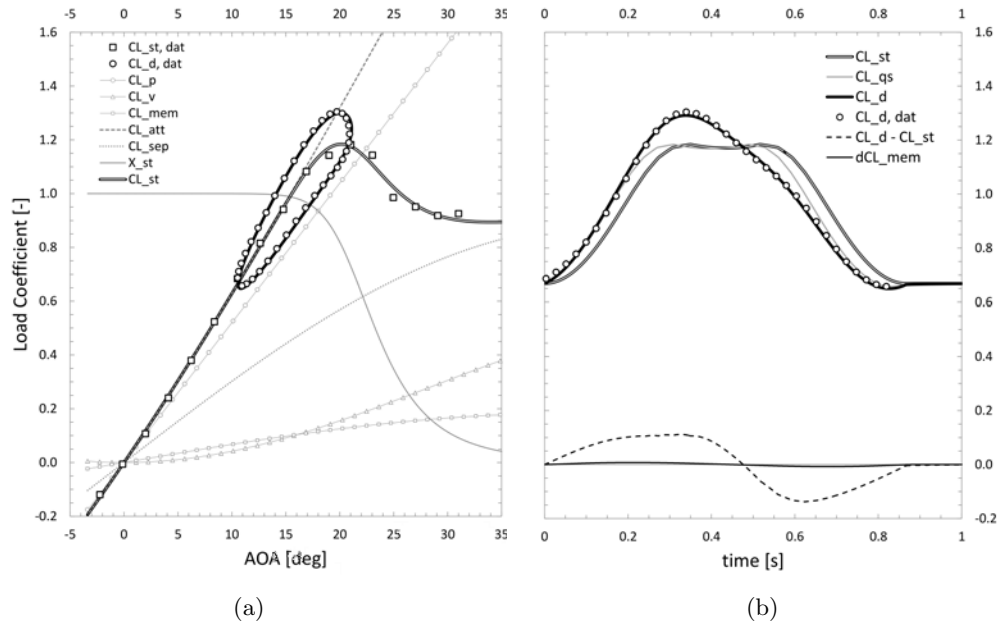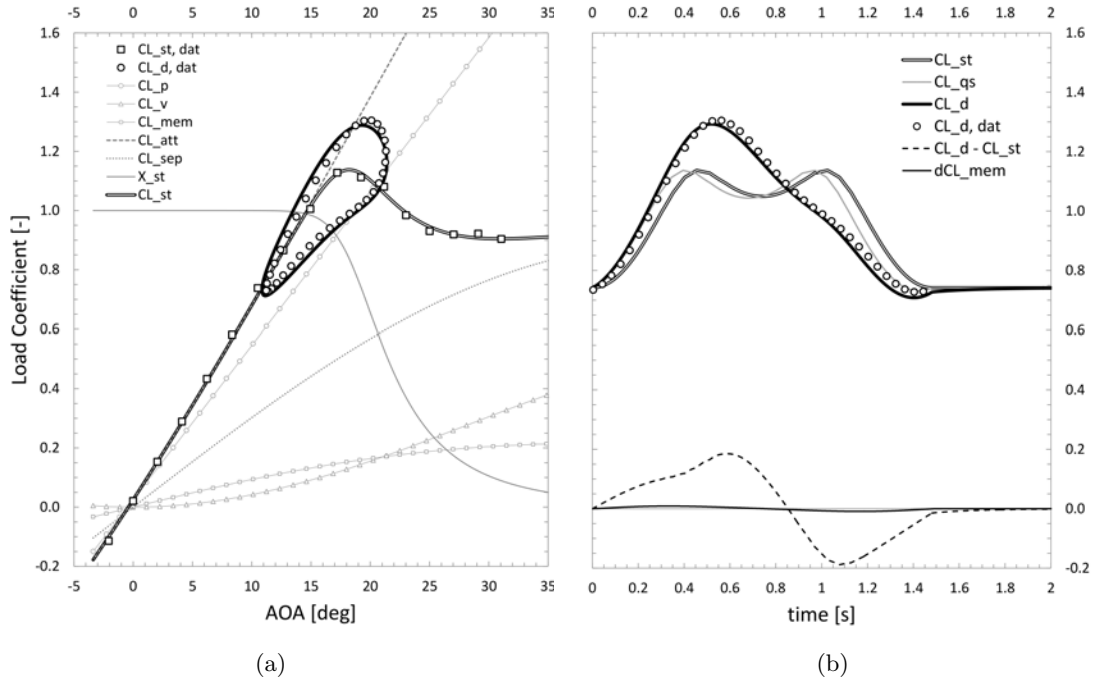
FIGURE 4.21: Dynamic lift model for a membrane at 2.0% prestrain, pitching at $k = 0.05$ for $\alpha_s = 10°$ and $\alpha_{amp} = 10°$, flow velocity of 6 m/s ($Re = 50k$), (a) C_L vs α, showing both static and dynamic lift models with static and dynamic wind tunnel data, (b) C_L vs time, showing dynamic lift, quasi steady lift, static lift, and wind tunnel data.

With the established values for τ_1 and τ_2^*, all membrane wings subjected to all testing conditions could be modeled and compared to measured values. Dynamic stall prediction for various membrane pretensions and flow velocities are reported in Fig.'s 4.19, 4.20, and 4.21. The results produced by this predictive model appear to be fairly robust to changes in flow velocity, pitching frequency, AOA ranges, and membrane tensions.

4.7.   Summary & Conclusion

A dynamic stall model is presented in this paper utilizing potential flow estimations of lift for static conditions to generate a static AOA lift model for attached and separated flow. Test data was used to predict the location of trailing edge separation for a given test scenario in order to produce an accurate static lift model for low to high AOA. This model

incorporates a prediction of lift due to static leading edge flow separation and membrane cambering. The stability criteria for membrane cambering at zero AOA was identified, and the magnitude of unstable cambering was predicted with acceptable accuracy for the conditions tested. With a complete static lift model, dynamic variations of lift were included due to instantaneous flow recirculation effects, added mass effects, and transient flow separation. A fist order, state space representation was used to model the time varying delayed separation effect experienced at high AOA. Using the purposed model, predictions of lift on thin flexible finite span wings, were compared to test data, both in static and dynamic pitching conditions. Wind tunnel tests were conducted for multiple 2:1 aspect ratio rectangular wings; both rigid and flexible. Over a wide variety of flow conditions, pitching rates, AOA ranges, and membrane pretensions, the model purposed produced acceptably accurate results.

Acknowledgments

5.   CONCLUSION

In this volume of work, three approaches to aerodynamic load estimation on a membrane wing were presented. Each utilized innovative methods in their application toward "feeling flight". The first, used strain sensors and a strain formulation for a perimeter reinforced membrane to predict the circulatory flow at the tip of the wing.

From the strength of this wing tip circulation, lift was estimated. This approach took a structural response, equated it to a wake flow response and then derived a guess of the load generating those responses. Given a fast enough iteration time, this approach has its application toward real-time flight load estimation. However, the practicality of implementing that with this approach seems unlikely due to the use of CFD for deriving the wake flow phenomena. Future endeavors could use a method of reduced order modeling, such as POD, to make a less computationally expensive estimation approach, and possible take the method toward real-time load identification.

The second approach to estimating loads on a membrane wing was an extension of the first. It utilized the same strain sensing, but approached the load formulation purely from a structural standpoint. This simplified the overall process by removing the extra step of estimating wake flow phenomena. The use of the Poisson formulation for a membrane subject to a normally distributed load, allowed for more fidelity of the load distribution over the wing. In addition to estimating the total lift, this approach also allowed for the estimation of moments since a center of pressure could be identified. This approach would lend itself well toward real-time estimation; given that the system was excited withing the bounds used to develop the POD basis. The possible additions of dynamic responses, such as harmonic vibration, could improve future accuracy of the method without exponentially increasing the number of strain sensors needed. Ultimately this approach proved to be an innovative and viable step toward real-time estimation of flight loads generated on a membrane wings.

The final work focused on estimating loads in a dynamic flight regime which would be directly applicable to small scale aerial vehicles. This regime was that of a time varying AOA maneuver, at low or high angles of attack, and at low Reynolds number. This approach accounted for leading edge flow separation, membrane displacement, flow separation due to stall, and time delayed flow separation effects. This approach was robust enough to predict these effects for any (reasonable) time varying pitching motion. In future

work, this approach could be integrated with the first or second methods presented, in order to improve the fidelity of the membrane displacement estimate. The dynamic stall formulation could be extended to predict other aerodynamic parameters such as pitching moment, which could again be integrated with the second approach in order to improve the accuracy of the load estimate. As it was presented, this approach correlated to data favorably and would be well suited for real-time load estimation, given known airspeed and AOA.

The concept of "feeling flight" is a simple one, yet the practical implementation and analytic formulation of this is not quite as straight forward. All told, this body of work has covered an array of load estimation approaches intended to further the understanding of the aerodynamics of membrane wings. It is the author's hope that this work will open new avenues of research and extend the knowledge and use of membrane wings in practical flight applications.

BIBLIOGRAPHY

1. Shyy, W., Berg, M., and Ljungqvist, D., "Flapping and flexible wings for biological and micro air vehicles," *Prog Aerosp Sci*, Vol. 35, 1999, pp. 455–505.

2. Song, A., Tian, X., Israeli, E., Galvao, R., Bishop, K., Swartz, S., and Breuer, K., "Aeromechanics of Membrane Wings with Implications for Animal Flight," *AIAA Journal*, Vol. 46, 2008, pp. 2096–2106.

3. Waldman, R., Song, A., Riskin, D., Swartz, S., and Breuer, K., "Aerodynamic Behavior of Compliant Membranes as Related to Bat Flight," *Fluid Dynamics and Co-located Conferences*, American Institute of Aeronautics and Astronautics, June 2008, pp. –.

4. Rojratsirikul, P., Wang, Z., and Gursul, I., "Unsteady Aerodynamics of Low Aspect Ratio Membrane Wings," *Aerospace Sciences Meetings*, American Institute of Aeronautics and Astronautics, Jan. 2010, pp. –.

5. Shyy, W., Aono, H., Chimakurthi, S., Trizila, P., Kang, C.-K., Cesnik, C., and Liu, H., "Recent progress in flapping wing aerodynamics and aeroelasticity," *Progress in Aerospace Sciences*, Vol. 46, No. 7, 2010, pp. 284 – 327.

6. Waldman, R. M. and Breuer, K. S., "Shape, lift, and vibrations of highly compliant membrane wings," *43rd Fluid Dyn. Conf.*, San Diego, CA, United states, 2013, pp. American Institute of Aeronautics and Astronautics (AIAA) –.

7. McMichael, J. and Francis, M., "Micro Air Vehicles - Toward a New Dimension in Flight," *Unmanned Systems*, Vol. 15, 1997, pp. 8–17.

8. Ray, C., *Modeling, Control, and Estimation of Flexible, Aerodynamic Structures*, Ph.D. thesis, Oregon State University, 2012.

9. Song, A. and Breuer, K., "Dynamics of a Compliant Membrane as Related to Mammalian Flight," *45th AIAA Aerospace Sciences Meeting and Exhibit*, Reno, NV, Jan. 8-11 2007.

10. Shyy, W., Lian, Y., Tang, J., Viieru, D., and Liu, H., *Aerodynamics of Low Reynolds Number Flyers*, Cambridge University Press, 2007.

11. Davis, W., Kosicki, B., Boroson, D., and Kostishack, D., "Micro Air Vehicles for Optical Surveillance," *The Lincoln Laboratory Journal*, Vol. 9, 1996, pp. 197–214.

12. Lillberg, E., Kamakoti, R., and Shyy, W., "Computation of unsteady interaction between viscous flows and flexible structure with finite inertia," *38th Aerospace Sciences Meeting and Exhibit*, 2000.

13. Katam, V., LeBeau, R., and Jacob, J., "Simulation of Separation Control on a Morphing Wing with Conformal Camber," *35th Fluid Dynamics Conference*, 2005.

14. Mueller, T., *Fixed and flapping wing aerodynamics for micro air vehicle applications*, American Institute of Aeronautics and Astronautics Prog Astronaut Aeronaut, 2001.

15. Wood, R. and Fearing, R., "Flight Force Measurements for a Micromechanical Flying Insect," *Proceedings of the 2001 IEEE/RSI International Conference on Intelligent Robots and systems*, 2001.

16. Raney, D. and Slominski, E., "Mechanization and control concepts for biologically inspried micro aerial vehicles," *Journal of Aircraft*, Vol. 41, 2004, pp. 1257–1265.

17. Khan, Z. and Agrawal, S., "Force and Moment Characterization of Flapping Wings for Micro Air Vehicle Application," *Proceedings of the 2005 American Control Conference, ACC*, 2005.

18. Shyy, W., Ifju, P., and Viieru, D., "Membrane wing-based micro air vehicles," *Appl Mech Rev*, Vol. 58, 2005, pp. 283–301.

19. Kim, D. and Han, J., "Smart flapping wing using Macro-Fiber Composite Actuators," *SPIE 13th Annual Symposium Smart Structures and Materials*, Vol. 6173, 2006, pp. 1–9.

20. Bradshaw, N. and Lentink, D., "Aerodynamic and structural dynamic identification of a flapping wing micro air vehicle," *26th AIAA Applied Aerodynamics Conference*, 2008.

21. Stanford, B., Ifju, P., Albertani, R., and Shyy, W., "Fixed membrane wings for micro air vehicles: Experimental characterization, numerical modeling, and tailoring," *Prog Aerosp Sci*, Vol. 44, 2008, pp. 258–294.

22. Kroninger, C., Pulskamp, J., Bronson, J., Polcawich, R., and Wetzel, E., "Bio-Mimetic Millimeter-Scale Flapping Wing for Micro Air Vehicles," Tech. rep., Army Research Laboratory, 2009.

23. Pai, P. and Chernova, D., "Nonlinear Modeling and Vibration Characterization of MAV Flapping Wing," *50th AIAA/ASME/ASCE/AHS/ASC Structures, Structural Dynamics, and Materials Conference*, 2009.

24. Croon, G., Clercq, K., Ruijsink, R., Remes, B., and Wagter, C., "Design, aerodynamics, and visionbased control of the DelFly," *International Journal of Micro Air Vehicles*, Vol. 1, 2009, pp. 71–97.

25. Clercq, K., Kat, R., Remes, B., Oudheusden, B., and Bijl, H., "Flow visualization and force measurements on a hovering flapping-wing MAV 'DelFly II'," *39th AIAA Fluid Dynamics Conference*, 2009.

26. Aono, H., Chimakurthi, S. K., Wu, P., Sallstrom, E., Stanford, B., Cesnik, C., Ifju, P., Ukeiley, L., and Shyy, W., "A Computational and Experimental Studies of Flexible Wing Aerodynamics," *Aerospace Sciences Meetings*, American Institute of Aeronautics and Astronautics, Jan. 2010, pp. –.

27. Finio, B., Prez-Arancibia, N., and Wood, R., "System identification and linear time-invariant modeling of an insect-sized flapping-wing micro air vehicle," *2011 IEEE/RSJ International Conference on Intelligent Robots and Systems*, 2011.

28. Norris, A., Palazotto, A., and Cobb, R., "Structural Dynamic Characterization of an Insect Wing," *Structures, Structural Dynamics, and Materials and Co-located Conferences*, American Institute of Aeronautics and Astronautics, April 2010, pp. –.

29. Anonymous, "The Surveillance Hummingbird," *Time*, Vol. November, November 2011, pp. 66.

30. Xie, L., Wu, P., and Ifju, P., "Advanced Flapping Wing Structure Fabrication for Biologically-Inspired Hovering Flight," *Structures, Structural Dynamics, and Materials and Co-located Conferences*, American Institute of Aeronautics and Astronautics, April 2010, pp. –.

31. Wang, J., "Dissecting Insect Flight," *Annual Review of Fluid Mechanics*, Vol. 37, 2005, pp. 183–210.

32. Jensen, M., "Biology and Physics of Locust Flight. III. The Aerodynamics of Locust Flight," *Philosophical transactions of the Royal Society of London. Biological sciences*, Vol. 239, 1956, pp. 511–552.

33. Willmott, A., Ellington, C., and Thomas, A., "Flow visualization and unsteady aerodynamics in the flight of the hawkmoth, Manduca sexta," *Philosophical transactions of the Royal Society of London. Biological sciences*, Vol. 352, 1997, pp. 303–316.

34. Ellington, C., "The aerodynamics of hovering insect fight. I The quasi-steady analysis," *Philosophical transactions of the Royal Society of London. Biological sciences*, Vol. 305, 1984, pp. 1–15.

35. Ellington, C., "The aerodynamics of hovering insect fight. II Morphological Parameters," *Philosophical transactions of the Royal Society of London. Biological sciences*, Vol. 305, 1984, pp. 17–40.

36. Ellington, C., "The aerodynamics of hovering insect fight. III Kinematics," *Philosophical transactions of the Royal Society of London. Biological sciences*, Vol. 305, 1984, pp. 41–78.

37. Ellington, C., "The aerodynamics of hovering insect fight. IV Aerodynamic mechanisms," *Philosophical transactions of the Royal Society of London. Biological sciences*, Vol. 305, 1984, pp. 79–113.

38. Ellington, C., "The aerodynamics of hovering insect fight. V Vortex Theory," *Philosophical transactions of the Royal Society of London. Biological sciences*, Vol. 305, 1984, pp. 115–144.

39. Ellington, C., "The aerodynamics of hovering insect fight. VI Lift and power requirements," *Philosophical transactions of the Royal Society of London. Biological sciences*, Vol. 305, 1984, pp. 1–15.

40. Willmott, A. and Ellington, C., "The mechanics of flight in the hawkmoth Manduca sexta," *Journal of Experimental Biology*, Vol. 200, 1997, pp. 2705–2722.

41. Wilkin, P., "The instantaneous force on a desert locust, Schistocerca gregaria (Orthoptera: Acrididae), Flying in a Wind Tunnel," *Journal of the Kansas Entomological Society*, Vol. 63, 1990, pp. 316–328.

42. Wilkin, P. and Williams, M., "Comparison of the aerodynamic forces on a flying Sphigid Moth with those predicted by quasi-steady theory," *Physiological Zoology*, Vol. 66, 1993, pp. 1015–1044.

43. Sedov, L., *Two-dimensional problems in hydrodynamics and aerodynamcis*, John Wiley & Sons, Inc., 1965.

44. Sunada, S. and Ellington, C., "Approximate added-mass method for estimating induced power for flapping flight," *AIAA Journal*, Vol. 38, 2000, pp. 1313–1321.

45. Khan, Z. and Agrawal, S., "Design of flapping mechanisms based on transverse bending phenomena in insects," *Proceedings - IEEE International Conference on Robotics and Automation*, 2006.

46. Khan, Z. and Agrawal, S., "Design and optimization of a biologically inspired flapping mechanism for flapping wing micro air vehicles," *Proceedings - IEEE International Conference on Robotics and Automation*, 2007.

47. Tobalske, B., Warrick, D., Clark, C., Powers, D., Hedrick, T., Hyder, G., and Biewener, A., "Three-dimensional kinematics of hummingbird flight," *Journal of Experimental Biology*, Vol. 210, 2007, pp. 2368–2382.

48. Ho, S., Nassef, H., Pornsinsirirak, N., Tai, Y., and Ho, C., "Unsteady aerodynamics and flow control for flapping wing flyers," *Progress in Aerospace Sciences*, Vol. 39, 2003, pp. 635–681.

49. Ferguson, L., Seshaiyer, P., Gordnier, R., and Attar, P., "Computational modeling of coupled membrane-beam flexible wings for micro air vehicles," *Collection of Technical Papers - AIAA/ASME/ASCE/AHS/ASC Structures, Structural Dynamics and Materials Conference*, 2007.

50. Willis, D., Israeli, E., Persson, P., Drela, M., Peraire, J., Swartz, S., and Breuer, K., "A computational framework for fluid structure interaction in biologically inspired flapping flight," *Collection of Technical Papers - AIAA Applied Aerodynamics Conference*, 2007.

51. Gordnier, R., "High fidelity computational simulation of a membrane wing airfoil," *Journal of Fluids and Structures*, Vol. 25, No. 5, 2009, pp. 897 – 917.

52. Gordnier, R. E. and Attar, P. J., "Impact of flexibility on the aerodynamics of an aspect ratio two membrane wing," *Journal of Fluids and Structures*, Vol. 45, No. 0, 2014, pp. 138 – 152.

53. Warrick, D., Tobalske, B., and Powers, D., "Aerodynamics of the hovering hummingbird," *Nature*, Vol. 435, 2005, pp. 1094–1097.

54. Poelma, C., Dickson, W., and Dickinson, M., "Time-resolved reconstruction of the full velocity field around a dynamically-scaled flapping wing," *Experiments in Fluids*, Vol. 41, 2006, pp. 213–225.

55. Suryadi, A. and Obi, S., "The estimation of pressure on the surface of a flapping rigid plate by stereo PIV," *Journal of Experimental Fluids*, Vol. 51, 2011, pp. 1403–1416.

56. Deluca, A. M., Reeder, M. F., and Cobb, R. G., "An experimental investigation into the effect of flap angles for a piezo-driven wing," *International Journal of Micro Air Vehicles*, Vol. 5, No. 1, 2013, pp. 55 – 92, Air force institute of technologies;Experimental investigations;Flapping frequency;Moment measurements;Particle image velocimetries;Six degree-of-freedom;Structural resonance;Voltage amplitude;.

57. Attar, P. J. and Gordnier, R. E., "High fidelity computational aeroelastic analysis of a plunging membrane airfoil," *50th AIAA Structures, Structrual Dynamics, and Materials Conference*, Palm Springs, CA, United states, 2009.

58. Wu, P., *Experimental characterizationm, design, analysis and optimization of flexible flapping wings for micro air vehicles*, Ph.D. thesis, University of Florida, 2010.

59. Coates, C. and Thamjuraj, P., "Inverse method using finite strain measurements to determine flight load distribution functions," *Journal of Aircraft*, Vol. 45, 2008, pp. 366–370.

60. Kang, D. and Lansey, K., "The battle of the water calibration networks (BWC): Roughness and demand estimation based on weighted least squares (WLS) method," *Water Distribution Systems Analysis 2010 - Proceedings of the 12th International Conference, WDSA 2010*, 2010.

61. Kang, D. and Lansey, K., "Real-Time Demand Estimation and Confidence Limit Analysis for Water Distribution Systems," *Journal of Hydraulic Engineering*, Vol. 135, 2009, pp. 825–837.

62. Liu, H., Ma, W., Wu, X., and Hu, H., "Real-time estimation of arterial travel time under congested conditions," *Transportmetrica*, Vol. 8, 2012, pp. 87–102.

63. Jabari, S. and Liu, H., "A stochastic model of traffic flow: Theoretical foundations," *Transportation Research Part B: Methodological*, Vol. 46, 2012, pp. 156–174.

64. Seppnen, A., Vauhkonen, M., Vauhkonen, P., Somersalo, E., and Kaipio, J., "Fluid dynamical models and state estimation in process tomography: Effect due to inaccuracies in flow fields," *Journal of Electronic Imaging*, Vol. 10, 2001, pp. 630–640.

65. Lipponen, A., Seppnen, A., and Kaipio, J., "Nonstationary approximation error approach to imaging of three-dimensional pipe flow: Experimental evaluation," *Measurement Science and Technology*, Vol. 22, 2011.

66. Berg, J. and Miller, K., "Force estimation via Kalman filtering for wind turbine blade control," *Conference Proceedings of the Society for Experimental Mechanics Series*, 2010.

67. Andino, M., Wallace, R., and Glauser, M., "Boundary feedback flow control: Proportional control with potential application to aero-optics," *AIAA Journal*, Vol. 49, 2011, pp. 32–40.

68. Na, S., Librescu, L., Marzocca, P., Kim, M., and Jeong, I., "Aeroelastic response of flapped-wing systems using robust estimation control methodology," *Journal of Guidance, Control, and Dynamics*, Vol. 29, 2006, pp. 199–203.

69. Allwine, D., Fisher, J., Strahler, J., Wu, M., Rose, I., Guan, J., and Lawrence, D., "On-line aerodynamic identification for space access vehicles," *Collect. Tech. Pap. AIAA Guidance Navig. Control Conf.*, 2006.

70. Naguib, A., Hudy, L., and Humphreys, W., "Stochastic estimation and non-linear wall-pressure sources in a separating/reattaching flow," *ASME Fluids Eng Div Publ FED*, 2002.

71. Durgesh, V. and Naughton, J., "Multi-time-delay LSE-POD complementary approach applied to unsteady high-Reynolds-number near wake flow," *Experiments in Fluids*, Vol. 49, 2010, pp. 571–583.

72. Hudy, L. and Naguib, A., "Stochastic estimation of a separated-flow field using wall-pressure-array measurements," *Physics of Fluids*, Vol. 19, No. 2, 2007, pp. 024103.

73. Nguyen, T., Wells, J., Mokhasi, P., and Remfer, D., "Proper orthogonal decomposition-based estimations of the flow field from particle image velocimetry wall-gradient measurements in the backward-facing step flow," *Measurement Science and Technology*, Vol. 21, 2010, pp. 1–15.

74. Taylor, J. and Glauser, M., "Towards practical flow sensing and control via POD and LSE based low-dimensional tools," *Journal of Fluids Engineering, Transactions of the ASME*, Vol. 126, 2004, pp. 337–345.

75. Payne, F. and Lumely, J., "Large eddy structure of the turbulent wake behind a circular cylinder," *Physics of Fluids*, Vol. 10, 1967, pp. 194–196.

76. Tadmor, G., Lehmann, O., Noack, B., Cordier, L., Delville, J., Bonnet, J., and Morzynski, M., "Reduced-order models for closed-loop wake control," *Phil. Trans. R. Soc. Lond. A*, Vol. 369, 2011, pp. 1513–1524.

77. Schmit, R. and Glauser, M., "Use of low-dimensional methods for wake flowfield estimation from dynamic strain," *AIAA Journal*, Vol. 43, 2005, pp. 1133–1136.

78. Martin, T., Hall, J., Schmit, R., and Glauser, M., "Estimation procedures for Micro air vehicles," *Collect. Tech. Pap. Aerosp. Sci. Meet.*, 2006.

79. Ausseur, J., Pinier, J., Glauser, M., Higuchi, H., and Carlson, H., "Experimental development of a reduced-order model for flow separation control," *Collect. Tech. Pap. Aerosp. Sci. Meet.*, 2006.

80. Pinier, J., Ausseur, J., Glauser, M., and Higuchi, H., "Proportional closed-loop feedback control of flow separation," *AIAA Journal*, Vol. 45, 2007, pp. 181–190.

81. Ausseur, J., Pinier, J., and Glauser, M., "Estimation techniques in a turbulent flow field," *Coll. Tech. Pap. AIAA Fluid Dynam. Conf.*, 2007.

82. Lumely, J., "The structure of inhomogeneous turbulent flows," *Journal of Atmospheric Turbulence and Radio Wave Propagation*, Vol. Nauka, Moscow & Toulouse, France, 1967, pp. 166–178.

83. Lumely, J., *Stochastic tools in turbulence*, Academic Press, 1970.

84. Siegel, S., Seidel, J., Fagley, C., Luchtenburg, D., Cohen, K., and MchLaughlin, T., "Low-dimensional modelling of a transient cylinder wake using double proper orthogonal decomposition," *Journal of Fluid Mechanics*, Vol. 610, 2008, pp. 1–42.

85. Cohen, K., Siegel, S., McLaughlin, T., Gilles, E., and Myatt, J., "Closed-loop approaches to control of a wake flow modeled by the GinzburgLandau equation," *Journal of Computers & Fluids*, Vol. 34, 2004, pp. 927–949.

86. Tropea, C., Yarin, A., and Foss, J., editors, *Springer Handbook of Experimental Fluid Mechanics*, Springer, 2007.

87. Rojratsirikul, P., Genc, M., Wang, Z., and Gursul, I., "Flow-induced vibrations of low aspect ratio rectangular membrane wings," *Journal of Fluids and Structures*, Vol. 27, No. 8, 2011, pp. 1296 – 1309.

88. Curet, O., Carrere, A., Waldman, R., and Breuer, K., "Aerodynamic Characterization of a Wing Membrane with Variable Compliance," *AIAA Journal*, Vol. 52, 2014, pp. 1749–1756.

89. Gursul, I., Cleaver, D., and Wang, Z., "Control of low Reynolds number flows by means of fluidstructure interactions," *Progress in Aerospace Sciences*, Vol. 64, No. 0, 2014, pp. 17 – 55.

90. Tregidgo, L., Wang, Z., and Gursul, I., "Low Aspect-Ratio Membrane Wing Undergoing Transient Pitching Motion at a Low Reynolds Number," *Fluid Dynamics and Co-located Conferences*, American Institute of Aeronautics and Astronautics, June 2011, pp. –.

91. Tregidgo, L., Wang, Z., and Gursul, I., "Unsteady fluidstructure interactions of a pitching membrane wing," *Aerospace Science and Technology*, Vol. 28, No. 1, 2013, pp. 79 – 90.

92. Sutton, M., Mingqi, C., Peters, W., Chao, Y., and McNeill, S., "Application of an optimized digital correlation method to planar deformation analysis," *Image and Vision Computing*, Vol. 4, No. 3, 1986, pp. 143 – 150.

93. Sutton, M., Turner, J., Bruck, H., and Chae, T., "Full-field representation of discretely sampled surface deformation for displacement and strain analysis," *Experimental Mechanics*, Vol. 31, 1991, pp. 168–177.

94. Schmit, R. and Glauser, M., "Improvements in Low Dimensional Tools for Flow-Structure Interaction Problems: Using Global POD," *Aerospace Sciences Meetings*, American Institute of Aeronautics and Astronautics, Jan. 2004, pp. –.

95. Stanford, B., Albertani, R., and Ifju, P., "Inverse Methods to Determine the Aerodynamic Forces on a Membrane Wing," *Structures, Structural Dynamics, and Materials and Co-located Conferences*, American Institute of Aeronautics and Astronautics, April 2007, pp. –.

96. Dickinson, B. T. and Singler, J. R., "Distributed Load Estimation From Noisy Structural Measurements," *Journal of Applied Mechanics*, Vol. 80, No. 4, May 2013, pp. 041011–041011.

97. Stanford, B., Albertani, R., Lacore, D., and Parker, G., "Proper Orthogonal Decomposition of Flexible Clap and Fling Elastic Motions via High-Speed Deformation Measurements," *Experimental Mechanics*, Vol. 53, No. 7, 2013, pp. 1127–1141.

98. Carpenter, T., Ray, C., and Albertani, R., "Correlation of Structural Strain to Tip Vorticity and Lift for a MAV Pliant Membrane Wing," *Experimental and Applied Mechanics, Volume 4*, Conference Proceedings of the Society for Experimental Mechanics Series, Springer New York, 2013, pp. 1–13.

99. Branch, M. A., Coleman, T. F., , Li, Y., and Li, Y., "A Subspace, Interior, and Conjugate Gradient Method for Large-Scale Bound-Constrained Minimization Problems," *Journal of Scientific Computation*, Vol. 21, 1999, pp. 1–23.

100. Byrd, R., Schnabel, R., and Shultz, G., "Approximate solution of the trust region problem by minimization over two-dimensional subspaces," *Mathematical Programming*, Vol. 40, No. 1-3, 1988, pp. 247–263.

101. Stanford, B. and Ifju, P., "The Validity Range of Low Fidelity Structural Membrane Models," *Experimental Mechanics*, Vol. 48, No. 6, 2008, pp. 697–711.

102. Cohen, K., Siegel, S., J., Aradag, S., and McLaughlin, T., "Nonlinear estimation of transient flow field low dimensional states using artificial neural nets," *Expert Systems with Applications*, Vol. 39, 2010, pp. 1264–1272.

103. LaCroix, B., Gardiner, C., and Ifju, P., "Investigating the Aerodynamic Effects of Flexible Membrane Wings," *Imaging Methods for Novel Materials and Challenging Applications, Volume 3*, Conference Proceedings of the Society for Experimental Mechanics Series, Springer New York, 2013, pp. 345–352.

104. Posada, J. A., *Numerical study of wingtip shed vorticity reduction by wing Boundary Layer Control*, Ph.D. thesis, West Virginia University, 2007.

105. Imamura, T., Enomoto, S., and Yamamoto, K., "Noise Simulation around NACA0012 Wingtip using Large Eddy Simulation," *Japan Society of Aeronautical Space Sciences Transactions*, Vol. 55, 2012, pp. 214–221.

106. Stanford, B., Viieru, D., Albertani, R., Shyy, W., and Ifju, P., "A Numerical and Experimental Investigation of Flexible Micro Air Vehicle Wing Deformation," *Aerospace Sciences Meetings*, American Institute of Aeronautics and Astronautics, Jan. 2006, pp. –.

107. McCroskey, W., Carr, L., and McAlister, K., "Dynamic Stall Experiments on Oscillating Airfoils," *AIAA Journal*, Vol. 14, No. 1, Jan. 1976, pp. 57–63.

108. McCroskey, W., "The phenomenon of dynamic stall," *Von Karman Inst. for Fluid Dynamics Unsteady Airloads and Aeroelastic Probl. in Separated and Transonic Flow*, 1981.

109. Carr, L. W., "Progress in analysis and prediction of dynamic stall," *Journal of Aircraft*, Vol. 25, No. 1, Jan. 1988, pp. 6–17.

110. Coton, F. and Galbraith, R., "Experimental study of dynamic stall on a finite wing," *Aeronautical Journal*, Vol. 103, No. 1023, 1999, pp. 229 – 236.

111. Cummings, R., Morton, S., and Siegel, S., "Numerical Predictions and Wind Tunnel Experiment for a Pitching Unmanned Combat Air Vehicle," *Aerospace Sciences Meetings*, American Institute of Aeronautics and Astronautics, Jan. 2003, pp. –.

112. Beddoes, T., "Onset of leading edge separation effects under dynamic conditions and low mach numbers," *34th Annual National Forum of the American Helicopter Society*, American Helicopter Society, 1978.

113. Leishman, G., "Dynamic stall experiments on the NACA 23012 aerofoil," *Experiments in Fluids*, Vol. 9, 1990, pp. 49–58.

114. Goman, M. and Khrabrov, A., "State-space representation of aerodynamic characteristics of an aircraft at high angles of attack," *Journal of Aircraft*, Vol. 31, No. 5, Sept. 1994, pp. 1109–1115.

115. Larsen, J., Nielsen, S., and Krenk, S., "Dynamic stall model for wind turbine airfoils," *Journal of Fluids and Structures*, Vol. 23, No. 7, 2007, pp. 959 – 982.

116. Polhamus, E. C., "A Concept of the Vortex Lift of Sharp-Edge Delta Wings Based on a Leading-Edge-Suction Analogy (NASA TN D-3767)," Tech. rep., Langely Research Center, NASA, 1966.

117. Polhamus, E. C., "Application of the Leading-Edge-Suction Analogy of Vortex Lift to the Drag Due to Lift of Sharp-Edge Delta WIngs (NASA TN D-4739)," Tech. rep., Langley Research Center, NASA, 1968.

118. Stanford, B., Ifju, P., Albertani, R., and Shyy, W., "Fixed membrane wings for micro air vehicles: Experimental characterization, numerical modeling, and tailoring," *Progress in Aerospace Sciences*, Vol. 44, No. 4, 2008, pp. 258 – 294.

119. Alioli, M., Masarati, P., Morandini, M., Carpenter, T., and Albertani, R., "Nonlinear Membrane Inverse Finite Element Model for Pliant Wings," *AIAA SciTech*, American Institute of Aeronautics and Astronautics, Jan. 2015, pp. –.

120. Reich, G. W., Eastep, F. E., Altman, A., and Albertani, R., "Transient Poststall Aerodynamic Modeling for Extreme Maneuvers in Micro Air Vehicles," *Journal of Aircraft*, Vol. 48, No. 2, March 2011, pp. 403–411.

121. Wickenheiser, A. M. and Garcia, E., "Optimization of Perching Maneuvers Through Vehicle Morphing," *Journal of Guidance, Control, and Dynamics*, Vol. 31, No. 4, July 2008, pp. 815 – 823.

122. Sheldahl, R. and Klimas, P., "Aerodynamic Characteristics of Seven Symmetrical Airfoil Sections Through 180-degree Angle of Attach for Use in Aerodynamic Analysis of Vertical Axis Wind Turbines," Tech. rep., Sandia National Laboratories, 1981.

123. Leishman, G., *Principles of Helicopter Aerodynamics*, Cambridge University Press, 2006.

124. Pelletier, A. and Mueller, T. J., "Low Reynolds Number Aerodynamics of Low-Aspect-Ratio, Thin/Flat/Cambered-Plate Wings," *Journal of Aircraft*, Vol. 37, No. 5, Sept. 2000, pp. 825–832.

125. Carpenter, T. and Albertani, R., "Aerodynamic Load Estimation from Virtual Strain Sensors for a Pliant Membrane Wing," *AIAA Journal*, Vol. 53, 2015, pp. ???

126. Sutton, M. A., Orteu, J.-J., and Schreier, H., *Image Correlation for Shape, Motion and Deformation Measurements: Basic Concepts,Theory and Applications*, Springer Publishing Company, Incorporated, 1st ed., 2009.

127. Oswald, W., "General Formulas and Charts for the Calculation of Airplane Performance (NACA-TR-408)," Tech. rep., U.S. Department of Commerce, National Technical Information Service, 1933.